UNIVERSITY OF COPENHAGEN
FACULTY OF SCIENCE

TU Graz

Thorsten Balduin, M.Sc.

Dust grain charging in protoplanetary disks and the potential emergence of lightning

DOCTORAL THESIS

to achieve the university degree of

Doktor der Naturwissenschaften at Graz University of Technology

and

Doctor of Philosophy at University of Copenhagen

submitted to

Graz University of Technology

and

PhD School of The Faculty of Science, University of Copenhagen

Supervisors

Univ.-Prof. Dr.rer.nat. Christiane Helling,
Institute of Theoretical and Computational Physics, Graz University of Technology
and
Prof. Uffe Gråe Jørgensen
Niels Bohr Institute, Faculty of Science, University of Copenhagen

Graz, April 2024

Acknowledgements

I would like to thank Doctor Peter Woitke from the IWF for his support and tremendously positive influence on this work.

I would also like to thank Dr. Dominic Bartholomew Singh Samra for helping me in writing this thesis and for being a good friend to me.

Thank you as well to Kristian Holten-Møller for his help on the KROME implementation.

I also thank all the ESRs from the CHAMELEON ITN for being a very supportive group of people, without whom this trip through the field of astrophysics would have be significantly less enjoyable. It was an honor to represent you people for a year.

This project is funded by the European Union's Horizon 2020 research and innovation programme under the Marie Sklodowska-Curie grant No 860470.



Affidavit

I declare that I have authored this thesis independently, that I have not used other than the declared sources/resources, and that I have explicitly indicated all material that has been quoted either literally or by content from the sources used. The text document uploaded to TUGRAZonline is identical to the present thesis.

18.04.2024
Date

Signature

Abstract

Wherever lightning occurs, it impacts the chemistry profoundly. Therefore, lightning could have a substantial impact on the chemistry of protoplanetary disks. The link between lightning and protoplanetary disks are charged dust grains, as they are required for lightning to emerge and do appear in the midplanes of protoplanetary disks. Charged dust grains can play a vital role in the planet formation process due to their interaction with the magneto rotational instability, hence understanding their charging behavior in detail could give new insights into the planet formation process.

The main topic of this work is to investigate how dust grains charge in the midplanes of proplanetary disks, how they impact the chemistry and the charge balance and lastly whether they could lead to the emergence of lightning. In order to study the charging behavior of dust grains in protoplanetary disks, I use the thermo-chemical disk model ProDiMo (Woitke et al. [2016]).

I did several improvements to the model, in order to make this study possible. For example I made it possible for the model to consider several different dust grain sizes, where previously the model used a single average dust grain size. Additionally I implemented a new approach in the charging chemistry of ProDiMo where we can now handle triboelectric charging in conjunction with the other charging mechanisms, such as photoionization, electron attachment and charge exchanges between dust grains and molecules. This approach of combining triboelectric charging and other charging mechanism is a completely new approach in the field.

The main findings of this study is that in the midplanes of protoplanetary disks the dust grains become the dominant negative charge carrier and together with NH_4^+ dominate the charge balance.

Using these results, I developed a simple turbulence driven charge separation model in order to test if the conditions that I found in the midplanes could lead to an emergence of lightning. I found that the electric fields generated in this way are not large enough for an electron avalanche to occur. An electron avalanche is mandatory for lightning to occur.

In addition, this work will show some preliminary results of the implementation of triboelectric charging. The main finding is that the dust charging distribution can change significantly if one considers triboelectric charging.

Lastly, this work also discusses my involvement in the MSG project (Jørgensen et al.) and the work I did in implementing non-equilibrium chemistry into the MARCS code. In particular, I test the impact of the Chapman cycle on the upper atmospheres of a simulated exoplanet.

Resumé

Hvor end lyn opstår, vil de have en stor indvirken på kemien. Derfor kunne lyn også have en væsentlig effekt på kemien af protoplanetariske skiver.

Linket mellem lyn og protoplanetariske skiver er ladede støvkorn, eftersom de er nødvendige for at lyn kan opstå og de findes i midtplanerne af protoplanetariske skiver. Ladede støvkorn kan spille en afgørende rolle i planetdannelsen på grund af deres interaktion med magneto-rotationsustabiliteten, og derfor kan en mere detaljeret forståelse af deres ladning give ny indsigt i planetdannelsesprocessen.

Hovedformålet med dette studie er at undersøge, hvordan støvkorn lades i midtplanerne af proplanetære skiver, hvordan de påvirker kemien og ladningsbalancen, og endelig, om de kan føre til fremkomsten af lyn. For at studere støvkorns ladeadfærd i protoplanetariske skiver benytter jeg den termokemiske skivemodel ProDiMo (Woitke et al. [2016]).

Jeg har foretaget flere forbedringer af modellen, for at muliggøre dette studie. Jeg gjorde det blandt andet muligt for modellen at inkludere flere forskellige størrelser af støvkorn, hvor modellen tidligere brugte en enkelt gennemsnitlig støvkornstørrelse. Derudover implementerede jeg en ny tilgang i ladekemien i ProDiMo, hvor vi nu kan inkludere triboelektrisk ladning i samarbejde med de andre ladningsmekanismer, såsom fotoionisering, elektronvedhæftning og ladningsudveksling mellem støvregn og molekyler. Denne tilgang med at kombinere triboelektrisk ladning og andre ladningsmekanismer er en helt ny tilføjelse til feltet. Hovedresultaterne af dette studie er, at støvkornene i midtplanerne af protoplanetariske skiver bliver den dominerende negative ladningsbærer og sammen med NH4+ dominerer ladningsbalancen.

Udover disse simuleringer udviklede jeg også en simpel turbulensdrevet lad-

ningsadskillelsesmodel for at teste om de forhold, som jeg fandt i midtplanerne, kunne føre til dannelsen af lyn. Jeg fandt ud af, at de elektriske felter, der genereres på denne måde, ikke er store nok til, at der kan opstå en elektron-lavine. En elektron-lavine er nødvendige for at lyn kan opstå.

Derudover vil dette arbejde også vise nogle foreløbige resultater af implementeringen af triboelektrisk ladning. Hovedfundet er, at ladningsfordelingen af støvkornene kan ændres væsentligt, hvis man inkluderer triboelektrisk ladning. Til slut vil dette arbejde også diskutere min involvering i MSG projektet (Jørgensen et al.) og det arbejde, jeg foretog med at implementere ikkeligevægtskemi i MARCS-koden. Især tester jeg effekten af Chapman cyklussen på den øvre atmosfære af en simuleret exoplanet.

Zusammenfassung

Wo Blitze auftreten, beeinflussen sie die Chemie auf signifikante Weise. Blitze könnten somit auch einen großen Einfluss auf die Chemie in protoplanetaren Scheiben haben. Die Verbindung zwischen Blitzen und protoplanetaren Scheiben sind geladene Staubkörner, da sie eine Voraussetzung für Blitze und in den Mittelebenen von protoplanetaren Scheiben zu finden sind. Geladene Staubteilchen können darüber hinaus eine wichtige Rolle während der Planetenentstehung spielen aufgrund ihrer Interaktion mit der Magnetorotationsinstabilität. Ein besseres Verständnis davon, wie sich Staubkörner aufladen, könnte neue Erkenntnisse für den Planetenentstehungsprozess liefern.

Der zentrale Fokus dieser Arbeit ist zu verstehen, wie Staubkörner sich innerhalb der Mittelebene von protoplanetaren Scheiben aufladen, wie sie Chemie und die Ladungsbalance beeinflussen und letztlich, ob sie die Entstehung von Blitzen möglich machen können. Um das Aufladeverhalten von Staubkörnern in protoplanetaren Scheiben besser zu verstehen, werde ich den Nutzen von dem thermochemischen Scheibenmodell ProDiMo (Woitke et al. [2016]).

Es wurden einige Verbesserungen an diesem Model von mir durchgeführt, welche eine Voraussetzung waren, um diese Arbeit zu ermöglichen. Zum Beispiel habe ich es möglich gemacht, dass das Model in der Lage ist, Staubkörner verschiedener Größen zu berücksichtigen. Dies war vorher nicht der Fall, wo lediglich eine durchschnittliche Staubkorngröße benutzt wurde. Ferner habe ich einen neuen Ansatz in die gesamte Ladungschemie von ProDiMo eingebaut, welche es nun ermöglicht den triboelektrischen Ladungsmechanismus in Kombination mit anderen Ladungsmechanismen, wie zum Beispiel, Photoionisation, Elektronenanlagerung und Ladungsaustausch zwischen Staubkörnern und Molekülen. Dieser Ansatz, triboelektrisches Laden und die anderen Mechanismen zu kombinieren, ist vollkommen neu und erstmalig angewendet in diesem

Fachbereich.

Eines der Hauptresultate dieser These ist, dass in der Mittelebene von protoplanetaren Scheiben die Staubkörner der dominierende negative Ladungsträger sind und zusammen mit positiven $NH_4{}^+$ Molekülen die Ladungsbalance dominieren. Auf der Basis dieses Resultats habe ich ein turbulentes Ladungsseparationsmodel entwickelt, um zu testen, ob die Gegebenheiten, die wir in den Mittelebenen vorfinden, dazu geeignet sind, um Blitze zu erzeugen. Es zeigt sich, dass die elektrischen Felder, die man mit dieser Methode erzeugen kann, nicht groß genug sind, um eine Elektronenlawine auszulösen. Elektronenlawinen sind eine Voraussetzung für Blitze.

Darüber hinaus wird diese Arbeit einige vorzeitige Resultate der Implementation des triboelektrischen Ladungsprozesses zeigen. Das Hauptresultat hier ist, dass sich die Staubkornladungsverteilung signifikant ändern kann, wenn man triboelektrisches Aufladen berücksichtigt.

Zu guter Letzt diskutiert diese Arbeit auch meine Teilhabe an dem MSG Projekt (Jørgensen et al.) und meine Arbeit an der Implementation von Nichtgleichgewichtschemie in den MARCS Code. Im Besonderen werde ich den Einfluss des Chapman Kreislaufs auf die oberen Atmosphärenschichten eines Testplanetens diskutieren.

Use of own published and pre-published work

In this work I will make use of my own published work

Size-dependent charging of dust particles in protoplanetary disks Can turbulence cause charge separation and lightning?.
Authors: T. Balduin, P. Woitke, U. G. Jørgensen, W.-F. Thi, and Y. Narita
Published in: Astronomy and Astrophysics, 678, A192 (2023)
https://doi.org/10.1051/0004-6361/202346442

In particular, chapter 2 of this thesis is the text and images of sections 2 and 3 of my published work.
Chapter 3 of this thesis are the text and images of section 4 and section 5 of my published work.
Chapter 4 is previously unpublished and completely original work by myself.
Chapter 5 is based on my contribution to Jørgensen et al. but does not use any of their text or plots.
Chapters 1 and 6, the introductions and conclusion are completely new and do not use any images or text from previously published work by myself .
Additionally, the appendix of this thesis also consists of the appendix of my previously published work.

Contents

1 Introduction

1.1 Outline of the Introduction

This introduction will start by giving an overview of what protoplanetary disks are and give a short summary of the current state of research in the field (Sec. 1.2).
We will then go into more detail into the areas crucial to this thesis. These will be a section on what is known about the dust grains in protoplanetary disks in general (Sec. 1.3) and known effects of charged dust grains in protoplanetary disks (Sec. 1.3.1).
We then discuss the second big topic of this thesis with a section on lightning in particular (Sec. 1.4), focusing on how lightning can emerge on earth and observations and theories of non-terrestrial lightning. We will then discuss what are the necessary conditions for lightning to emerge (Sec. 1.4.1). The, for this thesis and lightning very important, dust grain charging mechanism called triboelectric charging will be explained in Section 1.4.2

Lastly, an overview will be given on the research that already has been done in the field of lightning in protoplanetary disks 1.5.
The introduction will be concluded by an outline of the thesis overall in section 1.6.

1.2 Protoplanetary Disks

As the name might suggest to the observant reader, protoplanetary disks are the birthplace of planets. In its most fundamental form protoplanetary disks are a type of accretion disk that form around young stellar objects (YSO). They get their characteristic disk form due to the fact that the angular momentum within a collapsing molecular cloud, exceeds the amount of angular momentum that can be taken on by the YSO (Goodman et al. [1993]).

Due to the fact that protoplanetary disks are accretion disks, their lifetime is very short compared to the host star. Large amounts of material in the disk still accretes onto the host star, can get carried away by other effects such as winds and some of the material will form planets. In the classification scheme for YSO by Lada and Wilking [1984], protoplanetary disks are usually classified as Class II. They show an the excess in the infrared parts of the stellar spectrum, which hints at one major component of protoplanetary disk and that is the dust (See Fig. 1.1).

Observing protoplanetary disks can be a challenging endeavor due to the different ranges of wavelength that one would require to get a full picture of both the gas and the dust (compare Fig. 1.2). Observations in the infrared, for example with JWST, would only reveal the upper layers of the disk. If one would be interested in the lower areas where dust is abundant one would need millimeter observations, for example with ALMA.

These millimeter observations can reveal highly diverse substructures in the dust in the outer disk, with gaps and rings forming, (compare Fig. 1.3). A good example of such observations is the big MAPS survey with ALMA (Öberg et al. [2021], Ilee et al. [2021]). We can only see the outer disk structure mostly due to spatial resolution issues. At the long wavelengths that ALMA operates in even its km baseline is not large enough to allow the resolution necessary to investigate inner areas of the disk. Telescopes that operate in the near infrared

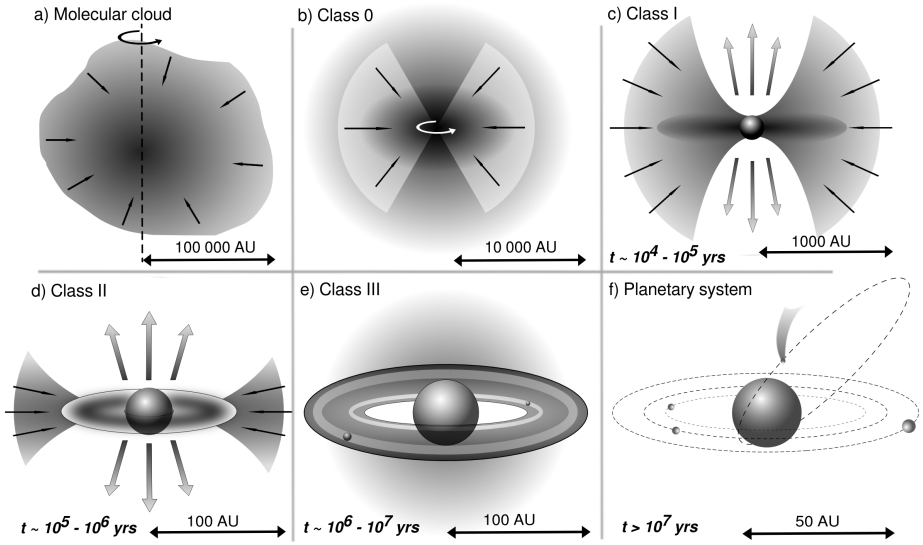

Figure 1.1: A short illustration of the star and planetary system formation process from its beginnings as a prestellar core, through the 4 stages from being classified as a class 0 to class III object onto the final planetary system. The image is taken from Drazkowska et al. [2022]. Permission for reuse granted by the creator.

like VLT/SPHERE could image the inner areas of the disk, but still not the midplane areas is, as these areas are highly opaque (compare again Fig. 1.2). The host star will also become problematic at those wavelengths as it starts to dominate the spectrum.

If one would like to study the more inner regions towards the host star observations will not be the best tool. Here computer simulations are an extremely helpful tool as it allows us to shine a light on these regions. In addition, with the notoriously long timescales of astrophysical objects compared to meager human lifetime timescales, computer simulations allow us to understand dynamical process and evolutionary processes in disks in higher detail. In this study we will make use of the the thermo-chemical disk simulation code ProDiMo (Woitke et al. [2016]) to investigate these inner areas in more detail.

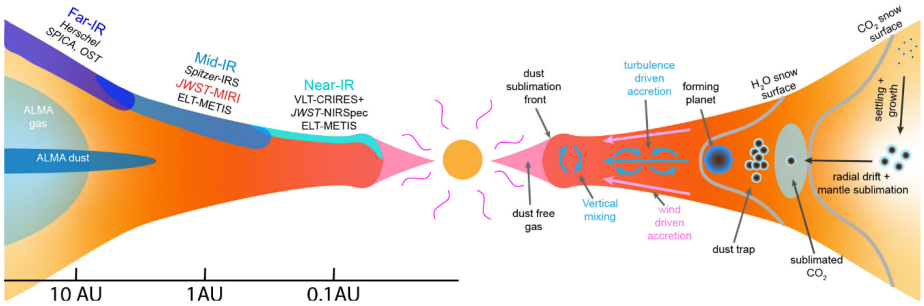

Figure 1.2: Illustration of a protoplanetary disk in edge-on view. The left hand side illustrates what parts of the disk can be imaged in which wavelength regimes and with which instrument. The right hand side gives an image of the different processes that dust grains undergo or take part in within a protoplanetary disks. Important mentions are, from right to left in the image, settling and drifting, ice formation, their concentration via dust traps and the formation of planets. Image taken from figure 1.3 of the PhD Thesis of A. Bosman (Bosman [2018]) . Permission for reuse granted by the creator.

1.3 Dust grains in protoplanetary disks

Dust grains make up only about 1 percent of the total mass of protoplanetary disks, following the dust to gas ration of the interstellar medium (ISM) (Weingartner and Draine [2001]). Since the dust grains in protoplanetary disks are a remnant of the ISM, they are made of the same material. Hence, when we talk about dust grains in protoplanetary disk we mostly talk about amorphous silicate dust grains Draine [2003] Min et al. [2006] (see Fig. 1.4).

Dust grains in disks are probably the most intriguing component of the disks because dust grains in protoplanetary disks are the basis material of planets (see reviews on planet formation such as Drazkowska et al. [2022]). In order for planets to form, dust grains within a protoplanetary disk have to accumulate. The first step of accumulation is settling. Dust grains tend to gravitationally settle into the midplane of protoplanetary disk on comparatively short timescales (Dubrulle et al. [1995], Dullemond and Dominik [2004], and Riols and Lesur [2018]). In addition to settling in the midplane dust grains also experience a drift towards the host star. This drift is induced by the dust grains experiencing drag forces when moving through the gas of the disk. These drag forces occur due to the gas and grains rotating at different velocities around the host

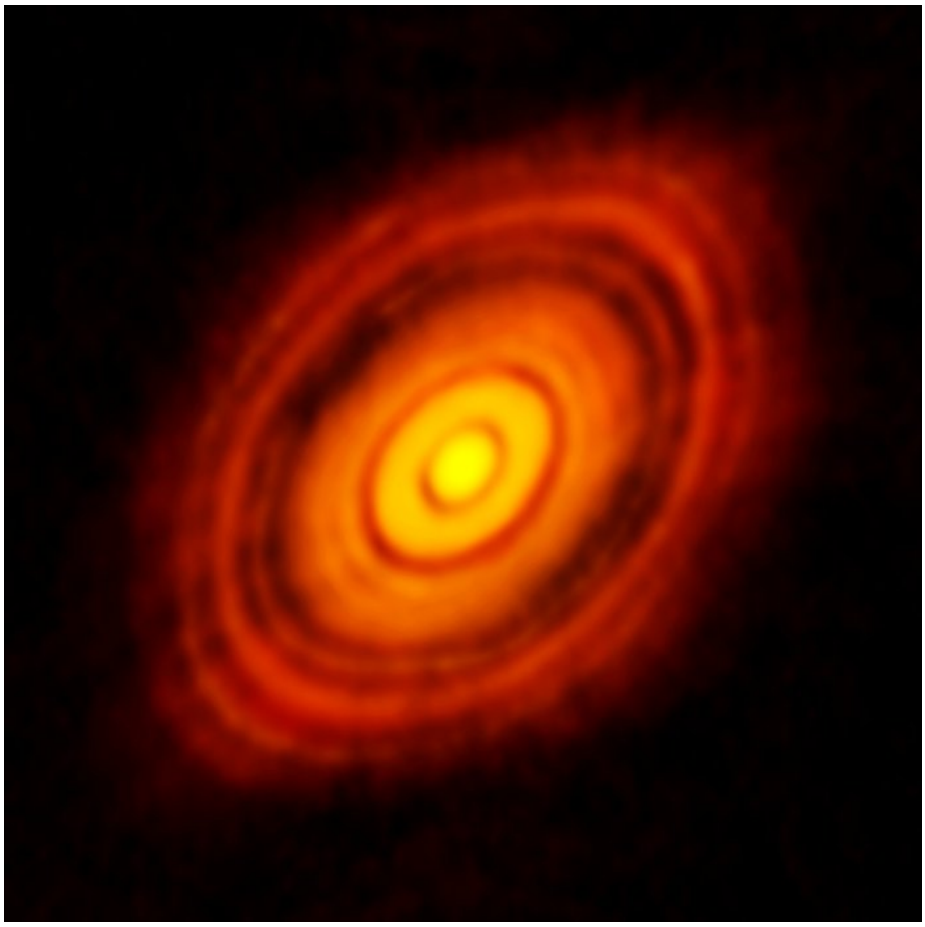

Figure 1.3: Observation of the continuum of the the protoplanetary disks around HL Tau. Image credit to ALMA (ESO/NAOJ/NRAO).

star. The dust grains rotate at Keplerian velocities and the gas rotates at sub-Keplerian velocities. These drag forces slow down the grains, resulting in the dust grains drifting inwards to match their rotation velocity to appropriate orbits (compare reviews like Birnstiel et al. [2016], Birnstiel [2023]).

Whilst settling and drifting are a first step in dust accumulation to form planets, these processes are not sufficient enough to ultimately form planets. In order to achieve a high enough concentration of dust grains, they need to be concentrated further in what are called dust or pressure traps. Once the dust grains have clustered together they could start to grow from their usual sub-micron to millimeter size to form pebbles ($\approx$ mm to cm size) and ultimately planetessimals (km sized) via collisions. But, a simple hierarchical growth, from dust grains to pebbles and then planetessimals, seems to not be possible, since several growth barriers have to be overcome in the process.

When dust grains collide, there can be several outcomes. The positive outcomes, which are the ones where at least one of the interacting particles grows, would be sticking and mass transfer. The negative ones would be bouncing, where no mass transfer occurs, or fragmentation, effectively a return to the starting point of the growth process. It has been shown that at the velocities that dust grains would have under typical midplane conditions growth beyond millimeter sizes becomes less and less likely, due the dust grains starting to bounce and fragment more often than they would stick or transfer mass with each other (compare Chapter 3 of Birnstiel et al. [2016] in particular their Fig. 2).

The question that arises here is, if it is not possible for pebbles to grow beyond cm sizes, how can larger objects like planetessimals and even ultimately planets form. A solution to this problem could be the streaming instability (Youdin and Goodman [2005] Youdin and Johansen [2007] Johansen and Youdin [2007]). Streaming instabilities achieve the clustering of dust grains by creating an area where dust grains are sheltered from the drag forces of the gas, comparable to how the outer riders of a peleton in a bike race shelter the riders inside the peleton from the wind drag. This sheltering is so effective that the accumulating pebbles can become gravitationally unstable, ultimately forming planetessimals ($\approx$ km size).

A last step in planet formation is then the ultimate growth of planetessimals towards planet sized objects. The leading theory here is pebble accretion

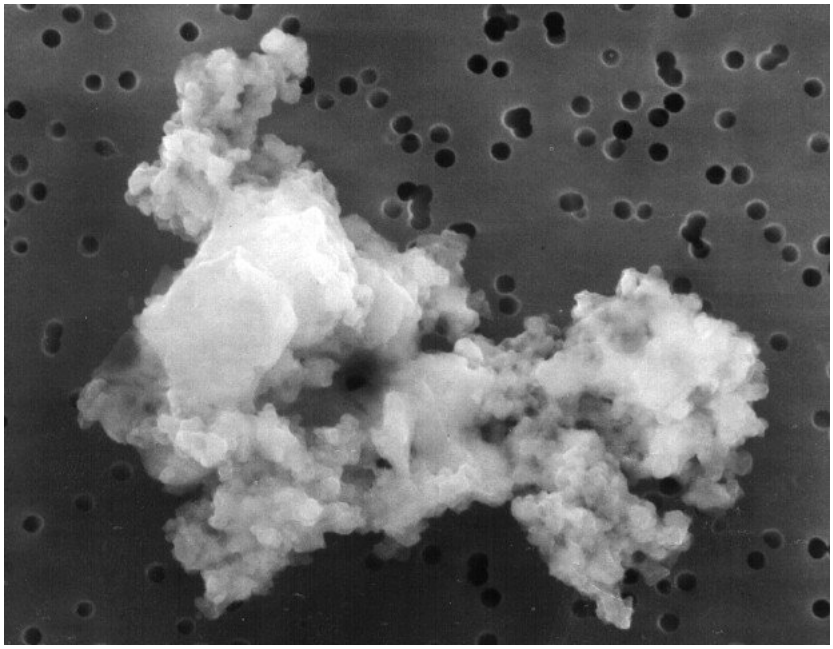

Figure 1.4: An image of an interplanetary dust grain of roughly 100 times 40 microns in sizes. It gives us an idea of how protoplanetary dust grains would look as well. One can see very well how these dust grains are aggregates of mostly smaller grains and some more crystalline components such as glasses. They also contain some organic compounds. They are very porous and it is easy to understand why they are sometimes referred to as "fluffy". Image credit to NASA.

Johansen and Lambrechts [2017], Lambrechts and Johansen [2012].

1.3.1 Effects of charged dust grains

The effects of charged dust grains are sometimes neglected in theoretical approaches due to additional complications that come when accounting for it. For example, the growth of planetessimals could be inhibited by charged dust grains (Akimkin et al. [2023], Okuzumi [2009], Okuzumi et al. [2011], and Akimkin et al. [2020]). In the important regions for planet formation, the midplane of disks, dust grains tend to charge mostly negative, due the area being well shielded. This effect of dust grains inhibiting planetessimal growth is often called the charge barrier.

But, charged dust grains could also be beneficial for the planet formation. As mentioned before, for effective planet formation to occur we require dust grains to get trapped, for example in streaming instabilities. For streaming instabilities to occur, a dust to gas ratio of the order of unity is required. In an unperturbed disk, at low enough levels of viscosity, such dust to gas ratios can be reached. But, the settling process of the dust grains could get perturbed by several instabilities.

Some of these instabilities, that could lead to dust getting perturbed like vertical shear instabilities (Nelson et al. [2013]), convective overstabilities (Klahr and Hubbard [2014]) or the so called zombie vortices (Marcus et al. [2013] Marcus et al. [2015] Marcus et al. [2016] Lesur and Latter [2016]). But the one where charged dust grains could play a role is the magneto magneto-rotational instability (MRI) (Salmeron and Wardle [2008], Suzuki et al. [2010] Perez-Becker and Chiang [2011], Bai [2011], and Thi et al. [2019]).

The MRI is an magneto-hydrodynamical (MHD) effect, occurring predominately in the midplane of disks and close to the host star. MRIs are a result of the magnetic field coupling to the weakly ionized gas exerting an influence on the gas. Due to the weak ionization of the gas, the gas particles feel the influence of the magnetic field. If the gas particles get perturbed, by for example some drifting more in wards and some drifting more outwards, the magnetic field lines would bend in accordance with this perturbation. When magnetic field lines get bend, a magnetic tension builds itself up, and in the case of MRI this tension can result in a spring like effect, where gas particles which are radially closer to the host star lose angular momentum and drift even more inwards radially, whilst the radially more outwards particles gain angular momentum and drift more outwards. An illustration of this mechanism is shown in Fig. 1.5.

However, dust grains could come to the rescue here, as they can play a role in creating so called "dead-zones" (Dullemond and Penzlin [2018], Regály et al. [2021], and Regaly et al. [2023]) where MRI does not occur and hence aid the process of dust grain concentration. We will see, that dust grains tend to get charged negatively via there reaction with electrons. As this process removes electrons from the gas and it lowers the ionization fraction of the gas. As mentioned, the gas needs to be weakly ionized for MRI to occur. In the literature we find values for the electron fraction of at least 10^{-13} at 1 AU to be a requirement for MRI to occur (compare first page of Inutsuka and Sano

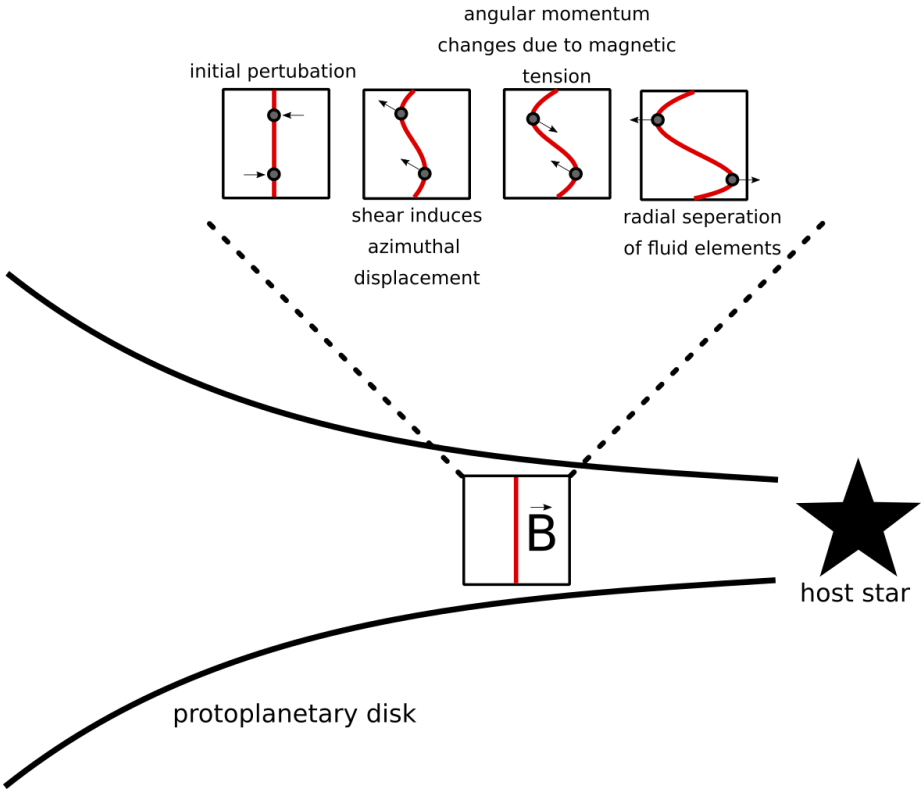

Figure 1.5: An illustration of how the magneto-rotational instability (MRI) occurs within a protoplanetary disk. The lower image is a crude representation of a protoplanetary disk with an arbitrary chosen box of gas at distance r from the host star. We then zoom into this box and show 4 stages of how MRI can develop. The first image just shows the magnetic field as a red vertical line and two particles in the disk that are coupled to said field and experience an initial perturbation The crucial parts in understanding this instability are the second and third box. Firstly the particles experience different azimuthal displacement due to the shear in the disk. The magnetic field counteracts this displacement via magnetic tension, resulting in the upper particle to lose angular momentum and the lower particle to gain angular momentum. The fourth box shows the end result of the upper particle drifting inwards radially and the lower particle outwards. The figure is a creation of my own but inspiration was taken from figure 1.18 in Armitage and Kley [2019]

[2005]). We will see that the charging of dust grains can lower this fraction by orders of magnitude and therefore be responsible for the creation of dead zones and potentially aid in the planet formation process. This whole effect will get discussed in higher detail in chapter 2 of this thesis.

1.4 Lightning

The fascination with lightning might be one of humankind's longest lasting. To our ancestors the fire of the sky had to be of divine origin, only this way could its destructive force be explained, cast from sky-bound deities, either named Zeus, Thor or Indra. Nowadays we of course know that lightning is created from much more earthly origins. But, its fascination has not waned in the slightest. Studying lightning is an interesting endeavor due to its chemical implications.

Lightning discharges on Earth are accompanied by very high temperatures, exceeding 40000 K (Orville [1968a] Orville [1968b] Orville [1968c]). These high temperatures can result in chemical processes occurring which would be impossible otherwise. For example these high temperatures are capable of splitting molecular nitrogen into its atomic components. The atomic nitrogen is then further capable of forming nitrogen oxygen compounds NO_x. These nitrogen oxygen compounds play an important role in the abiotic fixation of nitrogen (Noxon [1976] Hill et al. [1980] Price et al. [1997]). Hence, Lightning could therefore have played an important role in the prebiotic fixation of nitrogen (Navarro-González et al. [2001]), and fundamentally influenced how life formed on this planet.

Additionally, Lightning, and the resulting nitrogen oxygen compounds, could have also played an integral part in the generation of the first ozone molecules in the atmospheres (Wild [2007] Murray et al. [2013]). Whilst in today's atmosphere, the ozone layer is held up by the Chapman cycle (Chapman [1930]), the ozone that is required for this cycle to work has to be seeded into the atmosphere in the first place. Here the nitrogen oxygen compounds are also important as the photodissociation of NO_2 results in in atomic oxygen, which can then react to ozone together with molecular oxygen.

However, lightning is not a phenomenon exclusive to earth. There have been direct observations of lightning in other solar system objects such as Venus (Russell et al. [2006] Russell et al. [2007] Russell et al. [2008]) and Saturn (Baines et al. [2009] Dyudina et al. [2010]). For planets outside of the solar system we at this point only have theoretical proof of lightning and its impact (Braam et al. [2022] Braam et al. [2023]).

1.4.1 Lightning Mechanisms

For lightning to emerge, certain conditions have to occur. In my own studies of the topic I started to summarize these conditions as the 2 D's, difference and distance (see Fig. 1.6 for an illustration).

Difference describes the fact that in order for lightning to occur one needs chargeable particles, but there needs to be a factor where these chargeable particles are different from one another. For example, one could have different types of material that charge in a different manner, as is in the case in thunderclouds on earth, where ice crystals and graupel are the chargeable particles (Takahashi [1978] Jayaratne et al. [1983] Saunders [1993] Saunders and Peck [1998]). But, one could also use materials of the same kind, for example dust grains, and have them be different in another aspect. One aspect could be for example their size. This is typically found in lightning in volcanic plumes on earth (Houghton et al. [2013]) where dust grains of different sizes are present. In protoplanetary disks the aspect of size could also be a candidate as the differing aspect.

In order to have an electric discharge such as lightning we need to also discuss the other factors of the 2 D's and that is distance. Distance in this context means that in order to generate an electric field large enough for lightning to emerge we have to bring a large enough distance between the charged particles. On earth, inside of thunderclouds, this is usually provided by the updraft wind, where particles of different sizes would be drag along more or less effectively and therefore separated Stolzenburg et al. [1998] Bruning et al. [2007]. Another way of separating charged particles can be found in volcanic eruptions Brook et al. [1974] Gaudin et al. [2018] or dust devils Yair [2012]. Both phenomena separate charges via rotational energy. So smaller particles would tend to be located more on the inside and larger particles would get carried to the outside. Turbulence, understood as a superposition of eddies, would be the prime candidate in providing the rotational energy needed for charge separation to occur in such a manner.

Lastly, when the electric field generated by charge separation is large enough to accelerate electrons fast enough, so that their kinetic energy is larger than the ionization energy of the air molecules in the atmospheres, an electron avalanche occurs (Townsend [1902]). This electron avalanche will result in the dielectric breakdown of the air which creates the lightning arc.

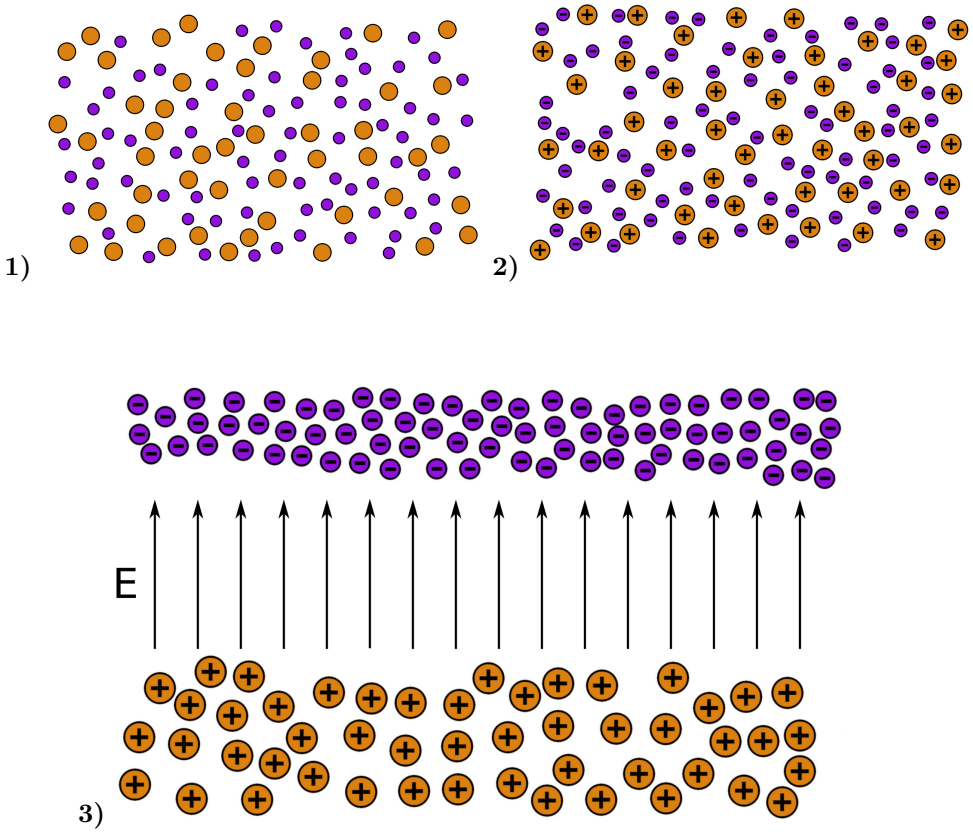

Figure 1.6: Short illustration of the necessary requirements for lightning to emerge. Images 1 and 2 illustrate that we need different particles (here orange and purple) that differ in one aspect, here for example size. These particles would then need to get charged in a different manner, here for example the larger ones becoming more positive and the smaller ones more negative. One charging mechanism that could achieve this is triboelectric charging. Image 3 illustrate the last step which is the fact the we need to distance these particle populations from each other. Mechanisms that could achieve this are for example gravity or turbulent vortices

1.4.2 Triboelectric Charging

Triboelectric charging in its simplest form is a charging mechanism where two objects exchange charges when they come in contact with each other. Triboelectric charging is a charging process that should be very familiar to the reader, as there are several everyday examples of triboelectric charging. For example the building up of an electrostatic potential when one walks with thick soled running shoes on linoleum floors is an effect of triboelectric charging. An occurrence that, very curiously, happened quite often at both institutes where this thesis was created at.

Triboelectric charging is very relevant to this work as it has been shown to charge particles of different sizes in different manners, for example in earth clouds (Baker et al. [1987] Dash et al. [2001]) or volcanic plumes (Houghton et al. [2013]). The tendency here is that smaller particles tend to be charged more negatively than larger particles (Lacks and Levandovsky [2007] Forward et al. [2009]).

What is at the core of triboelectric charging is the fact that when two materials with different workfunctions interact with each other, they exchange charges (Matsusaka et al. [2010] Lacks and Shinbrot [2019]). Whether one material accepts charges or donates charges in this process depends on their respective workfunctions, and can be looked up in the triboelectric series (Seol et al. [2018] Zou et al. [2020]). Triboelectric interactions can also lead to large amounts of charge exchanges compared to other charge exchange mechanisms. In photoprocesses or chemical reactions the amounts charge exchanged are often just one singular charge entity, usually an electron that either gets absorbed or emitted. But for example in Jungmann et al. [2021] we can see that for sub millimeter sized silicate particles, the amounts of charges exchanged can be in the tens of thousand.

We have chosen to investigate triboelectric charging for several reasons. Firstly, related to lightning, we know already from volcanic eruptions on Earth that dust particles can be triobelectrically charged, and enough for lightning to emerge (Houghton et al. [2013]). Secondly, related to the implications of charged dust grains in general, the literature reveals that triboelectric charging could be instrumental in planet formation, by helping to overcome the bouncing barrier (Jungmann and Wurm [2021]) and also have implications in ionizing the

gas around the dust grains (Wurm et al. [2022]).

1.5 Previous research on Lightning in Protoplanetary Disks

it is important to point out that exploring lightning in protoplanetary disks is not an entirely unique concept and has been theorized and investigated beforehand. This is due to the similarities between lightning emergence on Earth and the conditions found in protoplanetary disks. Midplanes of protoplanetary disks show very high dust grain number densities, therefore the required material for lightning would is present in abundance. Additionally dust traps or the turbulence induced by the rotation of the disk could results in the necessary dynamics that are needed for lightning to emerge.

Lightning in protoplanetary disks has often been a candidate to explain the occurrence of particles in the disk that would require high temperatures to occur. Examples of this are for example highly ordered and crystalline silicate dust grains as found in EX Lupi Ábrahám et al. [2009], or the creation of chondrules Desch and Cuzzi [2000]. But, in both cases, the ultimate proof that lightning is responsible for their creation is still lacking.

A fundamental work, is for example Muranushi [2010]. In that work a critical dust number density is calculated in order to determine if lightning can occur. One critical difference between their work is the lack of dynamics whilst this thesis considers dynamical processes. Just having enough charged dust grains will not be sufficient for lightning to emerge, a separation still needs to occur. In this work we will develop a simple charge separation model via turbulence. Additionally, they only consider triboelectric charging and no other charging processes. This thesis will combine all charging effects, which is the first time such an approach has been done in the field.

Very important to mention is the works of Okuzumi and Inutsuka [2015] and Okuzumi et al. [2019]. Whilst not necessarily studying lightning, they study different ways of how electric fields could be generated in disks via the MRI. Lastly one should also mention Johansen and Okuzumi [2017], where they investigate lightning discharge via positron emission of pebbles that contain radioactive Al^{26}. A difference to the approach discussed here is that the ionization mostly

comes from cosmic rays and not radioactivity.

1.6 Outline of the Thesis

Chapter 2 discusses the charging of dust grains in a thermo-chemical model. The theoretical framework for this thesis will be discussed and it will be explained how the model disk is setup, what advancements had to be made to the code to investigate dust grain charging and how the chemistry in the midplane is impacted by dust grain charging.
Chapter 3 discusses the simple turbulent charge separation model that was developed to investigate if lightning could emerge with the results that were found in chapter 2.
Chapter 4 discusses how triboelectric charging was implemented into the code and what the preliminary results are of including this charging mechanism into the dust charging chemistry.
Chapter 5 is a short summary of my involvement into the MSG project at my secondment University in Copenhagen, where I helped the implementation of non-equilibrium chemistry into a different code.
Chapter 6 is a conclusion of the different chapters 2-5 and an overall summary of the thesis.

2

On the implications of dust grain charging within protoplanetary disks

In this chapter the numerical and theoretical outline that is necessary to investigate dust grain charging with the Prodimo code will be explained. This chapter will be taken from section 2 and section 3 of my previous publication Balduin et al. [2023] handling the topic with some adjustments to fit the format of a thesis.

The text and plots of this Section were all done by me. The numerical formulation of dust grain moments and its implementation into the ProDiMo code are based on the work of the coauthor Wing-Fai Thi. There have also been significant feedback by my coauthor Peter Woitke.

2.1 The thermo-chemical disk model

To simulate the size-dependent charging of dust grains in a protoplanetary disk, we used the Protoplanetary Disk Model (ProDiMo) developed by Woitke et al. [2009, 2016]. ProDiMo is a 2D thermo-chemical disk modeling code that combines detailed continuum and line radiative transfer with the solution of a chemical network, the determination of the non-local thermal equilibirum (LTE) population of atomic and molecular states, and the heating-cooling balance for both gas and dust.

The model uses a simple parametric density setup chosen to represent a 2 Myrs old T Tauri star. All further assumptions about the star; the disk shape; the irradiation of the disk with FUV photons, X-rays, and cosmic rays; the dust material composition and opacities; and dust settling are explained in detail in [Woitke et al., 2016, see their table 3]. Here, in this publication, we only explain the changes made to the ProDiMo code that differ from the code used in Woitke et al. [2016], and differences to the setup from Woitke et al. [2016]. The selected values for the stellar, disk shape, and dust parameters are summarized in Table 2.3.

2.1.1 Chemical setup

We choose the so-called large DIANA-standard chemical network with 235 species as our base network for this work. It has been described in detail by Kamp et al. [2017]. Most UV, cosmic ray, two-body, and three-body reaction rates are from the UMIST 2012 database Woodall et al. [2007], McElroy et al. [2013]. In addition, there are rates for the H_2 formation on grains, reactions for electronically excited molecular hydrogen $H_2^\star$, polyaromatic hydrocarbon (PAH) charge chemistry Thi et al. [2019], and a simple freeze-out chemistry for the ice phases of all neutral molecules (see Woitke et al. [2009] and Kamp et al. [2017]). The large DIANA-standard network also includes X-ray processes with doubly ionized species from Aresu [2012].

We added a number of dust species to this base chemical network to represent the different charging states q of grains of different sizes a. By solving the chemical rate network, we determined the dust charge distribution function for every given size and charge $f(a, q)$ from which we could then compute, for

example, the mean charge of grains of different sizes, including the feedback of the charged grains on all other results of the chemistry.

In contrast to Woitke et al. [2016], we have chosen to omit the PAH charging states in the chemistry in this paper, but PAH heating is still taken into account. If present, the PAHs can introduce similar effects as charged grains. Since we want to study the chemical feedback of charged grains in disks in particular, we wanted to avoid any confusion between PAH charging and dust charging. In addition, preliminary tests showed that the impact of PAHs in the midplane is negligible, due to the PAHs freezing out. Therefore, we also omitted them to lower the numeric effort.

2.1.2 Dust size distribution and settling

In ProDiMo, the dust component enters into the modeling (i) as an opacity source for the continuum, (ii) its effect on line radiative transfer, and (iii) as a set of chemical species that can pick up and release charges in the chemical rate network. The dust grains, however, are neither created nor destroyed, nor do they grow in the chemistry module.

Our assumptions about dust settling and opacity are explained in Woitke et al. [2016]. The dust size distribution function before settling [cm^{-1}] is assumed to be

$$f_0(a) \propto a^{-a_{\mathrm{pow}}} \ , \tag{2.1}$$

which is the same everywhere in the disk, using N_{size} log-equidistant size grid points between the minimum grain radius a_{min} and the maximum radius a_{max}. The proportionality constant in Eq. (2.1) is derived from the local gas density $\rho(r,z)$, the dust material density ρ_{gr}, and the global gas-to-dust mass ratio, assumed to be 100 in this paper. In each vertical column at radius r, all grains of size a are vertically redistributed with a scale height that is smaller than the gas scale height. Here, in this publication, we used the settling description by Dubrulle et al. [1995] with the settling parameter $\alpha_{\mathrm{settle}} = 0.01$, as outlined in Woitke et al. [2016]. After applying the settling, the dust size distribution function $f(a,r,z)$ is numerically available on the N_{size} size grid points at each point (r,z) in the model. The term $f(a,r,z)$ is the basis for the opacity calculations.

2.1.3 Dust size bins in the chemistry

We used a much smaller number of dust size bins $N_{\rm bin}$ (between two and nine) to represent the position-dependent dust size distribution function after settling $f(a,r,z)$ in the chemistry. The idea in this section is to introduce two power-law indices, κ and ζ, to make the sparse representation exact with regard to two selectable dust size moments. We then argue which of the dust size moments should be selected in order to minimize the numerical errors in the chemistry introduced by the sparse resolution of $f(a,r,z)$ in size space. We start by computing the following moment of the dust size distribution function

$$\langle a^{\zeta}\rangle(r,z) = \int_{a_{\rm min}}^{a_{\rm max}} f(a,r,z)\, a^{\,\zeta}\, da \ , \tag{2.2}$$

where $f(a,r,z)$ [cm^{-1}] is normalized as $\int_{a_{\rm min}}^{a_{\rm max}} f(a,r,z)\, da = 1$. For example, $\zeta{=}2$, $n_d\, 4\pi\, \langle a^2\rangle$ is the total dust surface per cubic centimeter [cm^2/cm^3]. Next, we divide $\langle a^{\zeta}\rangle$ by $N_{\rm bin}$ and numerically adjust the bin boundaries a_j such that each size bin contains the same portion of $\langle a^{\zeta}\rangle$.

$$\langle a^{\zeta}\rangle_j = \int_{a_{j-1}}^{a_j} f(a,r,z)\, a^{\,\zeta}\, da = \frac{\langle a^{\zeta}\rangle(r,z)}{N_{\rm bin}} \ . \tag{2.3}$$

Here, a_j terms are the size bin boundary values, where $a_0 = a_{\rm min}$ and $a_{N_{\rm bin}} = a_{\rm max}$. Once the a_j are fixed this way, we compute similar quantities

$$\langle a^{\kappa}\rangle_j = \int_{a_{j-1}}^{a_j} f(a,r,z)\, a^{\,\kappa}\, da \tag{2.4}$$

and define the average size of our grains [cm] in the dust bin j as

$$\bar{a}_j = \left(\frac{\langle a^{\zeta}\rangle_j}{\langle a^{\kappa}\rangle_j} \right)^{1/(\zeta-\kappa)} \ . \tag{2.5}$$

Finally, the dust particle densities [cm^{-3}] in the size bin j are calculated as

$$n_{{\rm d},j} = n_{\rm d}(r,z) \frac{\langle a^{\kappa}\rangle_j}{(\bar{a}_j)^{\kappa}} . \tag{2.6}$$

Table 2.1: Construction of dust size bins for the chemistry[(1)].

	bin 1	bin 2	bin 3	bin 4	total
$\kappa = 0$ and $\zeta = 2$					
$\bar{a}_j$ [μm]	0.0636	0.122	0.316	1.72	
$n_{\mathrm{d},j}$ [cm^{-3}]	1.36(-4)	3.70(-5)	5.48(-6)	1.85(-7)	**1.78(-4)**
length [cm^{-2}]	8.63(-10)	4.50(-10)	1.73(-10)	3.18(-11)	1.52(-9)
area [cm^{-1}]	6.89(-14)	6.89(-14)	6.89(-14)	6.89(-14)	**2.76(-13)**
dust volume	1.46(-19)	2.80(-19)	7.27(-19)	3.96(-18)	5.11(-18)
$\kappa = 1$ and $\zeta = 2$					
$\bar{a}_j$ [μm]	0.0645	0.125	0.337	2.29	
$n_{\mathrm{d},j}$ [cm^{-3}]	1.32(-4)	3.51(-5)	4.83(-6)	1.04(-7)	1.72(-4)
length [cm^{-2}]	8.51(-10)	4.39(-10)	1.63(-10)	2.39(-11)	**1.48(-9)**
area [cm^{-1}]	6.89(-14)	6.89(-14)	6.89(-14)	6.89(-14)	**2.76(-13)**
dust volume	1.48(-19)	2.87(-19)	7.75(-19)	5.27(-18)	6.48(-18)
$\kappa = 0$ and $\zeta = 3$					
$\bar{a}_j$ [μm]	0.335	329	1070	2180	
$n_{\mathrm{d},j}$ [cm^{-3}]	1.78(-4)	1.88(-13)	5.45(-15)	6.43(-16)	**1.78(-4)**
length [cm^{-2}]	5.97(-9)	6.19(-15)	5.84(-16)	1.40(-16)	5.97(-9)
area [cm^{-1}]	2.51(-12)	2.56(-15)	7.86(-16)	3.85(-16)	2.52(-12)
dust volume	2.81(-17)	2.81(-17)	2.81(-17)	2.81(-17)	**1.12(-16)**

[(1)]Results for an unsettled dust size distribution with $a_{\min} = 0.05\,\mu$m, $a_{\max} = 3$ mm, $a_{\mathrm{pow}} = 3.5$, grain material density $\rho_{\mathrm{gr}} = 2.094\,\mathrm{g/cm^3}$, gas-to dust ratio 100, and gas density $n_{\langle \mathrm{H} \rangle} = 10^{10}\,\mathrm{cm^{-3}}$, using $N_{\mathrm{bin}} = 4$. The consecutive lengths are calculated as $\bar{a}_j\, n_{\mathrm{d},j}$, the surface areas as $4\pi\, \bar{a}_j^2\, n_{\mathrm{d},j}$, and the volumes as $(4\pi/3)\, \bar{a}_j^3\, n_{\mathrm{d},j}$. The correct total values are marked in bold: $n_d = 1.78 \times 10^{-4}\,\mathrm{cm^{-3}}$, length $= 1.48 \times 10^{-9}\,\mathrm{cm^{-2}}$, area $= 2.76 \times 10^{-13}\,\mathrm{cm^{-1}}$, and volume $= 1.12 \times 10^{-16}$.

From Eqs. (2.3) to (2.6), it follows that

$$\begin{aligned} n_{\mathrm{d},j}\,(\bar{a}_j)^{\kappa} &= n_{\mathrm{d}}(r,z) \int_{a_{j-1}}^{a_j} f(a,r,z)\, a^{\,\kappa}\, da \\ n_{\mathrm{d},j}\,(\bar{a}_j)^{\zeta} &= n_{\mathrm{d}}(r,z) \int_{a_{j-1}}^{a_j} f(a,r,z)\, a^{\,\zeta}\, da \ , \end{aligned}$$

which means that our dust bins $\{(n_{\mathrm{d},j}, \bar{a}_j) \,|\, j = 1, \ldots, N_{\mathrm{bin}}\}$ exactly represent two dust size moments where the dust size distribution function is weighted with a^{κ} and a^{ζ}, respectively (see Table 2.1).

If $\kappa = 0$ is chosen, the quantity $\langle a^{\kappa} \rangle_j$ becomes the fraction of dust particles having sizes between a_{j-1} and a_j, and consequently, the total dust number density $n_{\mathrm{d},1} + n_{\mathrm{d},2} + \ldots + n_{\mathrm{d},N_{\mathrm{bin}}} = n_{\mathrm{d}}$ becomes exact. In a similar way, choosing

$\zeta = 2$ causes the representation of the total dust surface to be exact. All other dust size moments, however, show deviations from their true integral values. Increasing the number of dust bins N_{bin} would reduce these problems.

Thus, with κ and ζ, we can choose two dust size moments that are represented exactly by the bins and are most relevant for the problem at hand. Since the effects of the charged grains in the chemistry, via their collisional and photoionization rates, scale with their total cross-section, a choice of $\zeta = 2$ seems appropriate. That scaling, however, is not exact because there are second-order dependencies of the rates on grain charge over radius q/a (see Sect. 2.1.8). In addition, the conservation of the total charge is an important principle. The total number of elementary charges on the grains per volume, assuming $q/a = \mathrm{const}$ is valid (see Sect. 2.1.8), is

$$Q = n_{\mathrm{d}} \int_{a_{\mathrm{min}}}^{a_{\mathrm{max}}} q(a)\, f(a)\, da \;\approx\; n_{\mathrm{d}} \left(\frac{q}{a}\right) \int_{a_{\mathrm{min}}}^{a_{\mathrm{max}}} a\, f(a)\, da \;. \tag{2.7}$$

Therefore, it seems important to get the first dust size moment correct as well. In contrast, there is no direct link between the total dust particle density and the chemistry nor to any dependencies of the chemistry on the total dust volume. Therefore, our default choice is $\kappa = 1$ and $\zeta = 2$.

Table 2.1 shows that in this case, we only need to represent the smaller grains up to a few microns in size. A larger value of ζ would also come with an increased level of computational problems and computing time, for example, because we would need to extend the maximum number of charging states q_{max} to many thousands for large grains (see Sect. 2.1.8).

2.1.4 Dust charging reactions

The charging of dust grains is part of the chemistry of ProDiMo. We focus only on the most relevant reactions here. A full description of all considered dust grain charging processes can be found in Thi et al. [2019]. The three most important reaction types are electron attachment, photoionization, and charge exchange between dust grains and molecular ions.

(A) Photoionization. Photoionization describes the process of stripping away electrons from the dust grains via photons with sufficiently high energies.

$$\mathrm{Z} + h\nu \;\rightarrow\; \mathrm{Z}^{+} + e^{-}, \tag{2.8}$$

where Z and Z^{+} stand for grains with charges q and $q+1$, respectively. Here, q can have any integer value greater than zero.

For positively charged and neutral grains, this process is called photoejection, and for negatively charged grains, this process is called photodetachment. According to Weingartner and Draine [2001], the energy threshold for photoejection is

$$h\nu_{\mathrm{pe}} = \mathrm{IP} = W_0 + W_c \ , \tag{2.9}$$

where IP is the ionization potential of the dust grain and W_0 the work function of silicate grains, assumed to be 8 eV by Cuzzi et al. [2001] after measurements of Feuerbacher and Fitton [1972]. The term W_c is an additional term that is dependent on the charge of the grain, and it increases the ionization potential for positive grains, making it harder to ionize the grain or decreasing the ionization potential and making it easier to ionize the grain. This additional term, W_c, is defined as

$$W_c = \left(q + \frac{1}{2}\right)\frac{e^2}{a}, \tag{2.10}$$

where q is the charge of the grain normalized by the elementary charge, e is the elementary charge, and a is the grain radius. We note that the factor 1/2 is still open for discussion according to Wong et al. [2003], where a factor of 3/8 was proposed. For photodetachment, the threshold photon energy $h\nu_{pd}$ is equal to the grain electron affinity EA plus the minimum energy E_{min} at which the tunneling probability becomes relevant.

$$h\nu_{\mathrm{pd}} = \mathrm{EA}(q+1, a) + E_{\mathrm{min}}(q, a) \tag{2.11}$$

$$\mathrm{EA}(q, a) = W_0 - E_{\mathrm{bg}} + \left(q + \frac{1}{2}\right)\frac{e^2}{a} \tag{2.12}$$

$$E_{\mathrm{min}}(q, a) = -(q+1)\frac{e^2}{a}\left[1 + \left(\frac{27\mathring{A}}{a}\right)^{0.75}\right]^{-1}, \tag{2.13}$$

where E_{bg} is the band gap, assumed to be 5 eV in Weingartner and Draine [2001]; a is the dust grain radius; and q is the grain charge in units of the electron

charge. For the total rate coefficient of photoionization, one has to combine both photodetachment and photoejection. The rate coefficient therefore takes the form of

$$k_{\rm ph}(q) = \pi a^2 \int_{\nu_{\rm pe}(q)}^{\nu_{\rm max}} \eta_{\rm eff}\, Q_{\rm abs}\, J_\nu \, d\nu \;+\; \pi a^2 \int_{\nu_{\rm pd}(q)}^{\nu_{\rm max}} \eta_{\rm pd}\, Q_{\rm abs}\, J_\nu \, d\nu, \tag{2.14}$$

where J_ν is the direction-averaged flux of photons per area and second [$\mathrm{cm^{-2}s^{-1}}$]; $\nu_{\rm pe}$ is the threshold frequency of photoejection; $\nu_{\rm pd}$ is the threshold frequency for photodetachment; $\nu_{\rm max}$ is the maximum frequency of photons, being equivalent to an energy of 13.6 eV in ProDiMo; $Q_{\rm abs}$ is the frequency-dependent absorption efficiency; $\eta_{\rm eff}$ and η_{pd} are the yields of the photoejection and photodetachment Weingartner and Draine [2001] of silicate; and a is the dust grain radius.

(B) Electron attachment. The rate coefficient for electron attachment,

$$\mathrm{Z} + e^- \;\rightarrow\; \mathrm{Z}^-, \tag{2.15}$$

is derived by averaging over the Maxwellian velocity distribution of the impinging electrons. Here Z and Z^- stand for grains with charges q and $q-1$, respectively, where q can have any integer value less than or equal to zero. This results in a reaction coefficient $k_e(q)$ of the form

$$k_e(q) = n_e S_e \sqrt{\frac{8 k_b T}{\pi m_e}}\, \sigma_Z\, f_q, \tag{2.16}$$

where n_e is the electron density, S_e is a sticking coefficient assumed to be larger than 0.3 Umebayashi and Nakano [1980] and set to 0.5 in our simulations, T is the gas temperature, m_e is the electron mass, and k_b is the Boltzmann constant. The dust grain cross-section is represented by $\sigma_Z = \pi a^2$, and a is the dust grain radius. The term f_q is a charge-dependent factor that is derived by taking the Coulomb interaction between the incoming electron and charged grain into account. For neutral grains, we have $f_q = 1$. For positively charged grains ($q > 0$), there is an additional attraction that enlarges the rate, and for negatively charged grains ($q < 0$), there is Coulomb repulsion

$$f_q = \begin{cases} 1 + \frac{W_c}{kT} & W_c > 0 \\ 1 & W_c = 0 \\ \exp \frac{W_c}{kT} & W_c < 0 \end{cases}, \tag{2.17}$$

(C) Charge exchange. Dust grains can get charged via charge exchanges between dust grains and molecular ions. The most prevalent charge exchange for this study is the exchange of a negative charge between a negatively charged dust grain and a positively charged molecular ion,

$$\mathrm{Z}^- + \mathrm{M}^+ \;\rightarrow\; \mathrm{Z} + \mathrm{M}. \tag{2.18}$$

The general form of the rate coefficient is similar to the electron attachment. Since we only allowed for exothermal charge exchange reactions, the rate coefficient takes the form

$$k_{\mathrm{ex}}^M(q) = n_M S_M \sqrt{\frac{8kT}{\pi m_M}}\, \sigma_Z\, f_q^M, \tag{2.19}$$

where, analog to Eq. (2.17),

$$f_q^M = \begin{cases} 1 - \frac{q\, q^{\mathrm{M}} e^2}{a\, kT} & q\, q^{\mathrm{M}} < 0 \\ 1 & q\, q^{\mathrm{M}} = 0 \\ \exp\left(- \frac{q\, q^{\mathrm{M}} e^2}{a\, kT} \right) & q\, q^{\mathrm{M}} > 0 \end{cases}, \tag{2.20}$$

where n_M is the density of the molecules, q^M is the charge of the impinging molecule (usually +1), S_M is a sticking coefficient set to one Thi et al. [2019], n_M is the number density of the molecule, and m_M is the molecular mass.

We note that we excluded passive ion attachment in our network. Meaning, in our network, molecules and dust grains cannot attach to each other via electromagnetic forces only. We discuss the potential implications of including passive ion attachment in Section 3.3.

We excluded endotherm charge exchange reactions between protonated molecules and dust grains, where the work function minus the band gap plus the proton affinity of the molecule exceeds 13.6 eV (see App. A.3 and Tab. 2.2). In order to identify these endotherm charge exchange reactions, we needed to know the heat of formation of negatively charged dust grains $H_f^0(Z^q)$, which is given by

the work function minus the band gap plus small correction terms of order e^2/a (see App. A.3). In our model, we consider porous silicate grains internally mixed with amorphous carbon (see Tab. 2.3), but these grains can also be ice coated. For pure silicate grains, values for the work function minus the bad gap lie between about 3 eV and 8 eV Weingartner and Draine [2001]. Yet, following the explanations of Helling et al. [2011] and looking at the compiled values of work functions of different dust components from Desch and Cuzzi [2000] and Kopnin et al. [2004], a value between 2 eV and 6 eV seems appropriate. In this paper, we use $H_f^0(Z^q) = q \times 5.89\,\mathrm{eV}$, where $q < 0$ for negative grains, 0 for neutral grains and $q > 1$ for positive grains, in accordance with Thi et al. [2019]. This is supported by Rosenberg [2001], who stated that a mixture of dust grain material tends to lower the work function overall. According to the data collected by Thi et al. [2019], water ice (coated) grains should have higher work functions. We can assume that our dust grains are water ice coated according to D'Angelo et al. [2019], who showed that at temperatures of 300 – 500 K, a water layer should be found on dust grains. This is further supported by Thi et al. [2020], who showed, with a ProDiMo model similar to ours, that phyllosilicates can be found in the midplane of a protoplanetary disk.

2.1.5 Chemical network adjustment for charge and proton exchange reactions

Particular to this work is that the code has the ability to automatically generate all possible charge exchange reactions between molecules and dust grains and proton exchange reactions between molecules and then add them to the network if they meet certain criteria. In addition, we allowed the code to add endothermic reactions to the network if they meet a predetermined requirement. We tested the implications of the different networks this creates in App. A.1.

Proton exchange reactions. Proton reactions come in the following form:

$$\mathrm{M_1} + \mathrm{M_2H^+} \longleftrightarrow \mathrm{M_1H^+} + \mathrm{M_2}, \tag{2.21}$$

where $\mathrm{M_1}$ and $\mathrm{M_2}$ are neutral molecules while $\mathrm{M_1H^+}$ and $\mathrm{M_2H^+}$ are the corresponding protonated molecules. We started our procedure by first identifying pairs of molecules and their protonated counterpart $(\mathrm{M_1}, \mathrm{M_2H^+})$. If a reaction

for the pair already exists in the network, we simply moved on. However, if a reaction between the pair was not found in the network, we added an approximated reaction to the network with certain assumptions.

The aim was to create a reaction rate with the Arrhenius equation,

$$k_{\rm ex}(T) = \alpha \left(\frac{T}{T_0}\right)^{\beta} {\rm e}^{-\gamma/T}, \tag{2.22}$$

where T_0 refers to the reference temperature of 293 K. In order to achieve this, we had to provide the different factors α, β, and γ. For α and β, we find their values with the following method. For each unprotonated molecule, $\rm M_1$, we counted how many protonation reactions for $\rm M_1$ already exist in the network. We summed up the different α_i and β_i parameters of the existing reactions. We averaged the summed-up parameters by simply dividing them by the number of reactions found in the network, $n_{\rm reac}$:

$$\alpha_{\rm mean} = \frac{1}{n_{\rm reac}} \sum \alpha_i, \tag{2.23}$$

$$\beta_{\rm mean} = \frac{1}{n_{\rm reac}} \sum \beta_i. \tag{2.24}$$

If we only found one reaction, we assumed $\alpha_{\rm mean}$ to be 5×10^{-10} and $\beta_{\rm mean}$ to be -0.5. We then checked pairs of unprotonated and protonated molecules ($\rm M_1, M_2H^+$) and created reaction rates with the calculated $\alpha_{\rm mean}$ and $\beta_{\rm mean}$ and the corresponding product ($\rm M_1H^+, M_2$). Lastly, we needed to calculate γ given by the reaction enthalpy ΔH_r (Eq. 2.25. This was done by taking the difference of the heats of formation of the products and reactants H_f^0, with data taken from measurements at 0 K from Millar et al. [1997].

$$\Delta H_r = H_f^0(M_1H^+) + H_f^0(M_2) - H_f^0(M_1) - H_f^0(M_2H^+). \tag{2.25}$$

Here, two cases can arise. In case of an exothermic reaction ($\Delta H_r < 0$), we can just add the reaction and set $\gamma = 0$. In case of an endothermic reaction ($\Delta H_r > 0$), the reaction is only added when $\Delta H_r/k_b$ is smaller than a predetermined barrier. In cases where ΔH_r is small enough, γ is set to $\Delta H_r/k_b$, and the reaction is added anyway. In our standard case, we exclude endothermic reactions (i.e., we set the barrier to zero). In the appendix we investigate the impact of such endothermic reactions by using a barrier value of 5000 K.

Charge exchange reactions - Molecules. For charge exchange reaction, we assume two types: non-dissociative and dissociative. We followed the same approach as with the proton exchanges, meaning we had to supply the different parameters of the Arrhenius equation. Our approach for γ is the same as with the proton exchange reactions. We calculated the difference of the formation enthalpies dH_f and added it as γ if the reaction was exothermic or below the predetermined barrier. For α and β, we simply assumed the values of 5×10^{-10} and -0.5, respectively.

Charge exchange reactions – Dust. If dust grains were involved in a charge exchange reaction, we adjusted the rate coefficient according to

$$k_{\mathrm{j,ex}}(q) = A \frac{\sqrt{\frac{T}{300K}}}{n_{d,\mathrm{ref}}} \left(\frac{a}{a_{\mathrm{ref}}} \right)^2 . \tag{2.26}$$

Here, A is the first factor in the Arrhenius equation and taken from the results from Leung et al. [1984], who calculated these rates for the reference dust particle density $n_{\mathrm{d,ref}} = 2.64 \times 10^{-12}$ cm^{-3} and reference grain radius $a_{\mathrm{ref}} = 0.1\,\mu$m.

2.1.6 Dust charge moments

In principle, each charge state q of the grains in size bin j could be included in the chemical rate network. However, since micron-sized grains can already collect thousands of elementary charges Stark et al. [2015], Tazaki et al. [2020], this method would mean including a couple thousand species, which is computationally very challenging. In order to avoid this problem, the dust grains and all their charge states are represented by three charge moments, $Z^-_{\mathrm{m},j}$, $Z_{\mathrm{m},j}$, and $Z^+_{\mathrm{m},j}$, in each size bin j.

$$[Z^+_{\mathrm{m},j}] = n_{\mathrm{d},j} \sum_{q=1}^{q_{\max}} (+q)\, f_j(q) \tag{2.27}$$

$$[Z^-_{\mathrm{m},j}] = n_{\mathrm{d},j} \sum_{q=-q_{\max}}^{-1} (-q)\, f_j(q) \tag{2.28}$$

$$[Z_{\mathrm{m},j}] = n_{\mathrm{d},j}\, q_{\max} - [Z^-_{\mathrm{m},j}] - [Z^+_{\mathrm{m},j}] \,, \tag{2.29}$$

Table 2.2: Proton affinities P_A and reaction enthalpies with negatively charged silicate grains ΔH_r of selected molecules M[(1)].

M	MH^+	P_A(M) [eV]	ΔH_r [eV]
C_3H_2	$C_3H_3^+$	-9.587	1.196
NH_3	NH_4^+	-8.904	1.879
SiO	$SiOH^+$	-8.06	0.352
C_4	C_4H^+	-8.032	0.324
CS	HCS^+	-8.00	0.2933
CH_3OH	$CH_3OH_2^+$	-7.82	0.112
H_2CS	H_3CS^+	-7.587	-0.121
H_2CO	H_3CO^+	-7.47	-0.243
HCN	$HCNH^+$	-7.426	-0.282
H_2S	H_3S^+	-7.39	-0.314
H_2O	H_3O^+	-7.173	-0.535
HS	H_2S^+	-6.98	-0.728
C_2H_2	$C_2H_3^+$	-6.59	-1.119
CO	HCO^+	-6.1	-1.608
CH_4	CH_5^+	-5.765	-1.943
N_2	HN_2^+	-5.12	-2.588
H_2	H_3^+	-4.36	-3.345

[(1)]The proton affinities are calculated as $P_A(\mathrm{M}) = H_f^0(\mathrm{MH}^+) - H_f^0(\mathrm{M}) - H_f^0(\mathrm{H}^+)$, where $H_f^0(\mathrm{MH}^+)$, $H_f^0(\mathrm{M})$ and $H_f^0(\mathrm{H}^+)$ are the enthalpies of formation of the protonated molecule MH^+, the neutral molecule M, and the proton, outside any electric fields, respectively (see App. A.3). The last column is the reaction enthalpy for a dissociative reaction of a protonated molecule with a negative dust grain $\mathrm{Z}^- + \mathrm{MH}^+ \rightarrow \mathrm{Z} + \mathrm{M} + \mathrm{H}$ (see App. A.3). The dashed line marks the threshold for reactions being considered in the code. The heat of formation data H_f^0 are from Millar et al. [1997] and Linstrom and Mallard [2022].

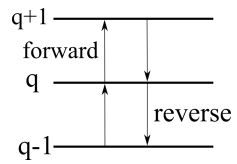

Figure 2.1: Sketch of the linear chain of reactions that populate and depopulate the charge states q. A forward reaction adds a positive charge, a reverse reaction adds a negative charge.

where $q_{\max}$ is the maximum number of elementary charges on the dust grains, both positive and negative, and $n_{\mathrm{d},j}$ is the dust number density of bin j. The moments $Z^{+}_{\mathrm{m},j}$ and $Z^{-}_{\mathrm{m},j}$ express the total number of positive and negative charges on the dust grains in size bin j per volume, respectively. The neutral moment $Z_{\mathrm{m},j}$ is defined in such a way that it becomes zero when all grains have a maximum charge, $q_{\max}$ or $-q_{\max}$, and stays positive for any other charge distribution function $f_j(q)$. The charge distribution function was normalized to one (i.e., $\sum f_j(q) = 1$). According to Eq. (2.29), we can identify a constant quantity,

$$\epsilon_{Z_j} = \frac{q_{\max}\, n_{\mathrm{d},j}}{n_{\langle \mathrm{H} \rangle}} = \frac{[Z^{+}_{\mathrm{m,j}}] + [Z_{\mathrm{m,j}}] + [Z^{-}_{\mathrm{m,j}}]}{n_{\langle \mathrm{H} \rangle}} \ , \tag{2.30}$$

which we used in ProDiMo to define a quasi-element abundance for the dust grains in size bin j. Here, $n_{\langle \mathrm{H} \rangle}$ refers to the total number density of hydrogen nuclei. The mean charge of the grains in size bin j is

$$\langle q_j \rangle \ = \ \sum_{-q_{\max}}^{-1} q\, f_j(q) + \sum_{1}^{q_{\max}} q\, f_j(q) \ = \ \frac{[Z^{+}_{\mathrm{m},j}] - [Z^{-}_{\mathrm{m},j}]}{n_{\mathrm{d},j}}. \tag{2.31}$$

2.1.7 Solving for the charge distribution function

To determine the discrete charge distribution function $f_j(q)$ for all charge states q in every size bin j, we employed a method called linear chains of reactions. We note that we assumed the charge distribution function to be in a steady state. The general idea is that in our model, the charge states q of a grain can only change by one increment, either forward to $q + 1$ or the reverse to $q - 1$. This is illustrated in Fig. 2.1.

The processes that add a charge, $q \to q + 1$, are photoionization (called

photoejection for neutral grains and photodetachment for negative grains) and charge exchange between a dust grain and a molecular cation. The forward rates $[1/s]$ were calculated in the following way:

$$\text{forward}_j(q) \;=\; k_{j,\text{ph}}(q) \;+\; \sum_{\text{cations } M} n_M \, k^M_{j,\text{ex}}(q) \;. \tag{2.32}$$

Here, n_M is the volume density of the molecule M that interacts in a charge exchange reaction with the dust grain Z.

Processes that decrease the charge, $q{+}1 \rightarrow q$, include the recombination with electrons and charge exchange reactions with molecular anions. The reverse rates were calculated as

$$\text{reverse}_j(q) \;=\; n_e \, k_{j,\text{e}}(q) \;+\; \sum_{\text{anions } M} n_M \, k^M_{j,\text{ex}}(q) \;. \tag{2.33}$$

After determining the processes of the forward and reverse rates, the charge distribution function $f_j(q)$ could be determined, separately in each size bin, in a step-down approach. We set $f_j(q_{\max}) = 1$ and performed a sequence of steps where we calculated $f_j(q)$ from $f_j(q{+}1)$ until $q = -q_{\max}$ was reached. During each step, we used

$$f_j(q) \;=\; f_j(q{+}1) \, \frac{\text{reverse}_j(q{+}1)}{\text{forward}_j(q)} \;. \tag{2.34}$$

Eventually, we calculated the normalization constant as

$$f_{j,\text{norm}} = \sum_{-q_{\max}}^{q_{\max}} f_j(q) \tag{2.35}$$

and normalized it as $f_j(q) \rightarrow f_j(q)/f_{j,\text{norm}}$.

The results only depend on the UV to optical photon fluxes, the electron density n_e, and the molecular ion densities M. In Fig. 2.2, we show the resulting $f_j(q)$ for six dust size bins at two positions in the disk. The left side of the figure shows a point in the midplane at $r = 0.1\,\text{au}$ and $z = 0$, and in the right side, a point in the upper areas of the disk also with $r = 0.1$ au but with $z = 0.29$ au is shown.

In the midplane, all grains charge up negatively because there are no UV-photons here, and the rate coefficients for electron attachment are larger than

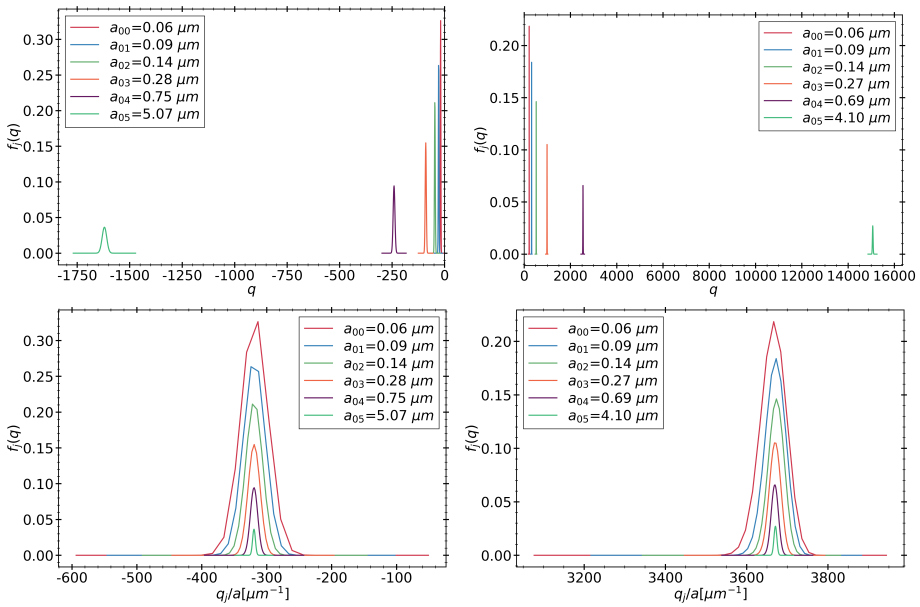

Figure 2.2: Overview of the charge distribution function $f_j(q)$. The two upper panels show the charge distribution function in relation to the charge held by each dust grain bin q. The lower panels also show the charge distribution function but in relation to total charge per dust grain bin size Q/a. The two left panels show the result at $r = 0.1$ au and in the midplane at $z/r = 0$ for each of the six different bins. The two right panels show the results also at $r = 0.1$ but higher up in the disk, at $z/r = 0.3$ Additionally, we show the size of each bin represented by a.

the rate coefficients for charge exchange with molecular ions. In addition, grains charge up negatively because free electrons have a higher mean thermal speed than molecular ions, that is, $\sqrt{\frac{8k_bT}{\pi m_e}} \gg \sqrt{\frac{8k_bT}{\pi m_M}}$. The lower part of the figure shows that the resulting equilibrium charge scales about linear with grain size because it is the electric potential q/a that enters into the rate coefficients. For example, all grains continue to charge up negatively until the rate for electron attachment, with decreases exponentially with q/a, balances the rates for charge exchange with molecular ions, which also depend on q/a. As a result, we get similar q/a values for all grain sizes. This behavior can also be seen and has been discussed in Okuzumi [2009]. There, the authors showed that the shape of the charge distribution function is approximately Gaussian, with its width scaling with the square root of the grain size (compare to our Fig. 2.2). An overview of the behavior of the charge distribution function for the whole simulation, instead of examples at single points in the simulation (as seen in Fig 2.2), can be seen in Fig 2.3.

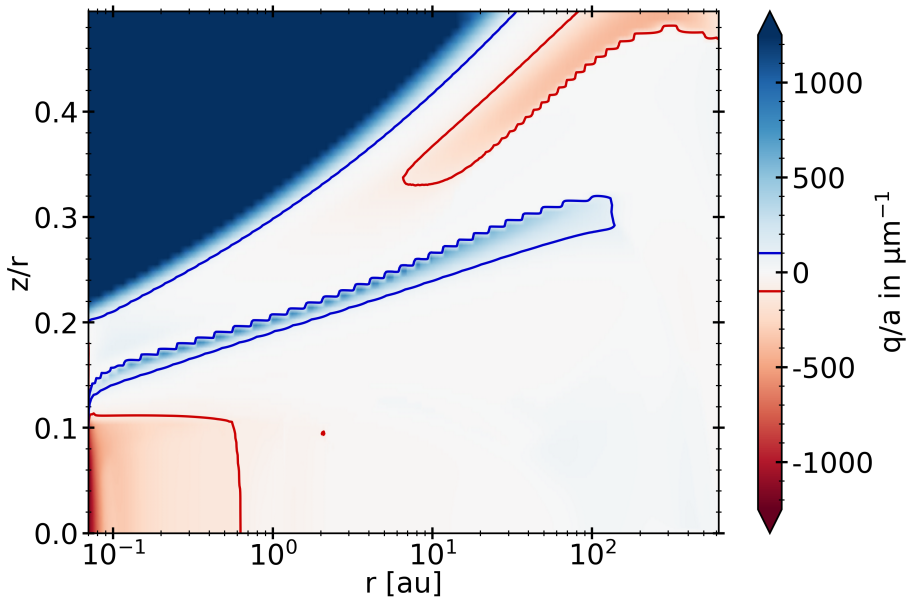

Figure 2.3: Illustration of how the charge per dust grain radius (q/a) [μm^{-1}] changes within the whole disk. For large areas of the disk, the dust is mostly neutral. In the upper areas that are largely affected by photodissociation, we find that dust charges very positively ($\geq$ 100, blue contour lines). In the areas of the midplane closest to the star, we find that the dust charges very negatively ($\leq$ -100, red contour lines).

2.1.8 Effective rates in the chemical rate network

In order to solve the chemical network with the dust charge moments as species, as introduced in Sect. 2.1.6, we needed to derive the effective rate coefficients for the moments. We only demonstrate the derivations for the most relevant processes here. For a full description of all reactions that concern dust grains and their moment representation, we refer to Appendix C of Thi et al. [2019]. For photoejection and photodetachment,

$$Z_{\mathrm{m},j} + h\nu \;\rightarrow\; Z^{+}_{\mathrm{m},j} + e^{-} \tag{2.36}$$

$$Z^{-}_{\mathrm{m},j} + h\nu \;\rightarrow\; Z_{\mathrm{m},j} + e^{-}, \tag{2.37}$$

we have

$$\begin{aligned}
\frac{d[Z^{+}_{\mathrm{m},j}]}{dt} &= k_{\mathrm{m},j,\mathrm{ph}}\,[Z_{\mathrm{m},j}] \;=\; n_{\mathrm{d},j} \sum_{0}^{q_{\max}-1} k_{j,\mathrm{ph}}(q)\, f_j(q) \\
\frac{d[Z_{\mathrm{m},j}]}{dt} &= k^{-}_{\mathrm{m},j,\mathrm{ph}}\,[Z^{-}_{\mathrm{m},j}] \;=\; n_{\mathrm{d},j} \sum_{-q_{\max}}^{1} k_{j,\mathrm{ph}}(q)\, f_j(q).
\end{aligned}$$

We note that these effective rates represent all photoreactions from charge state (q) to charge state $(q+1)$, not just for the neutral and negatively charged grains. To gain the effective rate coefficient, we divided by $[Z_{\mathrm{m},j}]$ and $[Z^{-}_{\mathrm{m},j}]$, respectively:

$$k_{\mathrm{m},j,\mathrm{ph}} = \frac{n_{\mathrm{d},j}}{[Z_{\mathrm{m},j}]} \sum_{0}^{q_{\max}-1} k_{j,\mathrm{ph}}(q)\, f_j(q) \tag{2.38}$$

$$k^{-}_{\mathrm{m},j,\mathrm{ph}} = \frac{n_{\mathrm{d},j}}{[Z^{-}_{\mathrm{m},j}]} \sum_{-q_{\max}}^{-1} k_{j,\mathrm{ph}}(q)\, f_j(q). \tag{2.39}$$

In the code, once $f_j(q)$ has been determined as explained in Sect. 2.1.7, we computed $[Z^{+}_{\mathrm{m},j}]$, $[Z_{\mathrm{m},j}]$, and $[Z^{-}_{\mathrm{m},j}]$ according to Eqs. (2.27) to (2.29) and then determined the effective photo rates from $f_j(q)$ by Eqs. (2.38) and (2.39). The rate coefficients are hence fully determined by the discrete charge distribution functions $f_j(q)$.

For the electron attachment, two new rate coefficients had to be derived.

The derivation is analogous to the photo processes, but one has to consider the different charge states of the grains:

$$Z_{\mathrm{m},j} + e^- \rightarrow Z^-_{\mathrm{m},j} \tag{2.40}$$
$$Z^+_{\mathrm{m},j} + e^- \rightarrow Z_{\mathrm{m},j}. \tag{2.41}$$

As the positively charged grains enhance the electron attachment, we needed to describe their behavior with the rate coefficient $k^+_{\mathrm{m,j,e}}$. Neutral grains do not show this kind of enhancement; therefore, we defined another rate coefficient $k_{\mathrm{m,j,e}}$. We also included the contribution of negatively charged grains to the rate for the neutral grains, even though their contribution to the overall rate coefficient is low. For positive charged grains and neutral grains, with the added contribution of negatively charged grains, we could define

$$\frac{d[Z^-_{\mathrm{m},j}]}{dt} = k_{\mathrm{m},j,\mathrm{e}}[Z_{\mathrm{m},j}] = n_{\mathrm{d},j}\left(k_{j,\mathrm{e}}(0)f_j(0) + \sum_{-q_{\max}+1}^{-1} k_{j,\mathrm{e}}(q)f_j(q)]\right)$$
$$\frac{d[Z_{\mathrm{m},j}]}{dt} = k^+_{\mathrm{m},j,\mathrm{e}}[Z^+_{\mathrm{m},j}] = n_{\mathrm{d},j}\sum_{1}^{q_{\max}} k_{j,\mathrm{e}}(q)f_j(q).$$

Here, $k_{j,\mathrm{e}}(q)$ are the rate coefficients for the individual charge states defined by Eq. (2.16). The effective rate coefficients for electron attachment are hence

$$k_{\mathrm{m},j,\mathrm{e}} = \frac{n_{\mathrm{d},j}}{[Z_{\mathrm{m},j}]}\left(k_{j,\mathrm{e}}(0)f_j(0) + \sum_{-q_{\max}+1}^{-1} k_{j,\mathrm{e}}(q)f_j(q)\right) \tag{2.42}$$
$$k^+_{\mathrm{m},j,\mathrm{e}} = \frac{n_{\mathrm{d},j}}{[Z^+_{\mathrm{m},j}]}\sum_{1}^{q_{\max}} k_{j,\mathrm{e}}(q)f_j(q). \tag{2.43}$$

The charge exchange reactions between dust grains and molecules also had to be adjusted. We considered the rates for neutral grains and negative grains separately:

$$Z_{\mathrm{m},j} + M^+ \rightarrow Z^+_{\mathrm{m},j} + M \tag{2.44}$$
$$Z^-_{\mathrm{m},j} + M^+ \rightarrow Z_{\mathrm{m},j} + M. \tag{2.45}$$

This resulted in the following charge exchange rates:

$$\frac{d[Z^+_{\mathrm{m},j}]}{dt} = k^M_{\mathrm{m},j,\mathrm{ex}}[Z_{\mathrm{m},j}][M^+] = n_{\mathrm{d},j}[M^+]\sum_{0}^{q_{\max}-1} k^M_{j,\mathrm{ex}}(q)f_j(q) \tag{2.46}$$

$$\frac{d[Z_{\mathrm{m},j}]}{dt} = k^{M,-}_{\mathrm{m},j,\mathrm{ex}}[Z^{-}_{\mathrm{m},j}][M^{+}] = n_{\mathrm{d},j}[M^{+}] \sum_{-q_{\max}}^{-1} k^{M}_{j,\mathrm{ex}}(q) f_j(q), \tag{2.47}$$

from which we derived the rate coefficients for charge exchange with molecule M^+:

$$k^{M}_{\mathrm{m},j,\mathrm{ex}} = \frac{n_{\mathrm{d},j}}{[Z_{\mathrm{m},j}]} \sum_{0}^{q_{\max}-1} k^{M}_{j,\mathrm{ex}}(q) f_j(q) \tag{2.48}$$

$$k^{M,-}_{\mathrm{m},j,\mathrm{ex}} = \frac{n_{\mathrm{d},j}}{[Z^{-}_{\mathrm{m},j}]} \sum_{-q_{\max}}^{-1} k^{M}_{j,\mathrm{ex}}(q) f_j(q) \ . \tag{2.49}$$

With these effective rate coefficients for the dust charge moments, we could either solve our rate network system for the time-independent solution, or we could advance the ordinary system of first-order differential equations (ODE system) in time from an initial vector of particle densities. Appendix A.2 explains how to deal with the problem that arises because $f_j(q)$ depends on the electron and molecular ion densities and the rate coefficients depend on particle densities.

2.1.9 Cosmic ray implementation

As explained in Sect. 2.2, we expected lightning to occur, if at all, in the dense and shielded midplane regions of the disk close to the star, where cosmic rays are the most relevant source for ionization. It was therefore important to use a model for the cosmic ray penetration that is as realistic as possible.

We used the description of cosmic ray attenuation and ionization following Padovani et al. [2009] and as implemented by Rab et al. [2017, 2018]. According to this model, the H_2 cosmic ray ionization rate ζ_{cr} s^{-1} is given by

$$\zeta_{\mathrm{cr}} = \begin{cases} \zeta_{\mathrm{low}} & , \ N_{\langle \mathrm{H} \rangle} < 10^{19}\,\mathrm{cm}^{-2} \\ \dfrac{\zeta_{\mathrm{low}}\,\zeta_{\mathrm{high}}}{\zeta_{\mathrm{high}} \left(\frac{N_{\langle \mathrm{H} \rangle}}{10^{20}\mathrm{cm}^{-2}} \right)^{a} + \zeta_{\mathrm{low}} \left(\exp \frac{\Sigma}{\Sigma_0} - 1 \right)} & , \ \text{otherwise} \end{cases} , \tag{2.50}$$

where $N_{\langle \mathrm{H} \rangle}$ [cm^{-2}] is the vertical hydrogen nuclei column density and $\Sigma \approx (1.4\,\mathrm{amu})\, N_{\langle \mathrm{H} \rangle}$ [$\mathrm{g/cm}^2$] the vertical mass column density. The fitting parameters are represented by ζ_{low}, ζ_{high}, Σ_0, and a. These fitting parameters originate from the fitting of cosmic ray spectra and account for different attenuations at

different column densities. The term ζ_{low} is used to fit the spectra for low column densities smaller than 10^{19} cm^{-2}, where the attenuation can be described as a power law, and $\zeta_{\rm high}$ is used for column densities higher than 10^{19} cm^{-2}, where the attenuation can be described with an exponential term. Additionally, Eq. 2.50 is applied twice in our models (once to account for cosmic rays impacting the disk from above and once to account for cosmic rays impacting the disk from below) by adjusting $N_{\langle \rm H \rangle} = 2N_{\langle \rm H \rangle}(r, 0) - N_{\langle \rm H \rangle}(r, z)$, where $N_{\langle \rm H \rangle}(r)$ is the total vertical hydrogen nuclei column density at point r and $N_{\langle \rm H \rangle}(r, z)$ is the local hydrogen nuclei column density at the point (r, z) for which the cosmic ray ionization rate has to be determined. In our main simulation, we made use of the cosmic ray spectra named Solar Max in Cleeves et al. [2013]. We do not include stellar energetic particles (SEPs) in this work.

2.2 Resulting dust charge and ionization properties

This section summarizes our results concerning the mean charge of the dust grains, how the grain charge distribution function depends on the position in the disk and on dust size, and how the dust charge is linked to the degree of ionization and molecular ions in the gas, with particular emphasis on the midplane regions. We first illustrate our standard case, where we only generated exchange reactions but no new protonation reactions and only considered exothermic reactions. A full discussion can be found in Appendix A.1. These results are used later to discuss whether charge separation and lightning can occur in disks (see Sect. 3).

2.2.1 Electron concentration

Figure 2.6 shows the resulting electron concentration $n_{\rm e}/n_{\langle \rm H \rangle}$ as a function of position (r, z) in our disk model. On the basis of these results, we introduced six different disk regions, A-F (see Fig. 2.6), where the physical and chemical processes leading to ionization and dust charge are qualitatively different in each case.

Table 2.3: Parameters of the ProDiMo disk model used in this paper.

stellar and irradiation parameters		
stellar mass	M_*	$0.7\,M_\odot$
stellar luminosity	L_*	$1\,L_\odot$
eff. temperature	T_*	4000 K
excess UV luminosity $/L_\star$	$f_{\rm UV}$	0.01
UV power law exponent	$p_{\rm UV}$	1.3
X ray luminosity	$L_{\rm Xray}$	$1(+30)\,{\rm erg\,s^{-1}}$
X ray emission temperature	$T_{\rm Xray}$	2(+7) K
interstellar UV field strength	$\chi_{\rm ISM}$	1
fitting parameter for $\zeta_{\rm cr}$	$\zeta_{\rm low}$	$2(-19)\,{\rm s^{-1}}$
fitting parameter for $\zeta_{\rm cr}$	$\zeta_{\rm high}$	$8(-19)\,{\rm s^{-1}}$
fitting parameter for $\zeta_{\rm cr}$	Σ_0	$230\ {\rm cm^{-2}}$
fitting parameter for $\zeta_{\rm cr}$	a	-0.01
disk mass and shape parameters		
disk mass	$M_{\rm disk}$	$0.01\ M_\odot$
inner radius	$R_{\rm in}$	0.07 au
tapering-off radius [(1)]	$R_{\rm tap}$	100 au
column density exponent	ϵ	1.0
reference radius	r_0	100 au
scale height at r_0	H_0	10.0 au
flaring power	β	1.15
dust material and size parameters		
dust to gas ratio	dust to gas	0.01
dust composition	$Mg_{0.7}Fe_{0.3}SiO_3$	60%
	amorph. graphite	15%
	porosity	25%
dust mass density	$\rho_{\rm gr}$	$2.094\ {\rm g/cm^3}$
min. dust radius	$a_{\rm min}$	$0.05\,\mu$m
max. dust radius	$a_{\rm max}$	3 mm
dust size dist. exponent	$a_{\rm pow}$	3.5
no. of dust size dist. points	$N_{\rm size}$	100
dust settling parameter	$\alpha_{\rm settle}$	0.01
dust parameters for the chemistry		
no. of dust size bins	$N_{\rm bin}$	6
dust bin fitting indices	κ, ζ	1.0, 2.0
max. dust charge per radius	$q_{\rm max}/a$	$4000\ \mu{\rm m^{-1}}$
simulation parameters		
Grid points in r-direction	NXX	500
Grid points in z-direction	NZZ	100
chemical heating efficiency	$\gamma^{\rm chem}$	0.2

Notation $a(b)$ means $a \times 10^b$.
[(1)]The outer radius $R_{\rm out} \approx 620$ au was adjusted automatically to obtain a vertical hydrogen nuclei column density of $N_{\langle {\rm H} \rangle}(R_{\rm out}) = 10^{\,20}\,{\rm cm^{-2}}$.

2.2.2 Regions F, E, and D - The plasma regions

Regions D-F in Fig. 2.6 are radiation dominated regions, where the UV and X-ray photons create a large degree of ionization along with positive dust charges. We found that region F is dominated by the ionization of H and H_2, region E is dominated by the ionization of atomic carbon, and region D by the ionization of atomic sulfur. According to the assumed element abundances of H, C, and S in our disk model, the degree of ionization in regions F, E, and D is about 1, 10^{-4}, and 10^{-7}, respectively. The grains charge up positively via photo-effect, $\mathrm{Z} + h\nu \rightarrow \mathrm{Z}^+ + \mathrm{e}^-$, and their charge is balanced by electron recombination, $\mathrm{Z}^+ + \mathrm{e}^- \rightarrow \mathrm{Z}$. The total number of charges on the grains, however, is insignificant in comparison to the number of free electrons and positive ions in the gas phase. Any dynamical displacement of the charged grains would easily be balanced out by slight motions of the free electrons in the gas, making charge separations very unlikely to occur in these plasma regions (see further discussion in Sect. 3).

2.2.3 Region A - The dust dominated region

We define region A as the disk region where the number of negative charges on the dust grains is balanced by the abundance of molecular cations. Free electrons are very rare in this region (degree of ionization $10^{-18} \ldots 10^{-14}$) and unimportant for the charge balance. In our disk model, region A is the area that stretches out from just behind the inner rim to about $r \approx 1$,au and $z/r < 0.1$. The outer boundary coincides with the location where water and ammonia ice emerge (snowline), and the upper boundary is roughly given by a vertical visual extinction of $A_V^{\mathrm{ver}} = 10$, which makes sure that UV photons cannot penetrate into region A.

Figure 2.7 shows that we found $NH_4{}^+$ to be by far the most important molecular cation in region A. The chemical processes that lead to this kind of charge balance in region A are multistaged and illustrated in Fig. 2.8.

Since region A is entirely shielded from UV photons and X-rays, cosmic rays are found to be the only relevant ionization source, in particular

$$\mathrm{H_2} \; + \; \mathrm{CR} \; \rightarrow \; \mathrm{H_2^+} + \mathrm{e}^- \; . \tag{2.51}$$

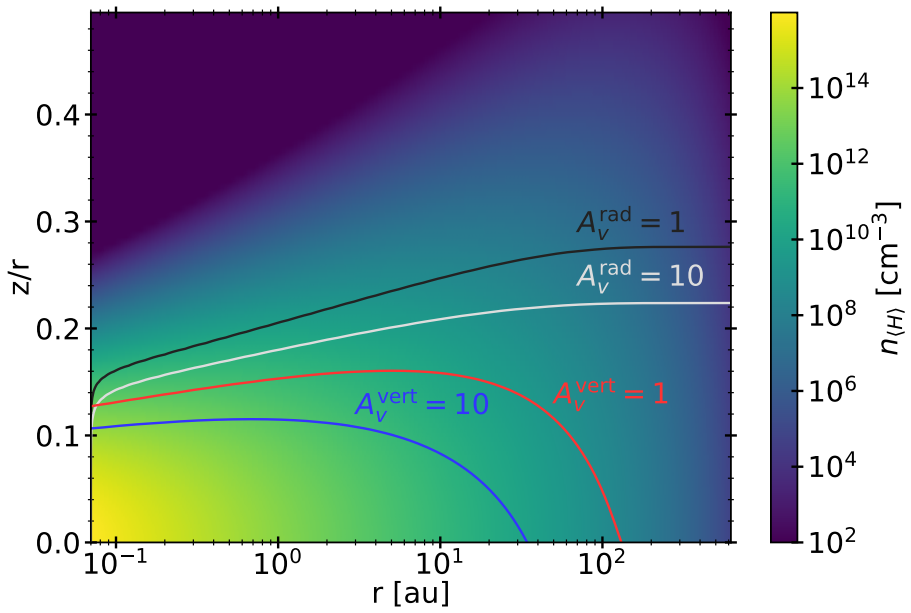

Figure 2.4: Hydrogen nuclei density $n_{\langle \mathrm{H} \rangle}$ [cm^{-3}] as a function of radius r and height over the midplane z in our disk model. The different colored lines represent the visual extinctions in the radial direction (white and black) measured from the star outward and in the vertical direction (red and blue) measured from the surface of the disk toward the midplane.

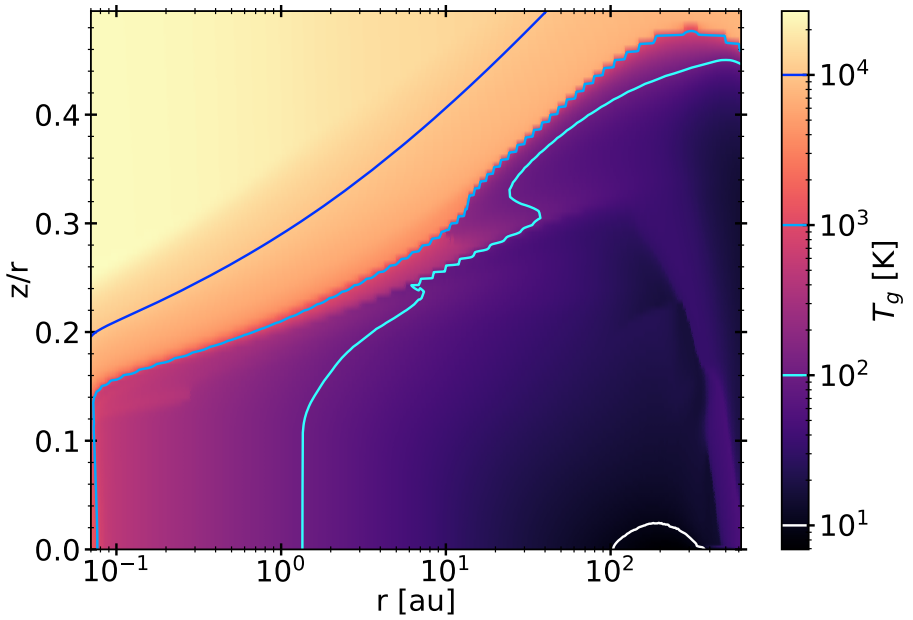

Figure 2.5: Calculated gas temperature structure in the disk model $T_{\rm g}(r, z)$. Colored lines show different orders of magnitude in Kelvin.

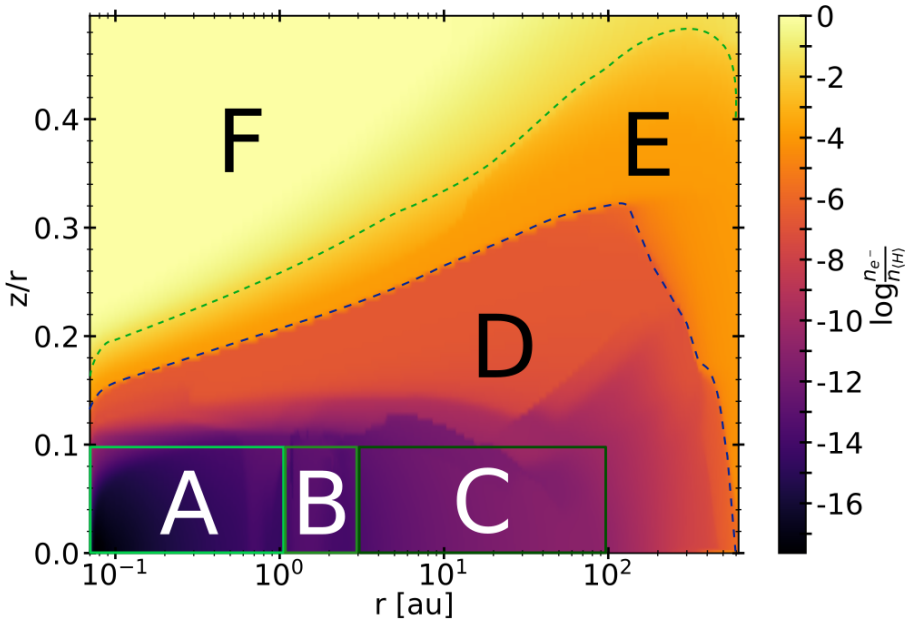

Figure 2.6: Electron concentration $n_{\rm e}/n_{\langle \rm H \rangle}$ as a function of position in the disk. We highlight areas, A-F, where the character of the chemical processes leading to grain charge and gas ionization are different (see text).

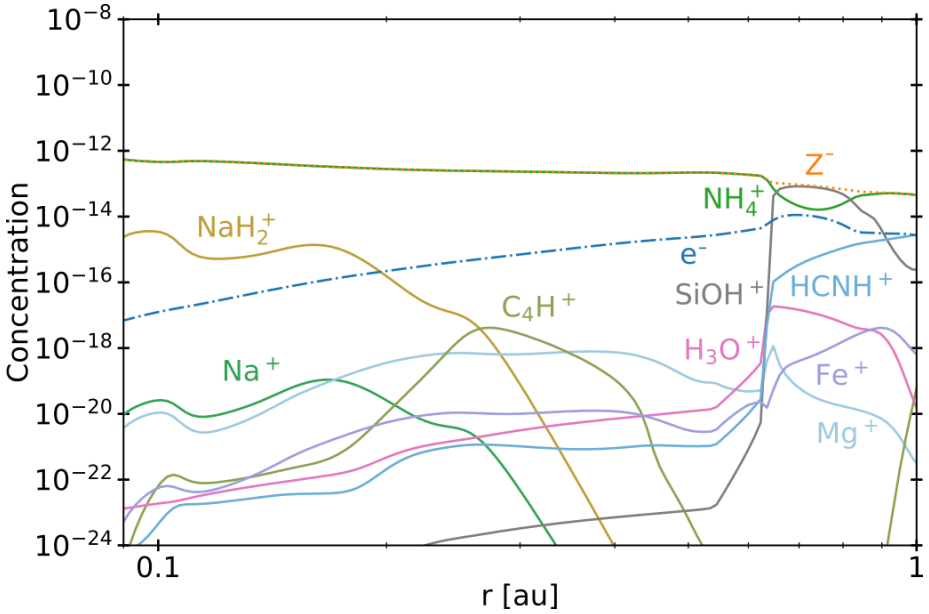

Figure 2.7: Concentrations $n_i/n_{\langle \mathrm{H} \rangle}$ of selected chemical species important for the charge balance in the midplane in region A. The dotted blue line represents the concentration of negative charges on all dust grains $Z^- = \sum_j [Z^-_{\mathrm{m},j}]$. The negative charges have accumulated on grain surfaces, whereas free electrons e^- are less important here.

While the free electrons are quickly picked up by the dust grains via $Z + e^- \rightarrow Z^-$, the $H_2{}^+$ molecules, after fast reactions with H_2, form the molecular cation $H_3{}^+$, which has a relatively low proton affinity (see Table 2.2). Therefore, the surplus protons in $H_3{}^+$ are quickly passed on to other abundant molecules, creating more complex molecular cations, such as H_3O^+, $HCNH^+$, and $NH_4{}^+$. Further proton exchange reactions with abundant neutrals tend to increase the abundances of the protonated molecules, which have the highest proton affinities.

The $NH_4{}^+$ molecule has an extremely high proton affinity of 8.9 eV, which means that it cannot recombine and dissociate on grain surfaces, that is, the reaction $Z^- + NH_4^+ \rightarrow Z + NH_3 + H$ is energetically forbidden. This creates a dead end in which the concentration of $NH_4{}^+$ is enhanced until an equilibrium is established with the dissociative recombination reaction $NH_4^+ + e^- \rightarrow NH_3 + H$ with the extremely rare free electrons.

However, the other protonated molecules below the threshold shown in Table 2.2, denoted by MH^+ in Fig. 2.8, can dissociatively recombine on the surface of the negatively charged dust grains, which creates a charging balance for the dust grains via the following three reactions:

$$Z + e^- \rightarrow Z^- , \tag{2.52}$$

$$Z^- + MH^+ \rightarrow Z + M + H , \tag{2.53}$$

$$Z^- + A^+ \rightarrow Z + A , \tag{2.54}$$

where M is the neutral abundant molecules and MH^+ is their protonated counterparts, in particular H_3O^+ and $HCNH^+$ in region A. There are also some simple charge exchange reactions with atomic ions A^+, such as Mg^+ and Fe^+, whereas the electron affinity of Na^+ of 5.14 eV is too small to detach an electron from a silicate grain on impact (work function 8 eV). We therefore eliminated the reaction $Z^- + Na^+ \rightarrow Z + Na$ from our databases. None of the chemical reaction rates visualized in Fig. 2.8 involve activation barriers, which is important to remember when using this reaction scheme to discuss how the charge balance between Z^-, MH^+, $NH_4{}^+$, and e^- reacts to any changes in density, CRI rate, or temperature. However, reaction (2.52) depends on the number of negative charges already collected by the grains, which is hence a result of the model.

Figure 2.7 shows that $NH_4{}^+$ remains the most abundant molecular cation

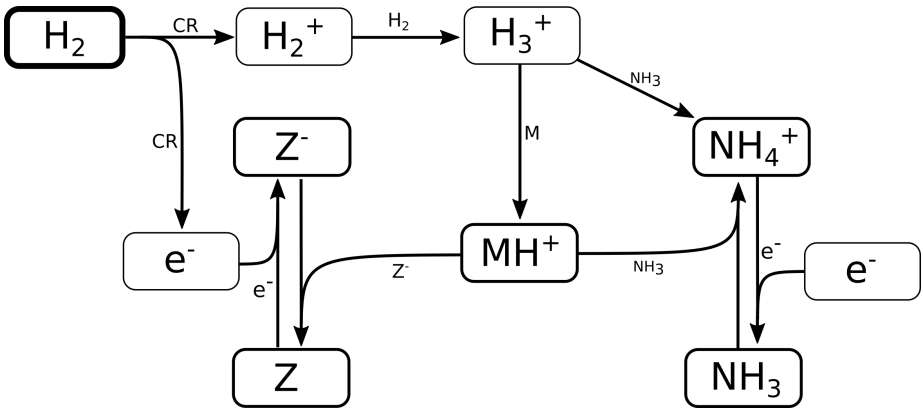

Figure 2.8: Reaction diagram showing how the gas is ionized and the grains obtain negative charges in region A.

up to a radial distance of about 0.7 au, which coincides with the formation of ammonia ice in the midplane of our disk model. At this point, NH_3 is no longer an abundant molecule, and protonated silicon monoxide $SiOH^+$ takes over the role of proton keeper from $NH_4{}^+$. The proton affinity of $SiOH^+$ is 8.1 eV, which means that it also cannot recombine dissociatively on negatively charged dust grain surfaces. Eventually, SiO freezes out as well, at 0.9 au, and we transit into region B.

2.2.4 Region B - The intermediate region

We identify region B as the disk region where the concentrations of (1) negative charges on dust grains, (2) free electrons, and (3) molecular cations are all of the same order, that is, $\approx 10^{-13}$. This happens in a transition region between about 1 au and 3 au in our disk model (see Fig. 2.9). Again, we required $A_V^{\mathrm{ver}} > 10$, ruling out photoionization, which corresponds to $z/r < 0.1$ in our disk model.

Figure 2.10 shows the stepwise freeze-out of oxygen, nitrogen, and carbon into ices with an outward falling temperature, which happens mostly in region B. The freeze-out starts with water ice, then ammonia ice around 1 au, and eventually several hydro-carbon ice phases, such as C_3H_2#, C_2H_5#, and C_2H_4# farther out. At the end of this ice formation zone, at a distance of about 3 au, the midplane is virtually devoid of any molecules other than H_2, He, noble

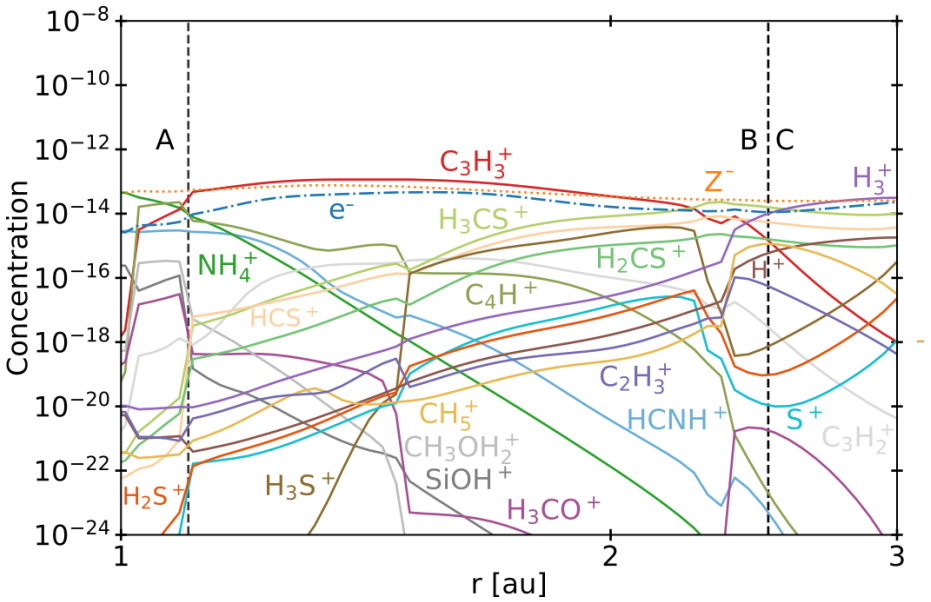

Figure 2.9: Same plot as Fig. 2.7 but for region B. The dashed black lines illustrate the transition between the regions A and B and between B and C, respectively.

gases, and some sulfur molecules, such as H_2S, CS, and H_2CS .

Therefore, the transition region B is carbon rich, with oxygen and nitrogen already being strongly depleted by ice formation. Among the remaining hydrocarbon molecules in region B, we found Cyclopropenylidene C_3H_2 to have the highest proton affinity (see Table 2.2). Consequently, the reaction diagram in Fig. 2.8 would need two slight modifications for to be valid for Region B as well. Firstly, one needs to replace NH_4^+ by $C_3H_3^+$, because $C_3H_3^+$ takes over its role as proton keeper. Secondly, we would replace M with H_2S,CS and H_2CS.

2.2.5 Region C - The metal-poor region

In region C, there are almost no molecules other than H_2 left in the gas phase because nearly all the oxygen, carbon, nitrogen, and sulfur is in the ice. Since the various electron recombination rates scale with n^2 but the cosmic ray ionization rate scales with n, the electron density steadily increases toward larger radii, whereas the concentration of negative charges on dust grains Z^- stays about constant. In fact, we used $n_e = [Z^-]$ to set the boundary between regions B and

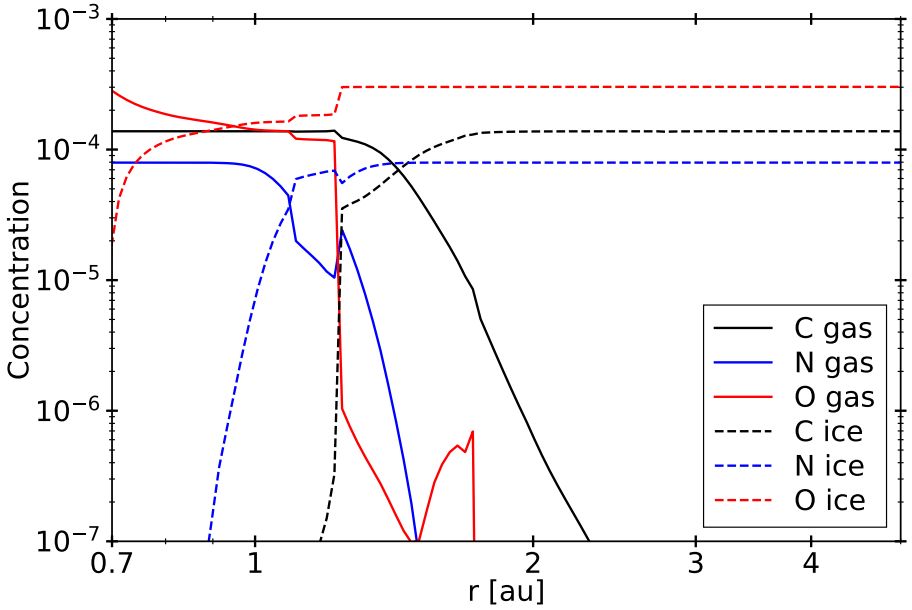

Figure 2.10: Total abundances of oxygen, carbon, and nitrogen in gas molecules and ice phases.

C, which happens at about 3 au in our model.

Consequently, we observed a charge equilibrium between free electrons and H_3^+ in region C, with some traces of H^+, whereas the negatively charged dust grains became increasingly unimportant for the charge equilibrium. Toward the outer edge of region C, the disk becomes vertically transparent again, some interstellar UV and scattered UV starlight reaches the midplane, and we found increasing amounts of ionized sulfur in the gas phase. At a radial distance of about 100 au in our model, H^+ and S^+ become more abundant than H_3^+, and we enter region D.

2.2.6 Dependence of grain charge on physical parameters

In order to investigate the charging behavior of dust grains in more detail, we wanted to investigate the trends seen in Fig. 2.2 further and see how they react to the changing of parameters that influence dust, gas, and electron abundance. In order to do this, we changed five specific parameters and studied how the

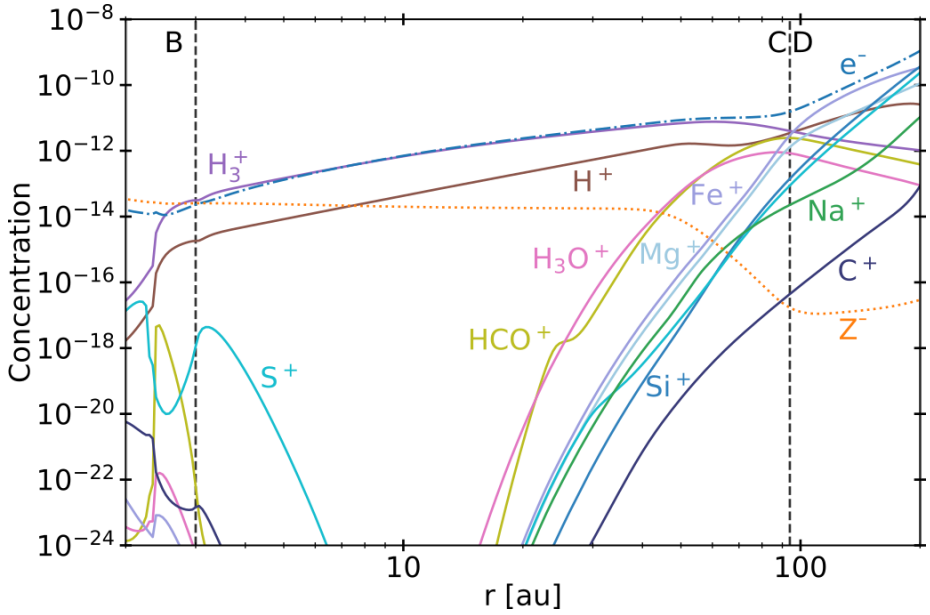

Figure 2.11: Same as Fig. 2.7 but with the species that dominate the charge balance in regions C and D. The vertical dashed lines indicate the transitions between regions B and C and between C and D.

affected species reacted to these changes. We changed the cosmic ray intensity ζ, the minimum dust grain size $a_{\min}$, the total gas density ρ, the dust-to-gas ratio, and the dust temperature $T_{\rm d}$. We did this by changing the parameters compared to our standard case (Tab. 2.3) and solved the chemistry only at the point in our simulation with r=0.1 au and z/r=0 in the midplane. An overview of the parameter space for each changed parameter can be found in Tab. 2.4. We only ever changed one parameter at a given time, and the other unchanged parameters remained equivalent to our standard case.

The main results of this section can be found in Fig. 2.12. Through the plots in the figure, we investigate the abundances of the three species that are the most influential to the charge balance at the investigated point and how the charge distribution function, as seen in the lower parts of Fig. 2.2, compared to q_j/a, changes when varying the different parameters. In order to see changes in the charge distribution functions compared to q_j/a, we created these plots for every dust bin of the different simulations. In order to make a comparison feasible, we took an average of the peaks of these charge distribution functions since Fig.

Table 2.4: Parameters that we varied to test the charging behavior of grains [(1)].

a_{min} [μm]	dust to gas	ζ [s^{-1}]	$M_{\rm disk}$ [$M_\odot$]	$T_{\rm d}$ [K]
0.05	0.0001	10^{-16}	0.0001	100
0.5	0.001	10^{-17}	0.001	200
5	**0.01**	10^{-18}	**0.01**	300
50	0.1	10^{-19}	0.1	**413**
500	1	$\mathbf{5 \times 10^{-20}}$	1	500
		10^{-21}		$\vdots$
		10^{-22}		1800

[(1)]The bold values are the default values of our standard simulation.

2.2 already revealed a very uniform behavior between the different dust bins. In addition, we calculated the standard deviations of the different q_j/a values σ_j. These standard deviations were averaged as well, and this average can be seen in Fig. 2.12 as the gray shaded areas. In the following paragraphs, we describe the different subplots of Fig. 2.12 for each parameter in more detail.

Minimal dust size. For testing the influence of the minimum dust size on the dust charging behavior, we tested five different minimum dust sizes, starting with $a_{\rm min} = 0.05\ \mu m$, which is the default value of our standard simulation, and increasing by a factor of ten at each step until we reached $a_{\rm min} = 500\ \mu m$. The first big trend we observed was the decrease of the abundance of the negatively charged dust grains. This is due to the smaller surface area that a few large dust grains have, compared to many smaller ones, since one of the main contributors to the abundance of negatively charged dust grains is the total surface area. This resulted in lower rate coefficients and therefore less negatively charged dust grains, as they react less with electrons. This also explains the two other trends we observed: an increase in electron abundance and a decrease in NH_4^+ abundance until a saturation is reached at $a_{\rm min} = 50\ \mu m$. As explained before, this is due to the lower amount of dust grains. Dust grains are the main reaction partner of electrons, resulting in the normally high amount of negatively charged dust grains. If fewer dust grains react with electrons, one gets more free electrons.

These free electrons are also part of the main destruction path for the NH_4^+, which explains the decrease of the NH_4^+ molecules. Both the electrons and the NH_4^+ abundances converge toward each other because the dust grain abundance

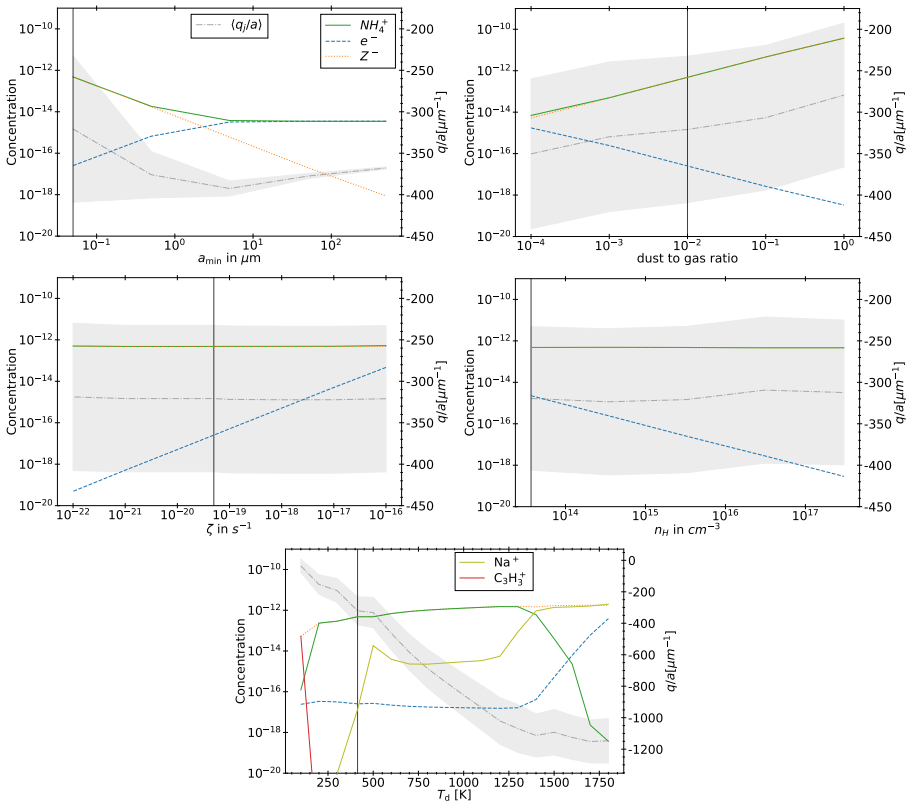

Figure 2.12: Results for the parameter analysis. For all panels, the solid green line represents the abundance of NH_4^+, the dotted orange line represents negatively charged dust grains abundance, and the dashed blue line represents the abundance of the electrons. In addition, the last plot shows the abundance of $C_3H_3^+$ in red and Na^+ in yellow-green. All abundances are represented in units of hydrogen atom abundance, seen on the left Y-axis. The grey dash-dotted line represents the mean of the amount of charge a dust grain carries relative to its size in μm, q_j/a. The shaded area around this line represents the average standard deviation of σ_j. In all plots, we also plotted a vertical black line that represents the conditions of the large simulation from which this set of simulations originates from. **Upper-left panel**: Results for the runs where we modify $a_{\min}$. **Upper-right panel**: Results where we modify the dust-to-gas ratio. **Middle-left panel**: Results where we modify the simulations with a constant cosmic ray ionization rate. **Middle-right panel**: Results where we modify the disk mass in order to increase the total gas density. **Lower panel**: Results where we modify the dust temperature.

becomes fully negligible with a sufficiently high minimum dust grain size.

Dust-to-gas ratio. We tested the influence of different dust-to-gas ratios by simulating five different dust-to-gas ratios, starting with 10^{-4} and again increasing at each step by a factor of ten up to a dust-to-gas ratio of one. The clear trend that can be seen is the decrease of the electron abundance with increasing dust-to-gas ratios. To understand these results, it is central to remember the role dust grains play in the midplane chemistry. Dust grains are the main reaction partner of free electrons. Therefore, increasing the amount of dust grains by increasing the dust-to-gas ratio decreased the amount of electrons. Secondly, as mentioned in the last paragraph, the main destruction pathway of NH_4^+ molecules is via reaction with free electrons. Hence, a reduction of electrons via having more dust grains resulted in an increase of the NH_4^+ molecules as well.

Cosmic rays. To investigate the impact different cosmic ray ionization rates have on our results, we chose to simulate six different cosmic ray ionization rates from $\zeta = 10^{-16}$ to $\zeta = 10^{-22}$. We note that we assumed a constant cosmic ray ionization rate, in contrast to the method we chose for our large simulations. This was done to make it easier to compare results. At the point we investigated, the cosmic ray ionization rate for our standard case is 5×10^{-20}.

The strongest trend one can see is the strong relation between the abundance of the electrons and the cosmic ray ionization rate. The trend is that the lower the cosmic ray ionization rate is, the lower the amount of electrons. This is caused by the fact that the main source of electrons in these highly shielded regions is the ionization of molecular hydrogen via cosmic rays. We also saw no change in the abundance of NH_4^+ and negative charged dust grains. This is the case because the cosmic ray ionization rate also influences how many H_3^+ molecules are available. A decrease in cosmic ray ionization rate also results in less molecular hydrogen ionization. This results in a constant abundance of both negative dust grains and NH_4^+ since there is a decrease of the species that are influential for both the creation and destruction of negatively charged dust grains and NH_4^+. For negatively charged dust grains, the important creation and destruction species are electrons for the creation and protonated molecules for the destruction. For NH_4^+ it is the opposite.

Gas density. To see if changing the gas density changes our result, we simulated different models with a differing disk mass. As the amount of gas in our model cannot be directly increased or decreased, we had to change the disk mass instead, which indirectly increases or decreases the gas density. We simulated five different disk masses, varying from $10^{-4} M_{\odot}$ up to $1 M_{\odot}$. We note, however, that we plotted against gas density and not disk mass. The results are very similar to what we got from the runs where we varied the cosmic ray ionization rate, and this is because increasing the gas density also increases the shielding and hence decreases the amount of cosmic ray ionization and therefore free electrons. Thus, the effects mentioned in the previous section mostly hold true for this part as well.

Dust temperature. We further wanted to investigate how changing the dust temperature could influence the charging behavior of the grains. Thus, we changed the dust temperature from 100 K to 1800 K in steps of 100 K. We note that we also changed the gas temperature at the investigated spot to be equal to the dust temperature at the beginning. The findings can be summarized into four different parts.

At the very first point at 100 K, we observed one clear deviation from the standard picture in the concentration of the NH_4^+ molecules. The molecules are less abundant by two orders of magnitude compared to the normal case. This is due to the fact that at these lower temperatures, we see a similar case to region B in our larger simulations, where nitrogen bearing species are frozen out, therefore reducing nitrogen abundances in the gas. Also similar to region B is that $C_3H_3^+$ is now the most abundant positive species, as carbon has not been frozen out yet and is therefore abundant in the gas phase.

For temperatures between 200 K to 1300 K, the concentrations of the different species resemble the standard case but with two exceptions. First, we found that the ability of the dust grains to gather electrons scales linearly with their temperature. Second, due to the dust grains being able to carry more negative charges, we found a slight increase in the concentrations of the negatively charged dust grains and a decrease in the electron concentration. This also resulted in an increase in the concentration of the NH_4^+ molecules.

From 1400 K to 1800 K, we observed Na^+ become a dominant species. This is due to the creation reactions of Na^+ becoming more efficient. The main

creation reaction that becomes more efficient is the collisional ionization of Na via H_2:

$$Na + H_2 \rightarrow Na^+ + H_2 + e^-. \tag{2.55}$$

This reaction is endothermic in nature, but the barrier of $dH_f/k_b \approx 60000$ is still low enough to be overcome more often at temperatures greater than 1400 K. This results in Na^+ becoming the most abundant positive species after 1400 K, and after 1600 K, it has a similar abundance as the dust grains. Additionally, we observed an increase in the electron concentration, as one of the products of reaction in Eq. 2.55 are electrons. This increase of electrons results in an overall reduction of the NH_4^+ molecules, as the main destruction reaction for NH_4^+ is the recombination with electrons.

3

On the charge separation with a simple turbulence model

This chapter will explain how the charge separation model via turbulence was developed. This chapter will also be taken from my previous publication Balduin et al. [2023], in particular sections 4 and 5.

The text and plots were all created by myself. However, there has been feedback by my coauthor Peter Woitke and help with the turbulence fundamentals by the coauthor Yasuhito Narita.

3.1 Turbulence induced electric fields

In this section, we develop a simple model to estimate the maximum electric field E that can arise when a mixture of negatively charged grains and molecular cations is shaken by turbulence. Figure 3.1 shows a physical sketch of the situa-

tion. We used the Richardson-Kolmogorov approach for turbulence Richardson [1926] Kolmogorov [1941]. Therefore, we assume a superposition of turbulent eddies k with various spatial scales ℓ_k, timescales τ_k, and characteristic velocities $v_k = \ell_k/\tau_k$. In the inertial range

$$v_k \propto (\dot{\epsilon}\, \ell_k)^{1/3} \qquad (\ell_\eta < \ell_k < \ell_L)\ , \tag{3.1}$$

is valid, where $\dot{\epsilon}$ is the energy dissipation rate toward smaller and smaller turbulent scales and ℓ_η and ℓ_L are the smallest (thermalization) and largest (driving) turbulent length scales, respectively. In the co-moving frame of a curved gas flow related to the eddy k, the dust grains are accelerated by the centrifugal force $m\, v_k^2/\ell_k$ until an equilibrium with the frictional force $F_{\rm fric}$ in the gas is established. This problem is well known for constant gravity g (see, e.g., Woitke and Helling [2003].) After an initial acceleration timescale $\tau_{\rm acc}$, the grains of mass m and size a reach a constant drift velocity $\mathring{v}_{\rm dr}$, also known as the final fall speed. We took the results from Woitke and Helling for the case of a subsonic flow and large Knudsen numbers, also known as the Epstein regime. After replacing g by v_k^2/ℓ_k, the results read:

$$\tau_{\rm acc} = \frac{a\,\rho_{\rm m}}{\rho\, v_{\rm th}} \quad , \quad F_{\rm fric} = \frac{m\, v_{\rm dr}}{\tau_{\rm acc}} \quad , \quad \mathring{v}_{\rm dr} = \frac{v_k^2}{\ell_k}\,\tau_{\rm acc}, \tag{3.2}$$

where $\tau_{\rm acc}$ is the acceleration (or stopping) time, $\rho_{\rm m}$ is the dust material density $\approx 2\,{\rm g/cm^3}$, and $v_{\rm th} = \sqrt{8kT/(\pi\bar{m})}$ is the thermal velocity, with $\bar{m}$ being the mean molecular weight of the gas particles.

The drift of the charged grains leads to a charge separation, which causes an electric field. How exactly this field will look is complicated and depends on the geometry and the superposition of the electric currents caused by the drifting grains in the various turbulent eddies. However, we can estimate the maximum electric field that can be generated by a single long-lived eddy by considering the case $(\tau_E, \tau_{\rm acc})$ ¡ t ¡ t_k, where τ_E is the electric field buildup timescale and t_k is the eddy turnover time. We assumed the electric field builds up in a coherent manner, from larger to smaller eddies, but as shown later by Eq. 3.6 and Eq. 3.16, the main contribution comes from smaller eddies.

In this case, after the dust grains become accelerated by the eddies (Fig. 3.1, panel 2: acceleration), an electric field will continue to build up (Fig. 3.1, panel 3: intermediate) until the molecular cations in the gas follow the drifting

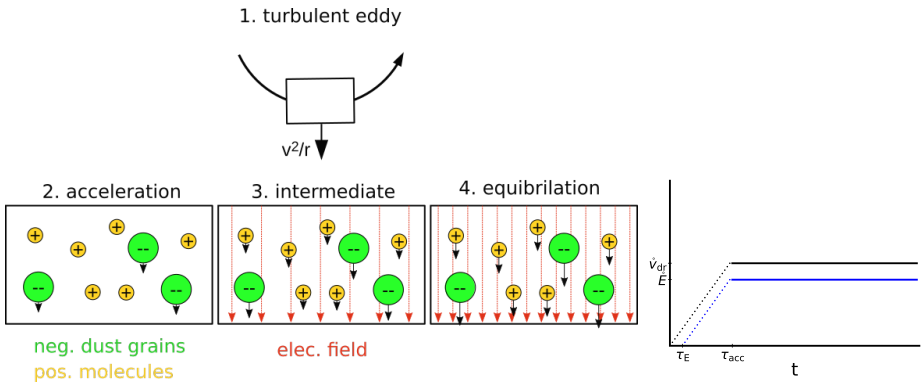

Figure 3.1: Sketch of our electrification model. The left-hand pictures show how the process evolves overtime for the related particles, and the right-hand side shows the time evolution of the drift velocity of the related particles and the electric fields. **Left:** Illustration of the different phases of our electrification model. Firstly, the centrifugal force in a turbulent eddy separates the charges until an electric field builds up, which causes the molecular cations to follow the negatively charged grains. **Right:** Example plot of the length of timescales for acceleration and equibrilation processes shown in the left illustration. The dotted line illustrates that either the dust grains have not reached the drift velocity (black) or that the electric field is not built up yet (blue). The units are arbitrary, as this plot was only made to make the model more understandable.

grains because of their mobility in the E field created by the grains. We call this equilibration (Fig. 3.1, panel 4: equilibration), and it is characterized by a vanishing electric current:

$$j_{\rm el} \;=\; \sum_j \left([Z^+_{{\rm m},j}] - [Z^-_{{\rm m},j}] \right) \mathring{v}_{{\rm dr},j} - n_{\rm e} v_{\rm e} + n_{\rm I} v_{\rm I} \;=\; 0 \;. \tag{3.3}$$

As before, j is an index for the dust size bins; $[Z^+_{{\rm m},j}]$, $[Z^-_{{\rm m},j}]$ are the concentrations of the dust charge moments [charges cm^{-3}] (see Eqs. (2.27) and (2.28)); and $n_{\rm e}$ and $n_{\rm I}$ are the electron and molecular cation densities [charges cm^{-3}].

The drift velocities of the molecular cations and electrons are given by

$$v_{\rm I} = -\mu_{\rm I}\, E \tag{3.4}$$

$$v_{\rm e} = \mu_{\rm e}\, E, \tag{3.5}$$

where $\mu_{\rm I}$ and $\mu_{\rm e}$ are the mobilities of the molecular cations and free electrons, respectively, in units of cm^2 s^{-1} V^{-1}. The E field is measured in V/cm. The

different signs in Eqs. (3.4) and (3.5) are because of the opposite directions of the drift velocities of molecular cations and electrons in a given electric field.

If the turbulent eddy under consideration lives long enough for the drifting grains to build up the maximum, "equilibrated" electric field, it follows from Eq. (3.3) that

$$E = \frac{\sum_j \left([Z^+_{\mathrm{m},j}] - [Z^-_{\mathrm{m},j}] \right) \mathring{v}_{\mathrm{dr},j}}{n_{\mathrm{I}}\,\mu_{\mathrm{I}} + n_{\mathrm{e}}\,\mu_{\mathrm{e}}}. \tag{3.6}$$

From Eq. (3.6) we can immediately see which turbulent flows can potentially produce large E fields. Normal plasmas have $n_{\mathrm{e}} \approx n_{\mathrm{I}} \gg [Z^+], [Z^-]$, in which case we do not expect large turbulence-induced electric fields. Dusty plasmas, like the one we expect in region A in the disk, have $[Z^-] \approx n_{\mathrm{I}} \gg n_{\mathrm{e}} \gg [Z^+]$. The induced electric fields in this case may be large when $\mathring{v}_{\mathrm{dr}}$ is large, μ_{I} is small, and n_{e} is sufficiently small to play no role, in which case n_{I} and $[Z^-] = \sum_j [Z^-_{\mathrm{m},j}]$ cancel, and we find

$$E = \frac{\langle \mathring{v}_{\mathrm{dr}} \rangle}{\mu_{\mathrm{I}}}\ , \tag{3.7}$$

where $\langle \mathring{v}_{\mathrm{dr}} \rangle = \sum_j [Z^-_{\mathrm{m},j}]\, v_{\mathrm{dr},j} \ / \ \sum_j [Z^-_{\mathrm{m},j}]$ is the charge-mean grain drift velocity. There is another case when $[Z^-] \approx [Z^+] \gg n_{\mathrm{I}}, n_{\mathrm{e}}$. In that case, which we call "region X" (not found in our present disk models), large E fields might be produced when many small grains are strongly charged negatively and many large grains are strongly charged positively, or vice versa, such that the nominator in Eq. (3.6) remains large despite charge neutrality in an isolating gas with few charged gas particles. We note that triboelectric charging, which is not included in our current disk models, might be able to turn parts of region A into a region X.

We mention that at this point, there are alternative approaches to how we consider ion and electron mobilities. In Okuzumi and Inutsuka [2015], they present analytic expressions for ion and electron drift velocities in an H_2 gas.

In order to estimate the duration of the equilibration phase in Fig. 3.1, henceforth called the E field buildup timescale τ_{E}, we considered the travel time of the grains

$$\tau_{\mathrm{E}} = \frac{d}{\mathring{v}_{\mathrm{dr}}}, \tag{3.8}$$

where d is the charge separation distance, that is, the distance between the moving grains and the moving molecular ions causing the electric field E. To estimate that distance, we considered the most simple geometry of a parallel

plate capacitor (with equations in SI units):

$$E_{\rm SI} = \frac{Q_{\rm SI}}{\epsilon_0\, A} \tag{3.9}$$

$$Q_{\rm SI} = e\, [Z^-]_{\rm SI}\, A\, d_{\rm SI} \tag{3.10}$$

$$\Rightarrow \quad d_{\rm SI} = \frac{\epsilon_0\, E_{\rm SI}}{e\, [Z^-]_{\rm SI}}\ , \tag{3.11}$$

where ϵ_0 is the electric vacuum permittivity and e is the electron charge in SI units; $E_{\rm SI} = 10^2\, E$ is the maximum electric field in [V/m]; A is a horizontal area [m^2] that cancels; $[Z^-]_{\rm SI} = 10^6\, [Z^-]$ is the concentration of negative charges on dust grains in [m^{-3}]; $d_{\rm SI} = 10^{-2}\, d$ is the charge separation distance in [m]; and $Q_{\rm SI}$ is the total negative charge on the grains in volume $d_{\rm SI} \times A$ in [C]. Equations (3.2), (3.8), and (3.11) provide an estimate for the time required to clear a volume $d \times A$ from dust grains of size a by centrifugal forces in a turbulent eddy k, which results in an overpopulation of negative charges at the lower boundary and missing negative charges at the upper boundary, which together build up the maximum electric field.

Thus, we have three different timescales to consider that may depend on the considered particle size a and the selected turbulent eddy k. In most cases, we found

$$\tau_k \gg \tau_{\rm acc}(a) \gg \tau_{\rm E}(a, k) \tag{3.12}$$

to be valid, that is, the turbulent eddy lives long enough to allow the grains to accelerate quickly and then drift for long enough distances to cause the maximum electric field. If relation (3.12) does not hold, Eq. (3.6) is not valid.

For the ion mobility $\mu_{\rm I}$, we considered the $NH_4{}^+$ cation, as we found this molecule to be the most abundant gas charge carrier in region A. Abedi et al. [2014] presented measurements for the mobility of $NH_4{}^+$ in a N_2 gas at standard pressure and temperature, $P_0 = 760\,$Torr and $T_0 = 273\,$K, which we denote by $\mu^0_{\rm NH_4^+,N_2} = 2.22\,{\rm cm^2 s^{-1} V^{-1}}$. As the most abundant species in the disks is H_2, we needed to adjust this value. This was done by multiplying with the ratio of the reduced masses of N_2 and H_2 with $NH_4{}^+$, denoted with $\bar{m}_{\rm N_2}$ and $\bar{m}_{\rm H_2}$, respectively, and scaling with the gas particle density [see Eq. 4 in Abedi et al., 2014]:

$$\mu_{\rm I} = \mu^0_{\rm NH_4^+,N_2} \left(\frac{\bar{m}_{\rm N_2}}{\bar{m}_{\rm H_2}}\right)^{1/2} \frac{P_0}{P}\frac{T}{T_0}\ . \tag{3.13}$$

The electron mobility $\mu_{\rm e}$ was calculated from the drift velocity measurements for electrons of Ryzko [1965] and calculated as

$$\mu_{e,0} = \frac{v_{\rm dr,e}}{E}, \tag{3.14}$$

with $v_{\rm dr,e}$ measured in dry air to be

$$v_{\rm dr,e} = 256 \times 10^3 \frac{E}{E_0} \frac{P_0}{P} \frac{T}{T_0} [cm/s], \tag{3.15}$$

where P_0 and T_0 are the same as for the ion mobility and $E_0 = 75\,{\rm V\,cm^{-1}}$. This formula results in an electron mobility that is about a factor of 200 larger than the mobility of $NH_4{}^+$. As the original measurements were done in dry air, we would have to adjust our mobility calculations in the same way we did for ion mobility, but due to only minor differences in reduced masses when considering the electron mass, we omitted making a similar correction.

According to our charge separation model, the electric fields that can potentially be caused by turbulence are proportional to the centrifugal accelerations v_k^2/ℓ_k that the turbulent eddies can provide. Following Eq. (3.1), we found

$$\frac{v_k^2}{l_k} \propto l_k^{-1/3}\ , \tag{3.16}$$

that is, the smallest eddies cause the largest centrifugal forces. We therefore considered the Kolmogorov timescale t_η, that is, the turnover timescale of the smallest eddy in the inertial subrange. Following Ormel and Cuzzi [2007], we determined τ_η by

$$\tau_\eta = \frac{\tau_L}{\sqrt{\mathcal{R}e}}, \tag{3.17}$$

where τ_L is the turnover timescale of the largest eddy in our system and $\mathcal{R}e$ is the Reynolds number defined by

$$\mathcal{R}e = \frac{v_L \ell_L}{\nu_{\rm kin}}, \tag{3.18}$$

where v_L is the velocity of the largest eddy, ℓ_L is its size, and $\nu_{\rm kin}$ is the kinematic viscosity. The kinematic viscosity is from Woitke and Helling [2003]. Using their formula for the dynamic viscosity, we got $\nu_{\rm kin} = {}^1\!/_3\, v_{\rm th} \bar{\ell}$. For the size and velocity of the largest eddy, we assumed $\ell_L = \sqrt{\alpha} H_p$ and $v_L = \sqrt{\alpha} c_s$ (see Ormel et al. [2007]), where H_p is the pressure scale height, which is set in our

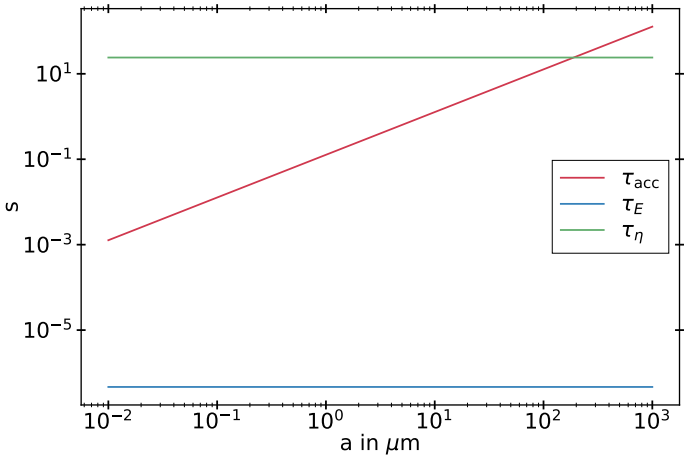

Figure 3.2: Comparison of the different timescales considered in our turbulence implementation.

simulations as

$$H_p(r) = 10\,\mathrm{au}\left(\frac{r}{100\,\mathrm{au}}\right)^{1.15}. \tag{3.19}$$

The resulting size of the smallest turbulent eddy ℓ_η is considerably larger than the gas mean free path $\bar{\ell}$ by about four orders of magnitude, but it is also much smaller in scale height by about eight orders of magnitude.

Since we wanted to maximize the effect of the turbulence, we had to choose the τ_k that maximizes the centrifugal acceleration. Additionally we had to choose a time that allows the electrical fields to develop. Therefore, we followed the principle that we choose the shortest time that is still long enough for the fields to develop. This is illustrated by Fig. 3.2. Following this principle of smallest time that still lets the fields develop, we can see that in most cases we can choose $\tau_k = \tau_\eta$. In cases with larger grains, $a > 10^{-1}$cm, we would choose $\tau_k = \tau_{\mathrm{acc}}$ to ensure the grains have enough time to reach their drift velocity $\mathring{v}_{\mathrm{dr}}$.

With these results, we could then calculate what electric fields would result from the interaction of our dust and gas mixture in a turbulent eddy and answer the question of whether lightning could emerge with this mixture already. Nonetheless, we still had to consider how large these electric fields could be. For lightning to emerge in any medium, the electric fields generated have to be large enough for an electron cascade to occur. We followed the description

and Eq. 56 from Muranushi and Tomiyasu [2009]. With this we were able to define a critical electric field, E_{crit}, that is the electric field at which an electron cascade can occur because the electrons are accelerated enough to ionize the neutral components of the gas:

$$E_{\mathrm{crit}} = \frac{\Delta W}{e\lambda}. \tag{3.20}$$

Here, ΔW is the ionization energy required to ionize the neutral components, e is the coulomb constant, and λ is the mean free path. For ΔW, we took the ionization energy of H_2 with 15.4 eV. To determine, λ we followed Eq. 10 of Woitke and Helling [2003].

3.2 Electric field magnitudes

In this section, we discuss our investigation of the magnitude of the previously discussed turbulence-induced electric fields. We took the data from our simulations that we made for investigating the dust charge behavior from Sect. 2.2.6 to perform this investigation. The resulting electric fields are shown in Fig. 3.3.

Minimal dust size. We found that if one changes the minimal dust size, one first sees an increase in electric field strength due to the increase in dust size and in drift velocity and therefore in electric field strength as well. However, with a minimum dust grain size of more than $0.5\mu m$, a decrease in electric field strength occurs. This is due to the fact that larger dust grains are less abundant in our model. Regarding the way we set up the simulations, only very large dust grains were considered, and therefore the dust abundance drops. According to Eq. 3.6, this of course has a negative impact on the total electric field strength.

Dust-to-gas ratio. For increasing dust-to-gas ratios, we observed a steady increase in electric field strength until a saturation took place at our standard value of 10^{-2}. The reason for the low electric field values at lower dust-to-gas ratios is again the fact that fewer dust grains can contribute positively toward the creation of electric fields.

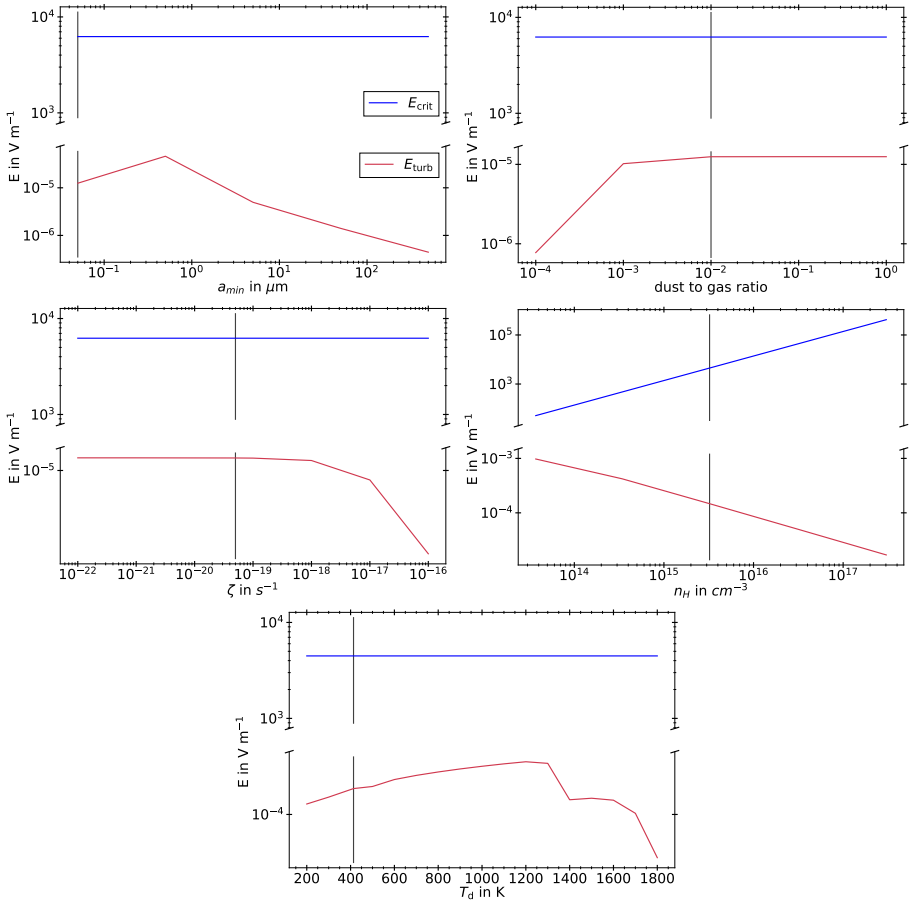

Figure 3.3: The electric fields resulting from turbulence induced eddies for the different parameter variations shown in Sec 2.2.6. The red line represents said electric fields, and the blue line shows the critical electric field as from Eq. 3.20. The solid black lines again represent the conditions from our standard simulation. We note that for the sake of visibility, the y-axis is interrupted, as the differences between the critical fields and the turbulence induced fields are quite large.

Cosmic rays. The influence of cosmic rays on the electric fields is not very surprising given their strong link to electron abundance. High cosmic ray ionization rates result in high electron abundances and therefore low electric fields, due to the attenuating effect electrons have on the buildup of electric fields. The reverse is true for low cosmic ray ionization rates, however, and this effect stagnates at around $10^{-19}[\mathrm{s}^{-1}]$.

Gas density. One could expect that the gas density has a similar effect on the electric fields as the cosmic ray ionization rate, but this does not fully hold. While the general trend is the same, that is, where high gas densities reduce the electron abundance due to the larger shielding, there are more effects that must be mentioned. Compared to the other tests where the critical field is kept constant, we found that the critical field rises with increasing gas densities. This is also the case with higher gas density: the mean free path increases, which increases the required energy for an electron avalanche to occur. We also found that for gas densities lower than our standard value, one can observe an enhancing factor for the electric fields. This is because of the reduced drag on the dust grains in lower gas densities. This in turn increases the drift velocities of the dust grains and can therefore enhance the charge separation and the electric fields.

However, one general trend holds true for all of the studied combination of parameters discussed above, namely, the resulting electric fields are several orders of magnitude smaller than the required critical field. Nonetheless, we can still use this study to state which conditions are best for lightning to emerge. We therefore state that the most likely parameter conditions for lightning to emerge in a protoplanetary disk include having large and abundant dust grains in an area with a low cosmic ray ionization rate and low gas density.

Dust temperature. To calculate the electric field strength for the simulations where we varied the dust temperature, we had to adjust our calculations of the electric field, as the most abundant positive ion for certain temperatures is Na^+ and not NH_4^+. We adjusted Eq. (3.6) to account for the concentration of Na^+, n_{Na^+}, and their mobility μ_{Na^+}:

$$E = \frac{\sum_j \left([Z^+_{\mathrm{m},j}] - [Z^-_{\mathrm{m},j}] \right) v_{\mathrm{dr},j}}{(n_{\mathrm{I}}\,\mu_{\mathrm{I}} + n_{\mathrm{Na}^+}\mu_{\mathrm{Na}^+}) + n_{\mathrm{e}}\,\mu_{\mathrm{e}}}. \tag{3.21}$$

We calculated the mobility of Na^+ in a manner similar to the NH_4^+:

$$\mu_{Na^+} = K_{0,Na^+} \frac{P_0}{P} \frac{T}{T_0}. \tag{3.22}$$

We took 17.5 $[cm^2\ V^{-1}\ s^{-1}]$ for K_{0,Na^+}, according to Loeb [1931], who measured the mobility of Na^+ in H_2. We chose the two normalization factors P_0 and T_0 to be the same as for our NH_4^+ calculations.

With these additional calculations in place, we could analyze the behavior of the electrical field at different temperatures. We note that in our analysis, we omitted the first point at 100 K, as including it would have required taking $C_3H_3^+$ into account with its mobility. We identified three different trends in the electric field curve. First, we identified a steady increase in electric field strength from 200 K up to 1300 K. This can be explained by the steady increase we observed in the concentration of negatively charged dust grains and the NH_4^+ relative to the electron concentration.

From 1400 K to 1600 K, we first observed a drop by nearly a factor of two and then a plateau. This can be explained by the Na^+ ions having become the most relevant positive species. As their mobility is larger by nearly a factor of ten, it is harder for the dust grains to obtain high amounts of separation compared to the case with NH_4^+.

Lastly, we observed a continuous drop in electric field strength until 1800 K. This can be explained by the electron concentration becoming relevant again. As shown in Section 2.2.6, the dominant reaction creating Na^+ also creates free electrons. Due to the very high mobility of the free electrons, they can strongly inhibit the buildup of the electrical field. Their mobility is about two orders of magnitude higher than the ones we found for our positive molecules. Hence, their effect can already be seen when their concentration is still at only about 1% of the negative dust grains and positive molecules.

In conclusion, the picture that presents itself when we modify the dust temperature is more complicated than for our other examples. In isolation, where we would just observe a system of dust grains and one other positive species, one could conclude that higher temperatures show a positive impact on electrical field strength. But as shown in our example, this is an oversimplification, and one should always consider the other effects an increase in temperature can have.

3.3 Discussion of the charge balance in region A under consideration of ion attachment

In this section, we discuss the charge balance in a case where a physical attachment between NH_4^+ and negative dust grains would be possible. Although the dissociative recombination reaction $Z^- + NH_4^+ \rightarrow Z + NH_3 + H$ is energetically forbidden, the NH_4^+ ion could be trapped in the electrostatic potential of a strongly negatively charged grain, either after a collision with its surface or after an inelastic collision with a gas particle close to the surface. This could occur when the electrostatic potential $e^2 \frac{q}{a}$ is much larger than the molecule's thermal energy kT. At a temperature of 100 K, this corresponds to a negative dust charge of $|q|/a \gg 6\,\mu\mathrm{m}^{-1}$. In such cases, the NH_4^+ molecule would be expected to stick to the surface or to stay in close vicinity of the surface.

Such an attachment reaction could be formally written as

$$Z^- + NH_4^+ \leftrightarrow (Z^- – NH_4^+)\ . \tag{3.23}$$

The compound $Z^- – NH_4^+$ would hold both the negative charges of the accumulated electrons and the positive charges of the accumulated molecular ions and would therefore be considerably less negative in the far field due to shielding by the NH_4^+.

We assumed that the overall effects of such a mechanism would not significantly change the charge balance we found in region A but could result in an increase of the non-shielded negative dust grain charge q/a. This would introduce a new destruction path for NH_4^+ with such a reaction, therefore decreasing the amount of NH_4^+ in the gas. This could increase the electron concentration in the charge balance, but the $Z^- – NH_4^+$ compound is less negatively charged than a dust grain Z^-, and it would result in more free electrons attaching to the compound compared to a dust grain. This process would increase the non-shielded grain charge q/a until the shielded negative grain charge becomes similar to the q/a calculated in this paper. In conclusion, such a process would act as a sink of both NH_4^+ and free electrons, while it would increase the non-shielded negative q/a.

However, in order to implement these effects into this work, one would need

more data about the microphysical details of these processes, as such a reaction would not only need to be considered for NH_4^+ but also for every other positive molecule with a proton affinity higher than about 8 eV (Table 2.2), and one would need a kinetic formulation of the back reactions. Therefore, inclusion of this mechanism goes beyond the scope of this paper, but it could be the subject of a follow-up study.

4

Triboelectric charging and its potential implications on the dust grain charge distribution

In this chapter, we will discuss the implementation of triboelectric charging into the dust charge chemistry and discuss the new results one can gather from this implementation.
We will discuss how one can derive a rate and rate coefficient for triboelectric charging in section 4.1.
Then we will discuss how one needs to change the solution method described to account for triboelectric charging in section 4.2.
We will then show some preliminary results of this new solution method and how the dust charge distribution can be affected, in section 4.3.
And lastly, we will discuss the results in section 4.4. In particular we will discuss which parameters could impact the dust charge distribution.
This chapter is entirely new and previously unpublished work.

4.1 Creating a triboelectric rate coefficient

In order to create a rate coefficient for triboelectric charging one has to account for all the factors that could affect how likely the interaction of two dust grains colliding with each other is. We identify three factors which affect how likely such an interaction is, and these three factors will then make up the rate coefficient. These factors are the cross section of both particles σ, the relative velocity between the two interacting particles ΔV, and additionally a factor that accounts for the either attractive or repulsive effect of the coulomb force f_q. The rate coefficient represented by the three factors will take the form of

$$k_t = \sigma \Delta V f_q. \tag{4.1}$$

In order to quantify the rate coefficient properly we have to determine which properties contribute to each factor.

Firstly, one needs to determine the cross section. Similarly to how the cross section is handled in reactions between dust grains and other species, like electrons or molecules, we simply assume the dust grains to be hard spheres. Particular in this case we assume the likelihood of a collision being depend on the surface area of both grains combined. Which results in a cross section where the radii of both dust grains are contributing. This gives us a cross section σ for dust grains of the radii a_1 and a_2 like this

$$\sigma = \pi(a_1 + a_2)^2. \tag{4.2}$$

Compared the other factors contributing to the triboelectric rate coefficient, finding the relative velocity between two dust grains is significantly more challenging. We decided to follow the description of Ormel and Cuzzi [2007], from now on just referred to as OC, where they derived a closed-form expression for the relative velocity between particles in a turbulent medium.

In their publication, they find a general expression for this relative velocity, denoted by $\Delta V_{1,2}$, and then simplify this expression for three distinctive cases. Of those three distinctive cases only the first one will be relevant to this work, hence we will only discuss this one in detail.

The formulation of the relative velocity between the particles will be written

in terms of Stokes numbers of the respective particles St_1 and St_2, which are calculated as

$$St_1 = \frac{t_{\mathrm{s},1}}{t_{\mathrm{L}}} \tag{4.3}$$

$$St_2 = \frac{t_{\mathrm{s},2}}{t_{\mathrm{L}}} \tag{4.4}$$

where $t_{\mathrm{s},1}$, $t_{\mathrm{s},2}$ are the respective stopping times of the particles and follow the first expression in Equation (Eq.3.2) and t_L the life time of the largest eddy, in our case simply assumed to be $1/\Omega_{\mathrm{kep}}$, where Ω_{kep} is the Keplerian rotation frequency. Additionally the terms derived in OC will be dependent on the Reynolds number Re. The Reynolds number will be calculated following Eq. 3.18. Lastly, the terms derived in OC will be dependent on the the gas velocity V_g, equivalent to the turnover velocity of the largest eddy $\sqrt{\alpha}c_s$, where $\sqrt{\alpha}$ is set to 10^{-2} in our simulations and c_s the sound speed. Note that OC refer to particle 1 as the larger particle by default.

The first case that OC consider, considers the particles to be small. In particular this means that their stopping times are much smaller than the Kolmogorov timescale, t_η, $t_1, t_2 < t_\eta = Re^{-1/2}t_L$. In this case $\Delta V_{1,2}$ can be identified as

$$\Delta V_{1,2} = V_g \sqrt{\frac{St_1 - St_2}{St_1 + St_2}\left(\frac{St_1^2}{St_1 + Re^{-1/2}} - \frac{St_2^2}{St_2 + Re^{-1/2}}\right)}. \tag{4.5}$$

In our cases we typically find Stokes numbers of the order from 10^2 for millimeter sized particles down to 10^{-4} for sub micron grains and Reynolds numbers between 10^{-1} up to unity. This results in velocities of the order of tenths of centimeter per second between millimeter and sub-micron particles. Note that one particular case that could arise is that for particles of the same size $V_{1,2}$ would equal zero.

In preliminary studies it was found, that for smaller sub-micron particles in the midplane, these velocities $\Delta V_{1,2}$ can be very similar to the Brownian motion and in many cases even smaller. It seems reasonable however, that the Brownian motion should be a lower limit of how fast particles move. Hence, the velocity between two particles will be now be denoted as ΔV and is a combination of $\Delta V_{1,2}$ and the Brownian velocity v_{brown}

$$\Delta V = \sqrt{\Delta V_{1,2}^2 + v_{\mathrm{brown}}^2} \tag{4.6}$$

with

$$v_{\text{brown}} = \sqrt{\frac{8k_bT_g}{\pi\mu_{\text{red}}}} \tag{4.7}$$

where μ_{red} being the reduced mass of both dust grains involved

$$\mu_{\text{red}} = \frac{m_1 m_2}{m_1 + m_2} \tag{4.8}$$

where the masses m_1 and m_2, are calculated via the raidii of the respective particles and the dust material mass density ρ_{gr}, assuming spherical grains

$$m_i = \rho_{\text{gr}} \frac{4\pi a_i^3}{3} \tag{4.9}$$

Lastly, one needs to determine how to factor in the coulomb repulsion and attraction. Here one can follow the example of the electron attachment rates (Eq. 2.16 and Eq. 2.17). We will determine an interaction probability factor f_q for triboelectric charging, which will modify the rate coefficient to make an interaction where coulomb attraction is the case, more likely, and where coulomb repulsion is the case, less likely.

In order to determine f_q we have to make some slight modification compared to the electron attachment. In particular we have to adjust which energies are compared to each other. For the electron attachment, the velocity that governs how likely a reaction between dust grains and electrons are, is the thermal velocity v_{th} of the electrons. Therefore, the coulomb attraction or repulsion has to be compared to the thermal energy of the electrons, if we want to determine whether an interaction between dust and electrons is more likely or less likely. For two dust grains interacting, the thermal energy is not the relevant factor in determining if the coulomb barrier could be overcome, but the kinetic energy. Therefore a comparison of the coulomb potential and the kinetic energy of the two dust grains is a more sensible comparison. The coulomb potential will be calculated as

$$E_{\text{col}} = \frac{q_1 q_2 e^2}{(a_1 + a_2)} \tag{4.10}$$

where q_1 and q_2 refer to the amounts of charge on the dust grains and e being the fundamental charge. The kinetic energy will be calculated via

$$E_{\text{kin}} = \frac{1}{2}\Delta V^2 \mu_{\text{red}} \tag{4.11}$$

The interaction probability factor, f_q will be formulated in the new rate coefficient for triboelectric charging, by following the formalism of the electron attachment. In case of a repulsion we multiply an additional exponential term to the coefficient to account for having the interaction probability being lower, the higher the repulsion is. In the case of an attractive interaction, we multiply a simple linear term that accounts for the strength of the attractive force

$$f_q = \begin{cases} exp(-\frac{E_{\text{col}}}{E_{\text{kin}}}) & E_{\text{col}} > 0 \\ 1 - (\frac{E_{\text{col}}}{E_{\text{kin}}}) & E_{\text{col}} \leq 0 \end{cases} \tag{4.12}$$

4.2 Adjustments to the solution method to account for triboelectric charging

In order to implement triboelectric charging into the chemistry of ProDiMo several changes to the code are needed. To understand the fundamental changes, that have to be accounted for, we remind the reader about how charges on dust grains were handled in the case that without triboelectric charging.

$$q_i - 1 \leftrightarrows q_i \leftrightarrows q_i + 1 \tag{4.13}$$

Previously, the charge on a grain could only change in single steps, by either +1 or -1, and the changes on a specific bin that represents a certain amount of dust grains, was independent of other bins. Meaning how much the grain charge of the i-th bin, q_i, changes was only dependent on the properties of the i-th bin itself and how the surrounding medium affects it, via radiation, temperature or potentially available reaction partners, such as molecules. In equation 4.13 this is referenced by the arrows having the same color. Including triboelectric charging changes these two fundamentals.

Firstly, more than a single charge can be exchanged. This amount of charge that will be exchanged will be called Δq. Secondly, the grain charges are not independent of each other anymore, as we allow different grains to react with each other now. Their differing properties like size or charge contribute to how likely an interaction/reaction between two different dust grain bins is. Therefore

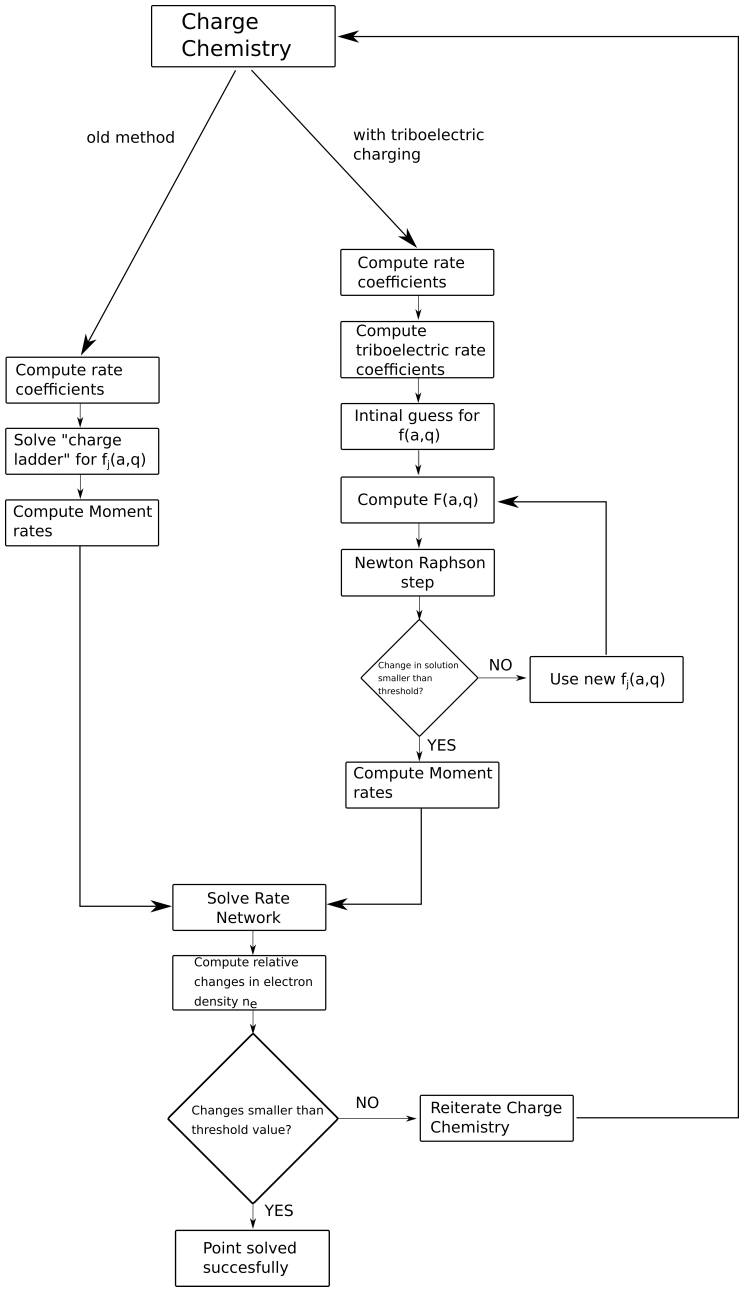

Figure 4.1: A flow chart that describes the way ProDiMo handles its charge chemistry. The previous approach of the charge chemistry, without triboelectric charging , follows the left hand side. The new approach with triboelectric charging follows the right hand side.

the simple picture of Eq. 4.13 will be significantly more complicated now

$$q_i - \Delta q \leftarrow q_i \leftarrow q_i + \Delta q \tag{4.14}$$

$$q_j - \Delta q \rightarrow q_j \rightarrow q_j + \Delta q \tag{4.15}$$

$$q_i - \Delta q \rightarrow q_i \rightarrow q_i + \Delta q \tag{4.16}$$

$$q_j - \Delta q \leftarrow q_j \leftarrow q_j + \Delta q \tag{4.17}$$

We assume here that the smaller grain i will take electrons from the larger grain j. The fact that different reactions are now linked with each other is represented by the different colors of the arrows. Meaning that the backwards reaction represented by the arrow of one color is linked to the forwards reaction of an arrow of the same color.

The new solving approach will be very similar to how the time independent chemistry as a whole is solved in ProDiMo. An overview of how the old and the new solving approach compare can be seen in Fig. 4.1. The chemistry in ProDiMo follows the kinetic equilibrium approach. Shortly speaking, this means that the number densities of all species in the network n_i should not change over a given time frame

$$\frac{dn_i}{dt} = 0 \tag{4.18}$$

For the dust charge distribution $f(a, q)$* we can follow the same approach where one has to find a solution where the charge distribution function should not change in a given time frame

$$\frac{df(a,q)}{dt} = F(a,q) = 0 \tag{4.19}$$

Such a problem can be solved with a Newton-Raphson iteration,

$$\vec{x}_{i+1} = \vec{x}_i - \Delta\vec{x}_i \tag{4.20}$$

where from an initial guess $\vec{x}_0$ one iterates, until the changes in the solution vector $d\vec{x}$ are small compared to a threshold value. This solution vector can be

*Note that this expression of $f(a, q)$ is equivalent to the previous description of the dust grain charge distribution of $f_j(q)$. Since, the distinctive factor between the dust grains is their radius, we decided to write the radius a explicitly into the argument of the function for the sake of clarity.

found by solving the equation

$$DF(a,q)\,\Delta\vec{x}_i = F(a,q) \tag{4.21}$$

with $DF(a,q)$ being the Jacobi matrix

$$DF(a,q)_{i,j} = \frac{\partial F(a_i,q_i)}{\partial x_j} \tag{4.22}$$

In order to construct $F(a,q)$ we have to first discuss how $f(a,q)$ is structured. Since $f(a,q)$ and its time derivative have $F(a,q)$ are vectors we have to find a one dimensional way of accounting for both relevant dimensions radius a and charge states q. The following illustration gives a short explanation of how $f(a,q)$ is structured for an example of three different bins

$$f(a,q) = \begin{pmatrix} a_1,q_{1_{\min}} \\ \vdots \\ a_1,q_{1_{\max}} \\ a_2,q_{2_{\min}} \\ \vdots \\ a_2,q_{2_{\max}} \\ a_3,q_{3_{\min}} \\ \vdots \\ a_3,q_{3_{\max}} \end{pmatrix} \tag{4.23}$$

Here $q_{1_{\min}}$ and $q_{1_{\max}}$ represent the minimal and maximal amounts of charge in the first bin, with the same being true for the other two bins respectively. These boundaries are first estimated, similar to how the old approach sets its boundaries. But, in our studies we found, that this approach will not work all the time, because of what happens within $f(a,q)$ when a reaction occurs (see Fig. 4.2). In the example, we only show newly created charging states within the boundaries of the sub-arrays of $f(a,q)$, but this will not always be the case. There can be cases where Δq will be so large that it would create states outside of array boundaries. Therefore we have to adjust the different bins by hand to

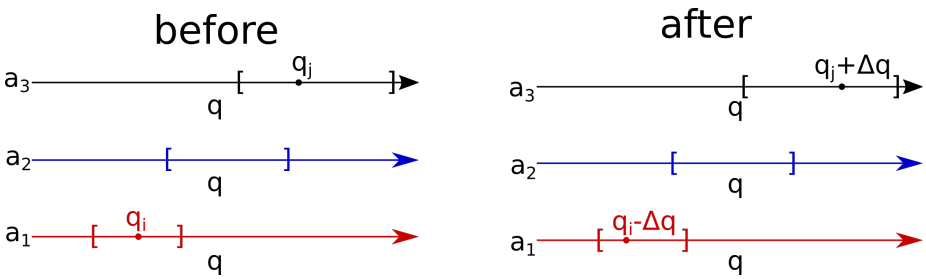

Figure 4.2: This plot illustrates how the dust charge distribution of the different dust grain bins change, when two dust grains bins interact with each other via triboelectric charging. On the left hand side are the distributions of three exemplary dust grain bins. The right hand side illustrates how one would need to adjust the distributions if bin 1 and 3 would interact with each other.

make sure that all potentially new charging states are accounted for. At the current code version, this process is needed for every different simulation point. Typical dimension for $f(a,q)$ at the usual example that we use with 6 bins is about 5000 entries in $f(a,q)$. This results in a dimension for $DF(a,q)$ of 5000 x 5000.

In order to now construct $F(a,q)$ we have to account for the change in charging states of the particles that interact before the collision and after the collision. Before the collision of particles i and j the corresponding change of charging states and how they would be written into $F(a,q)$ would look like this

$$n_i F(a_i, q_i) - = \sum_{a_j} \sum_{q_j} k_t n_i f(a_i, q_i) n_j f(a_j, q_j) \tag{4.24}$$

$$n_j F(a_j, q_j) - = \sum_{a_i} \sum_{q_i} k_t n_i f(a_i, q_i) n_j f(a_j, q_j) \tag{4.25}$$

note here that k_t refers to the rate coefficient as described in Eq. 4.1 and the minus sign before the equal sign, $- =$, indicates that these states are destroyed.

To account for the new states that would be created after a collision entries in $F(a,q)$ would look like this

$$n_i F(a_i, q_i - \Delta q) + = \sum_{a_j > a_i} \sum_{q_j} k_t n_i f(a_i, q_i) n_j f(a_j, q_j) \tag{4.26}$$

$$n_j F(a_j, q_j + \Delta q) += \sum_{a_i} \sum_{q_i} k_t n_i f(a_i, q_i) n_j f(a_j, q_j) \tag{4.27}$$

were the two changes to before the collision are the creation of a state either at $q_i + \Delta q$ or $q_j - \Delta q$, and a plus sign before the equal sign, $+=$, indicating a summation of all new states, as they are being created. In order to construct $DF(a, q)$ we can follow Eq. 4.22 and apply it to equations 4.24 - 4.27 respectively.

4.2.1 Determining the amount of charge transferred in a dust-dust interaction

One question that needs to be discussed when it comes to triboelectric charging is how many charges can be interchanged between the dust grains. As discussed in the introduction (Sec. 1.4.2) there is proof that a large amount of charges can exchanged in a single interaction between two dust grains (see again Jungmann et al. [2021]).

One fact that one regularly finds when triboelectric charging is discussed, is the fact that when two particles interact and exchange charges, they tend to do it in a manner where the workfunctions of the interacting grains equalize each other. In other words, if a grain with a higher workfunction interacts with a grain of a lower workfunction, we would see a transfer of charges in such a manner, that the workfunction of the larger grain gets lowered and the workfunction of the smaller grain increases, to a point where both workfunctions would be on the same level. Implementing such a way of determining the charge exchange is a bit more challenging in our case, due to the fact that in our case, materials with very similar workfunctions would interact with each other. Therefore the amount of charge exchanged would be very low.

However, to simplify our model and to account for a more realistic amount of charges exchanged, we assume in the following that Δq is given by one forth of the charge interval $(q_{\max} - q_{\min})$ of the smaller particle. This method has shown to create charge exchanges in the hundreds and low thousands of charges. Which is an amount that the code seems to be able to handle at this point.

4.2.2 Recalculating the rates for dust charge moments in the chemical network

In order to have this new approach work with the way the charge chemistry is handled in ProDiMo one needs to recalculate the dust grain moments to account for the impact that triboelectric charging can have. Similarly to how it has to be undertaken for non-triboelectric rates and as discussed in Section 2.1.8. Again we only consider rates where the smaller grain gets excess electrons from the larger grain, hence we only consider four types of reactions.

Firstly a neutral-neutral reaction where the smaller grain i gets negative charges from the larger grain j

$$Z_{m,i} + Z_{m,j} \rightarrow Z^{-}_{m,i} + Z^{+}_{m,j} \tag{4.28}$$

a positive-negative reaction, where both grains neutralize

$$Z^{+}_{m,i} + Z^{-}_{m,j} \rightarrow Z_{m,i} + Z_{m,j} \tag{4.29}$$

a positive-neutral reaction, where the positive charge is transferred to the larger grain

$$Z^{+}_{m,i} + Z_{m,j} \rightarrow Z_{m,i} + Z^{+}_{m,j} \tag{4.30}$$

and a neutral-negative reaction where the extra negative charge is transferred from the larger to the smaller grain

$$Z_{m,i} + Z^{-}_{m,j} \rightarrow Z^{-}_{m,i} + Z_{m,j} \tag{4.31}$$

The moment rate coefficients for each respective type of reaction are calculated as $k^{c_i,c_j}_{\mathrm{m,i,j,t}}$, where c_i and c_j represent the respective sings of the charges of the involved dust grains, and saved. Here is, as an example, how the moment rate coefficient for the positive-negative reaction will be calculated

$$k^{+,-}_{\mathrm{m,i,j,t}} = \sum_{q_i>0} \sum_{q_j<0} k_{\mathrm{t,q_i,q_j}} f(a_i, q_i) f(a_j, q_j) \Delta q \tag{4.32}$$

with the first sum representing the fact that only positive states of i are accounted for via $q_i > 0$ and the second sum represents the that only negative states of j are accounted for via $q_j < 0$. Additionally, $k_{\mathrm{t,q_i,q_j}}$ represent the tribo-

electric rate coefficient at the different charge states and $f(a_i, q_i)$ and $f(a_j, q_j)$ are the charge distribution functions of the i-th and j-th bin at the respective charge states.

A final step is then a normalization of the rate coefficient via the relevant moments

$$\frac{k^{+,-}_{\mathrm{m,i,j,t}}}{Z^{+}_{m,i} Z^{-}_{m,j}} \rightarrow k^{+,-}_{\mathrm{m,i,j,t}} \tag{4.33}$$

The other moment rate coefficients can be calculated analogously, but with changes in the boundaries of the sums, depending on the charges of the interacting particles. The normalization also have to adjusted to account for the relevant dust moments

$$\frac{k^{0,0}_{\mathrm{m,i,j,t}}}{Z_{m,i} Z_{m,j}} \rightarrow k^{0,0}_{\mathrm{m,i,j,t}} \tag{4.34}$$

$$\frac{k^{+,0}_{\mathrm{m,i,j,t}}}{Z^{+}_{m,i} Z_{m,j}} \rightarrow k^{+,0}_{\mathrm{m,i,j,t}} \tag{4.35}$$

$$\frac{k^{0,-}_{\mathrm{m,i,j,t}}}{Z_{m,i} Z^{-}_{m,j}} \rightarrow k^{0,-}_{\mathrm{m,i,j,t}} \tag{4.36}$$

4.3 Results

In this section we show preliminary results from the previous explained implementation, explain the change we will see in the dust grain charge distribution and discuss further effects and implications this change might have.

4.3.1 Overcoming the Coulomb Barrier

We started our investigation if triboelectric rates and rate coefficients are relevant for dust grain charging with a first test to see if these rates are relevant in the midplanes of disks. This test entailed to simply calculate the rate coefficients for the triboelectric charging and compare it to the most dominant charging process in midplane regions which is electron attachment. For these calculations the main simulation described it 2.3 will be used. Note that the rates were at first calculated without any coulomb interaction, as some previous tests have given the impression that the velocities we find in the midplane are

not high enough for particles to interact with each other at a high enough probability for triboelectric charging to be relevant. So in order to isolate velocity as a parameter, the coulomb interaction was neglected for now.

To see whether triboelectric rates can be relevant compared to the electron attachment, we plot the triboelectric rates of the largest Z_{05} and smallest particles Z_{00} interacting with each other, with $f_q = 1$ to neglect any contributions from the coulomb interaction, and compare it to the respective electron attachment rates of Z_{05} and Z_{00} (See. Fig. 4.3). We find that triboelectric charging should be a relevant mechanism in region A. However one also sees that this will only be true for areas closer towards the star as there the electron density is still lower due to the higher shielding. In areas above 0.6 au electron attachment dominates due the larger electron density and the fact that the electron velocity, in general, tends to be higher than the velocity of the dust grains, which results in a higher rate coefficients. It could therefore be concluded that triboelectric charging should play a significant role in the charge distribution of dust grains in the inwards regions of the midplane.

Unfortunately, if one accounts for the coulomb interaction, the triboelectric rates between the largest and the smallest dust grains in the inner areas of the midplane of our previous simulation drop significantly. This has to do with the simple fact, that at micron to sub-micron dust grain sizes, the kinetic energy of the particles would not be sufficient to overcome the coulomb barrier. A comparison between the kinetic energy and the coulomb potential can be seen in the upper plot of Fig. 4.4. One way of overcoming the barrier would be to test larger grains radii, as the radius scales the mass of the dust grains (Eq.4.9) and the mass of the dust grains scales the kinetic energy. This can be done in our simulations by adjusting the power law indices as discussed in section 2.1.3. In a new simulation the power law index was adjusted to 3, compared to the older simulation where it was set to 2. This results in dust grain sizes reaching from the micron range for the smallest bin to several millimeter in the largest bin. If one compares the energies for such an interaction again, one finds that now the kinetic energy should be more than sufficient to overcome the coulomb barrier in most areas of Region A (see Fig. 4.4 lower plot). Hence, we can conclude that in order to test the impact of triboelectric charging, sufficiently large dust grains have to be considered.

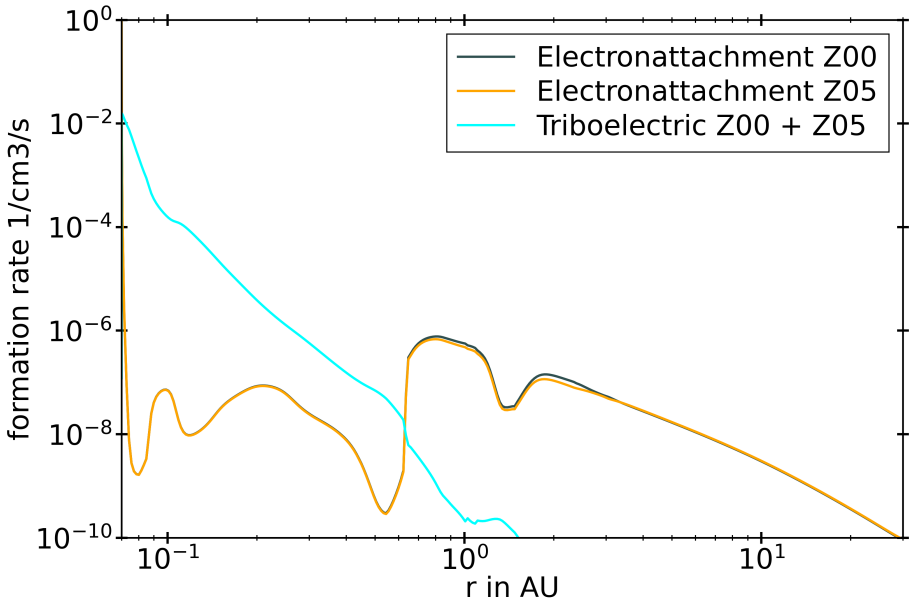

Figure 4.3: Comparison between the electron attachment rates of the smallest dust grain bin Z_{00} (dark blue line) and largest grains Z_{05} (orange line) and the triboelectric rate between the two particles without their coulomb interaction account for (sky blue line).

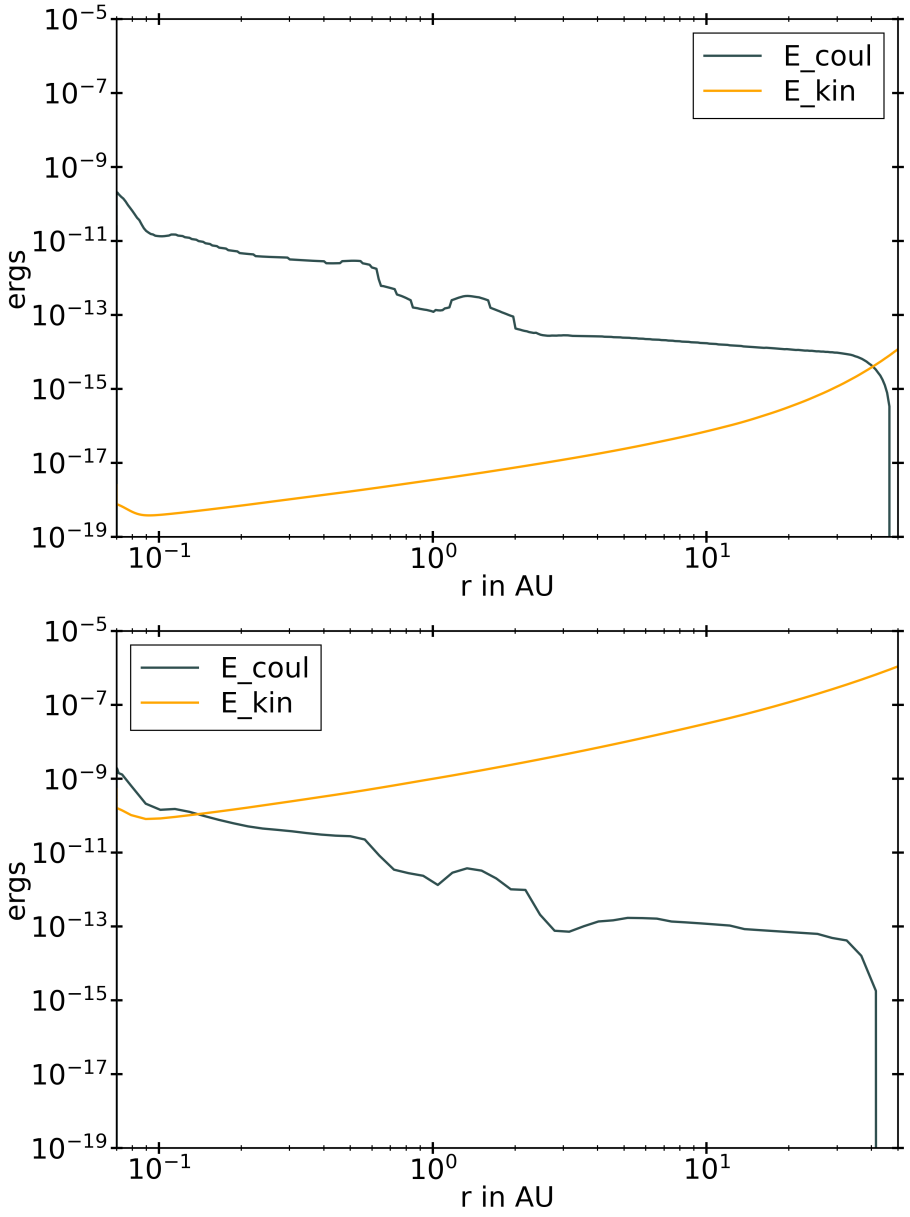

Figure 4.4: Comparison of the kinetic energy of the interaction of the smallest and largest grain bin in the simulation and the energy of the coulomb interaction. The upper plot is a comparison of the simulation with smaller, sub-micron to micro dust grains, at a power law fit index of 2. The lower plot is a comparison with larger grains up to millimeter sizes, at a power law fit index of 3

4.3.2 Impact on the dust charge distribution

We will now use our implementation of triboelectric charging, to see the impact on the dust grain charge distribution in detail. Due to the computational effort, this will first be done at a single point of the simulation. Due to the results of the previous tests, a point closer to the star was chosen, in order to maximize potential effects of triboelectric charging. The relevant parameters of this point are shown in table 4.1.

Note that for the power law fitting index ζ_{fit} 2.3 was used, and not as one might expect 3 from the previous test. This is simply done for the sake of simplicity. Increasing the power law index and therefore the size of the dust grains, also increases the amounts of potential charging states that have to be accounted for. For a power law index of 2.3 the dimension of the systems of ordinary differential equations that needs to be solved is in the realm of several thousands. Increasing this by just one decimal point to 2.4 leads to nearly an order of magnitude increase to dimensions in the tens of thousand. To solve such a large system, and potentially even larger systems, was not feasible at this point. As will be seen, at 2.3, the effects of triboelectric charging can already be seen to have a very significant impact, but its is noted that for a full overview of the effect different dust sizes should be probed and its potential effect will be discussed in the discussion of this chapter Sec. 4.4.1.
The results of this point simulation can be found in Figures 4.6 and 4.7. For comparison on how the dust charge distribution would look without triboelectric charging at the same point with the same parameters refer to Figure 4.5.

There are several interesting changes in the dust charge distribution when triboelectric charging is considered. Firstly, one might notice that the largest bin has considerably less amounts of charge. Which can be explained, by the reaction between the largest grain and smaller grains. A reaction of the type

$$Z_{05}^{-} + Z_{<1\mu m} \rightarrow Z_{05} + Z_{<1\mu m}^{-} \tag{4.37}$$

reveals itself to be the creation reaction with the largest rate for all dust grains smaller then 1 micron, represented by $Z_{<1\mu m}$, and the destruction reaction with largest rate for the largest grains Z_{05}.

One might now ask, why is the triboelectric rate between the largest grains

Table 4.1: Parameters for the point simulations used to test the triboelectric charging implementation

parameter	value and unit
distance from the host star r	0.07 [au]
height over the midplane z	0 [au]
gas temperature T_g	563.34 [K]
dust temperature T_d	563.34 [K]
gas density ρ	2.1×10^{-8} [g cm^{-3}]
dust to gas ratio	0.01
cosmic ray ionization rate ζ_{CR}	1.8×10^{-20}[s^{-1}]
power law index ζ_{fit}	2.3

and grains larger than 1 micron not the largest creation rate for grains larger than 1 micron. This can be explained by electron attachment. For grains larger than 1 micron, the abundances become smaller than the electron abundance. Hence, for these grains electron attachment is the dominating rate. Note, however triboelectric charging is still a relevant contributor.

These findings reveal that including triboelectric charging results in a changed pathway of how the charge balance establishes itself in the midplane, compared to our previous results. This new pathway is shown in Fig. 4.8. One can think of the new pathway of the charge balance establishing itself, similar to the previous way, but with an extra intermediate step included. Instead of all dust grains reaction with electrons, it now tends to be that only the largest one are reacting with the free electrons. They then give these negative charges to the smaller grains via triboelectric reactions with the smaller grains. What remains true compared to the previous results is that smaller grains still get neutralized by reactions with protonated molecules.

Looking deeper into the results, one finds that the largest change in average charge $\langle q \rangle$ and average charge per dust bin size $\langle q/a_i \rangle$ can be seen for the second smallest bin Z_{01} (see Tab. 4.2 first two tables). This is the case, because of the reaction between the largest grains Z_{05} and the second smallest Z_{01} dust grain bin having the highest rate of all triboelectric rates. From this the question

arises, why is the second smallest grain the one with the highest rate coefficient. One might expect that the rate between smallest and largest to be the highest, as the relative velocity between those two bins are the highest and because the smaller grains are the most abundant. But whilst this reaction is still very relevant for the smallest grains, it is not higher than the rate between the second smallest and largest because of the coulomb barrier. At the current constellation of bin sizes, for the second smallest bin the coulomb barrier can be overcome easier compared to the smallest bin. We show the relevant kinetic energies, coulomb barriers and ratios of the two in table 4.3.

If one looks even more into the charging behavior, one can see that two previous facts that were found without triboelectric charging have to be reconsidered. Previously, by far the most amount of charge was carried by the smallest grains, but with the second smallest grains having the largest rate, this is not categorically true anymore. The smallest and second smallest bins now carry nearly equal amounts of charge The amount of charge carried by each bin can be estimated by multiplying the average bin charge by its respective number density $\langle q \rangle \, n_{\mathrm{a_i}}$.

Additionally, a shift in how much charge each dust bin carriers, relative to one another has occurred. As can be seen in the third table of table (4.2), previously the first bin held more than two thirds of all of the dust grain charge. But now, the first and second bin hold nearly all the charge of all dust bins combined. To compare the average bin charge divided by its respective number density better with the electron and molecules concentrations, we also show average bin charge divided by its respective number density normalized to the number density of hydrogen nuclei $n_{\langle H \rangle}$ in the fourth table.

Note here, that including triboelectric charging increases the total amount of charge on the dust grains. This is most likely due the large grains becoming less negative and therefore being able to react more readily with the free electrons. An indication of this being true can be seen by comparing the electron concentrations of the simulations with and without triboelectric charging. We find that the electron concentration drops by more than a factor of two. Previously at this point, we find an electron concentration of 4.2×10^{-15} and we now find a concentration of 1.8×10^{-15}. This of course has an effect on the positive molecules in the gas as well, as we find more $NH_4{}^+$ in the simulations with triboelectric charging. One finds an increase by a bit more than a factor of two,

from 6.1×10^{-13} to 1.4×10^{-12}. This is an increase by roughly the same amount as the electrons decrease and is not too surprising remembering our findings in Section .

It can therefore be concluded that including triboelectric charging can have an impact on the overall charge balance, and it is important to not just consider small grains. The large grains, whilst not carrying a large amount of total charge, are still vital in creating this cascade of charge transport.

4.4 Discussion and Outlook

While these results are very exciting, it is important to notice that they are preliminary and limited to a single point in the disk and therefore tentative at best. Ideally, a full simulation would have been undertaken where several different points could have been discussed, but due to code and time limitations this was not possible. But, there are several different parameters that we would like to discuss, in particular if the results that we find could have an impact on the electric fields and lightning.

4.4.1 Numerical resolution of the grain size distribution

It is important to discuss the impact of increasing the dust grain sizes and number of dust grain bins would have on the results, because we want to ensure that the quality of our results is not dependent on the numerical parameters, such as number of size bins, coverage of the complete size domain from sub-micron to millimeter, and setting of charge interval boundaries. We saw already that, if one changes the power law fit index, that the results can change, but this is simply due to the fact that the code can account for larger grains in that case.

Firstly, it would be important to increased the dust bin numbers to evaluate if there are potential effects of the numerical implementation on the results. Ideally one would like to not see significant changes in the results if we effectively increase the resolution of how the dust charge distribution is represented.

It would also be important to test for different dust grain size fit parameters and make sure this way that we account for millimeter size grains. This could

Table 4.2: Comparison between Fig. 4.5 and Fig. 4.6 of the different quantities that describe the charging behavior of the dust grains. In particular I compare the average charge $\langle q \rangle$, the average charge per dust bin radius $\langle q/a_i \rangle$, the average charge times the respective dust number density $\langle q \rangle n_{\mathrm{a_i}}$ and the average charge times the respective dust number density normalized to the number density of hydrogen nuclei $n_{\langle H \rangle}$, $\langle q \rangle n_{\mathrm{a_i}}/n_{\langle H \rangle}$. Here $n_{\mathrm{a_i}}$ is the dust number density of the i-th bin. The results for simulation without triboelectric charging are designated via "off" and the ones with triboelectric charging are designated via "on".

$\langle q \rangle$

bin	off	on
a_{00}	-29.7	-49.48
a_{01}	-69.49	-346.46
a_{02}	-193.02	-240.36
a_{03}	-711.61	-703.11
a_{04}	-4074.11	-3916.67
a_{05}	-54828.35	-36301.9

$\langle q/a_i \rangle$ [μm^{-1}]

bin	tribo off	tribo on
a_{00}	-409.17	-656.08
a_{01}	-410.12	-1714.71
a_{02}	-404.31	-598.58
a_{03}	-403.63	-504.12
a_{04}	-403.13	-381.46
a_{05}	-403.08	-279.00

$\langle q \rangle n_{\mathrm{a_i}}$ [cm^{-3}]

bin	tribo off	tribo on
a_{00}	-2636.47	-4391.74
a_{01}	-847.23	-4224.42
a_{02}	-215.66	-268.55
a_{03}	-39.266	-38.79
a_{04}	-4.04	-3.89
a_{05}	-0.14	-0.09

$\langle q \rangle n_{\mathrm{a_i}}/n_{\langle H \rangle}$

bin	tribo off	tribo on
a_{00}	-4.3×10^{-13}	-7.2×10^{-13}
a_{01}	-1.4×10^{-13}	-6.9×10^{-13}
a_{02}	-3.5×10^{-14}	-4.4×10^{-14}
a_{03}	-6.4×10^{-15}	-6.4×10^{-15}
a_{04}	-6.6×10^{-16}	-6.4×10^{-16}
a_{05}	-2.3×10^{-17}	-1.5×10^{-17}

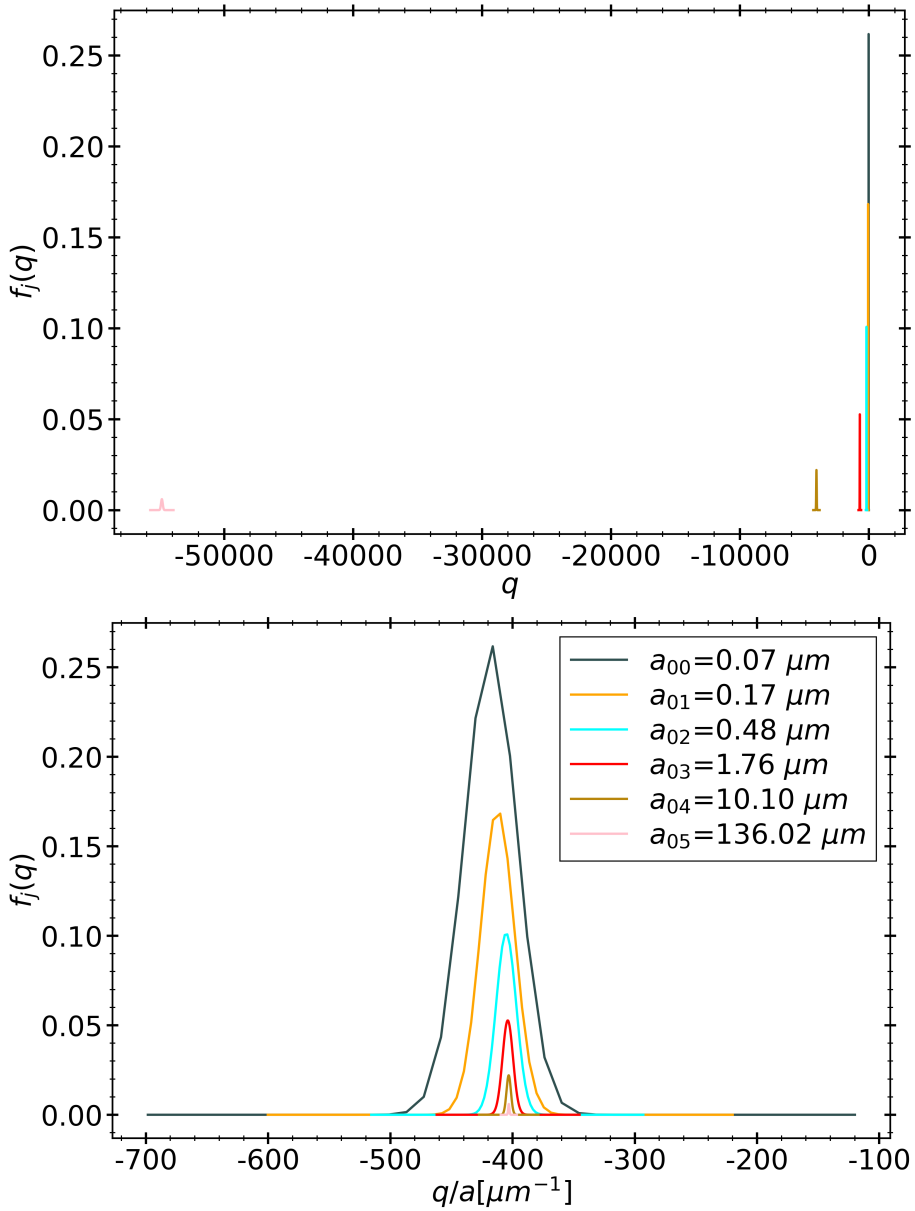

Figure 4.5: The dust charge distribution for the simulated point (see Tab. 4.1) but with triboelectric charging turned of to give the reader an overview how the dust charge distribution would usually look.

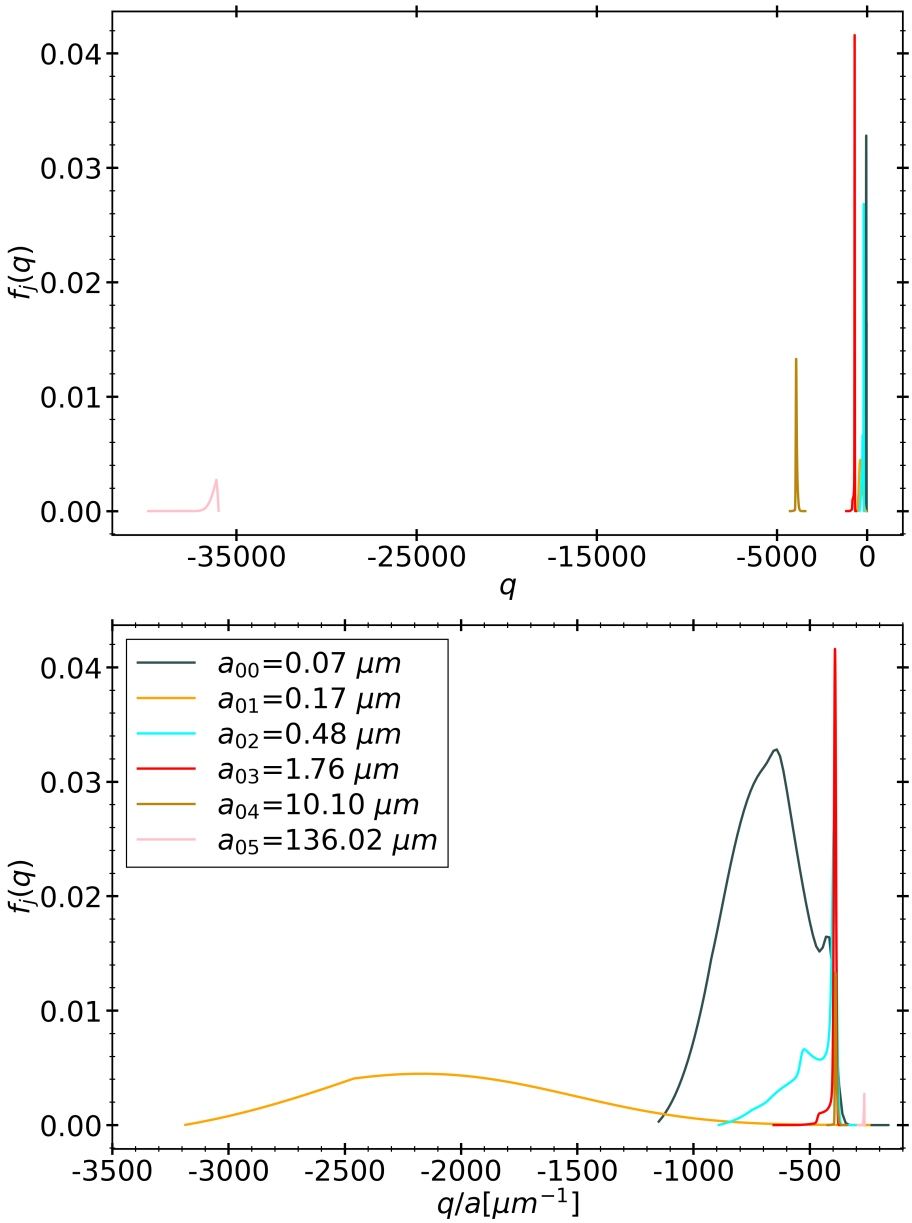

Figure 4.6: The dust charge distribution for the simulated point (see Tab. 4.1) with triboelectric charging turned on. These two plots show the new dust charge distribution in the linear representation of the y-axis, to allow better comparison to the old results Fig. 4.5.

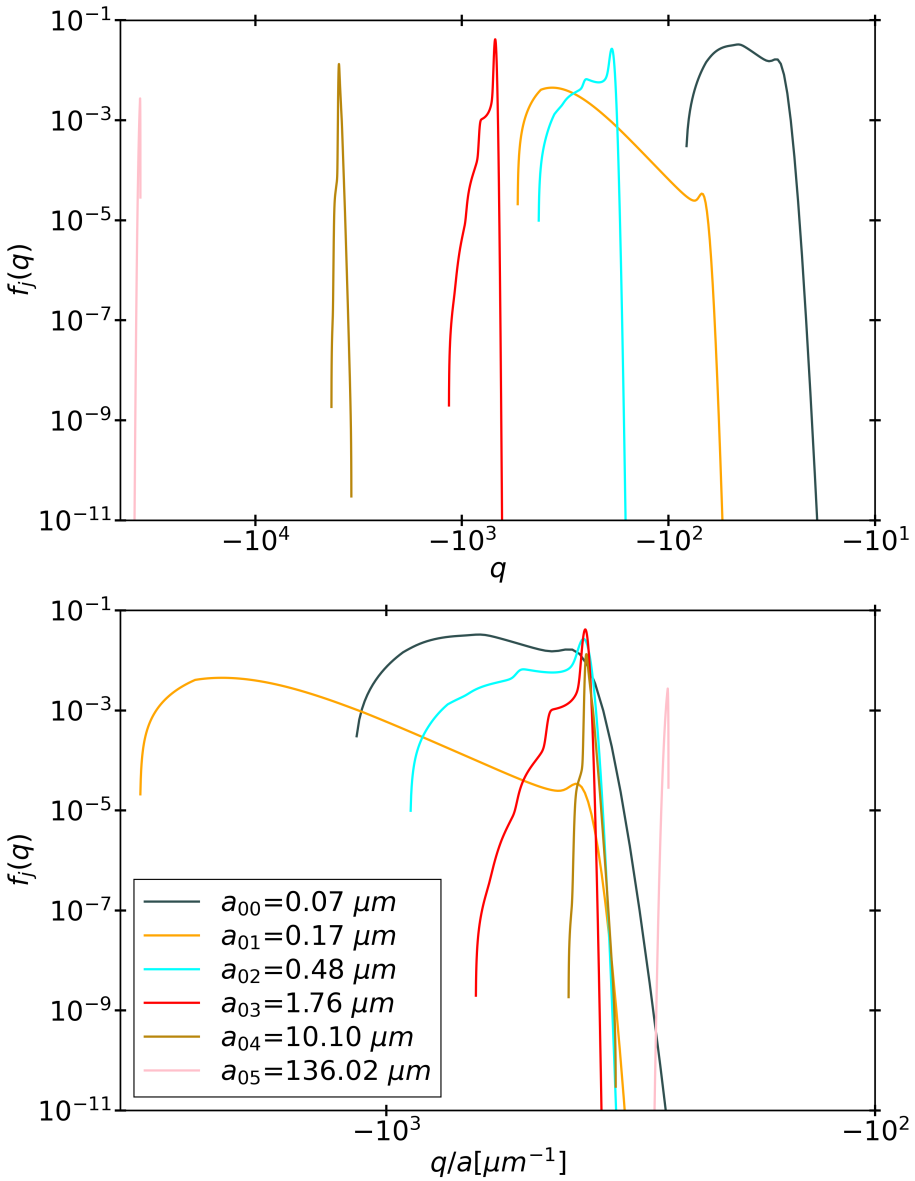

Figure 4.7: Same as Fig. 4.6 but these two plots have the y-axis presented in logarithmic form as it reveals a bit more of of how the charge is distributed in between the different bins.

Table 4.3: Collection of the different coulomb barriers, kinetic energies and ration between the two of all the different triboelectric reactions considered in the model.

interaction	$E_{\rm col}$ [ergs]	$E_{\rm kin}$ [ergs]	$E_{\rm col}/E_{\rm kin}$	$E_{\rm kin}/E_{\rm col}$
a_{00}, a_{01}	1.27×10^{-10}	9.91×10^{-14}	1.28×10^{3}	7.80×10^{-4}
a_{00}, a_{02}	5.51×10^{-11}	9.96×10^{-14}	5.53×10^{2}	1.81×10^{-3}
a_{00}, a_{03}	5.14×10^{-11}	1.08×10^{-13}	4.76×10^{2}	2.10×10^{-3}
a_{00}, a_{04}	4.02×10^{-11}	3.60×10^{-13}	1.12×10^{2}	8.96×10^{-3}
a_{00}, a_{05}	2.96×10^{-11}	1.41×10^{-11}	2.10	4.76×10^{-1}
a_{01}, a_{02}	2.92×10^{-10}	1.03×10^{-13}	2.84×10^{3}	3.53×10^{-4}
a_{01}, a_{03}	3.04×10^{-10}	2.03×10^{-13}	1.50×10^{3}	6.68×10^{-4}
a_{01}, a_{04}	2.48×10^{-10}	3.50×10^{-12}	7.09×10^{1}	1.41×10^{-2}
a_{01}, a_{05}	1.85×10^{-10}	1.87×10^{-10}	9.89×10^{-1}	1.01
a_{02}, a_{03}	2.60×10^{-10}	1.60×10^{-12}	1.62×10^{2}	6.15×10^{-3}
a_{02}, a_{04}	2.39×10^{-10}	7.23×10^{-11}	3.30	3.03×10^{-1}
a_{02}, a_{05}	1.82×10^{-10}	4.19×10^{-9}	4.34×10^{-2}	2.30×10^{1}
a_{03}, a_{04}	6.65×10^{-10}	2.71×10^{-9}	2.45×10^{-1}	4.08
a_{03}, a_{05}	5.64×10^{-10}	2.08×10^{-7}	2.71×10^{-3}	3.69×10^{2}
a_{04}, a_{05}	2.31×10^{-9}	3.41×10^{-5}	6.78×10^{-5}	1.48×10^{4}

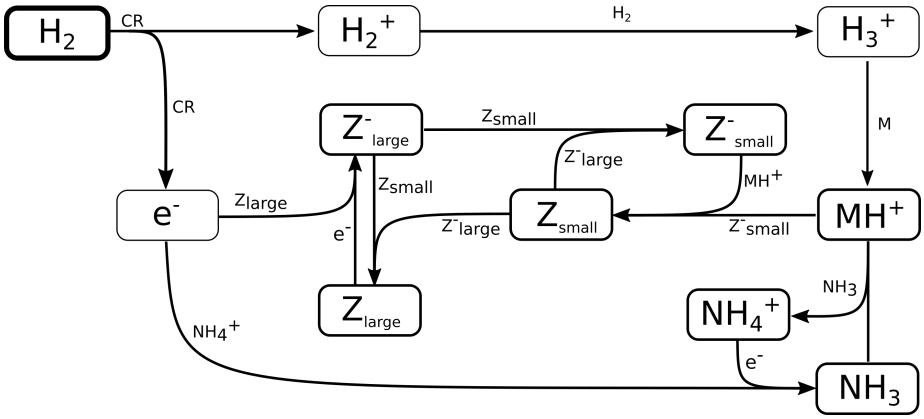

Figure 4.8: An updated version of the reaction pathways which establish the charge balance one finds in the midplane (compare Fig.2.8)

have large implications on the quality and quantities in the results. It could reveal that when one can reliably overcomes the coulomb barrier between largest and smallest grains, the smallest grains dominate the overall charge again.

4.4.2 Changes in the amount of charge transferred Δq

As mentioned in Section 4.2.1, it was tried to implement a method that accounts for a realistic amount of charges transferred when two dust grains interact with each other. We ultimately chose a numerically more stable but not physically motivated method. We would expect some quantitative changes if a more realistic method is implemented, but not necessarily qualitative. It would be important to make sure the realistic implementation would be usable, nonetheless, just to ensure we have an as close as possible representation of reality.

4.4.3 Different physical conditions

Testing a full simulation, or maybe in the beginning just different points of the simulation, could be one of the most impactful changes to the results. We would like to quickly discuss three different areas of the disks here.

We would expect that there are certain areas in the disks where triboelectric charging makes very little to no impact. The regions D-F that we identified in Section 2.2.2, very high up in disk, are so photodominated, that we would not expect for triboelectric charging to be competitive with photoionization. Additionally, the Coulomb barrier might be even harder to overcome, as the dust grains in these areas are very positively charged, even more positively charged as the grains are negatively charged in the midplane.

Other areas in the midplane could be interesting to investigate. We already have an indication from Fig. 4.3 that somewhere around 0.6 au, electron attachment could become the dominant charging mechanism again. Therefore it is important to investigate in which areas exactly triboelectric charging is relevant and which parameters such as shielding or temperature could have impacts on how relevant the contribution of triboelectric charging is.

Lastly we would like to discuss an area of the disk that we find to be a promising candidate for what we called region X, a region where dust grains

would totally dominate the charge balance. In other words, an area where positive charged dust grains would be the most abundant positively charged species in addition to negatively charged dust grains being the most abundant negative charge carrier.

As can be seen in Fig. 2.3 there are large areas where the grains are mostly neutral. Triboelectric charging could create a charge distribution where the larger bins would be positively charged and the smaller one negatively charged. This would resemble what occurs for example in volcanic eruptions on earth where lightning occurs.

It could also have a effect on the electric field magnitudes. If one looks again at our electric field equation, equation 3.6, one can see that we accounted already for a contribution of positive grains. But, claiming that these dust grains would dominate the overall charge balance would be hard to state, as these areas in the disk are less shielded than the midplane. Hence, these regions could be still photodominated. So either triboelectric charging would not matter, similar to how we discussed the higher areas of the disk, or the resulting ions and electrons from the photoionization of atoms or molecules would dominate the overall charge balance. Nonetheless, studying more areas of the disk, and undergoing the necessary numerical improvements to make this possible are on the upcoming agenda.

It is important to point out that in previous studies such as Muranushi and Tomiyasu [2009] where they implemented triboelectric charging and found regions where they deem lightning to be possible, only triboelectric charging was implemented and no other charging processes where considered. Hence this work lays the ground work for a complete study of all relevant charging processes for dust grains.

4.4.4 Effects on the emergence of lightning

Lastly we would like to discuss whether these results could have an impact on the generation of the electric fields and therefore lightning. One can do this by using equation 3.6 and including the necessary densities of the different dust grain bins, the electrons and the $NH_4{}^+$.

When doing this, one finds an increase in the electric field by roughly a factor

of 2. Which is of course not even remotely enough to overcome the critical field in these areas. This increase can mostly be accounted for, by having more charge on the smaller grains compared to the results without triboelectric charging. Since in our model, smaller grains are more abundant, they would contribute more in equation 3.6.

5

Implementation of non-equilibrium chemistry into the MARCS code and the Chapman cycle

This chapter illustrates the work that has been done during the secondment at the University of Copenhagen.
At the group in Copenhagen, a large effort had been undertaken in updating their radiative transfer code, MARCS, to make it usable for simulating exoplanets. One part of these efforts is to integrate non-equilibrium chemistry into the MARCS code. In this chapter, I will explain my part of these efforts of implementing non-equilibrium chemistry and show some preliminary results by testing our implementation of the Chapman cycle.
The chapter is structured in the following way, section 5.1 gives a rudimentary explanation of the MARCS code and recent improvements.
Section 5.2 gives a short explanation how the KROME code works and explain how we implemented KROME into MARCS.

Section 5.3 will give a short explanation into the Chapman cycle itself.
Section 5.4 shows some first results showing that the implementation is working and discusses these results briefly.

5.1 MARCS and the MSG project

The MARCS code in its original iteration Gustafsson et al. [1975] was a radiative transfer code designed to solve the radiative transfer for solar-like stars atmosphere in an effective temperature range from 8000 K down to 2500 K Gustafsson et al. [2008]. The efforts of group in Copenhagen, were part of the MSG project, to make the MARCS code applicable to exoplanetary atmospheres. This was achieved by coupling the MARCS code with the StaticWeather Code Helling and Woitke [2006] and the GGchem code Woitke et al. [2018], creating the abbreviation MSG Jørgensen et al..

The StaticWeather code is a kinetic cloud formation code designed to investigate cloud formation in exoplanetary atmospheres. Static weather is a 1D kinetic cloud formation model, modeling cloud population using the moment method for mixed material composition cloud particles, coupled to equilibrium gas-phase chemistry through elemental depletion. Nucleation is treated using a modified classical nucleation theory approach, particles settle through equilibrium drift dependent on size. A static cloud deck is achieved by a relaxation timescale for atmospheric composition towards an undepleted cloud free gas phase, from the deep atmosphere.

The GGchem code is a code designed to solve the concentrations and abundances of the relevant species in thermal equilibrium. The code achieves this, by trying to minimize the total Gibbs free energy at the given temperature in the atmosphere layer.

5.2 KROME

Whilst local thermal equilibrium can be a good approximation for certain circumstances that are found in exoplanetary atmospheres, a more accurate approach would be to also have a way to handle non-equilibrium chemistry. There

are several common occurrences in atmospheric modeling where non-equilibrium chemistry is necessary in order to simulate realistic circumstances, like the influence of the radiation of the host star or other sources, mixing processes between different atmospheric layers, influences of discharge processes within atmospheres like lightning or emissions from the surface, either from metabolic processes or from volcanic sources for example.

In order to account for such non-equilibrium influences, we implemented the KROME code Grassi et al. [2014] into the new MSG framework. KROME follows are very typical kinetic equilibrium approach, where for every species n there change in a certain time frame will become ideally zero, or more often, smaller than a certain tolerance.

$$\frac{dn_i}{dt} = F_j - D_j = \sum_j k_j \Pi_j n_j - \sum_j k_j \Pi_j n_j \tag{5.1}$$

where n_i is the number density of a specific species, F_j is a sum of all formation reactions of the said species, D_j a sum of all destruction reactions. Both sums are sums of the respective rates for each reaction, where those rates are calculated as a product of the respective coefficients k_j and the respective species involved, which is accounted for by a product of the different species involved in the the reaction n_j. To solve this stiff set of ordinary differential equations KROME uses the DLSODES solver from the DVODE package.

Within the MARCS framework KROME is implemented in the following way. For each iteration of MARCS towards a self-consistent, stable solution, we first calculate the GGchem thermodynamical equilibrium abundance of all included species. To avoid being overwhelmed computationally, we initially implemented the non-equilibrium for only a small subset of these species, keeping the rest at their equilibrium values. For example, in our implementation of the Chapman cycle, only the relevant Oxygen species are part of the chemical network of KROME. After GGchem has finished, we call KROME and let it run until a steady state solution has been reached for the selected species starting from the equilibrium values.

5.3 Chapman Cycle

In order to test our implementation of non-equilibrium chemistry we chose to implement the Chapman cycle. The Chapman cycle is set of four reactions which are responsible for the ozone layer creation in earths atmosphere. The main reaction that makes the whole cycle possible is the photodissociation of molecular oxygen by energetic UV radiation, at least UVB (Eq. 5.2). The created oxygen atoms can create Ozone molecules, by reacting with molecular oxygen and an additional reaction partner M, needed for the sake of energy conservation (Eq. 5.3). The created Ozone molecule can react back to molecular oxygen via two pathways. Either another photodissociation with slightly less energetic UV radiation (Eq. 5.4) or a recombination with atomic oxygen (Eq. 5.5). The necessary rate coefficients were taken from the NIST database Linstrom and Mallard [2022].

$$O_2 + h\nu_{<242\text{nm}} \rightarrow O + O \tag{5.2}$$

$$O + O_2 + M \rightarrow O_3 + M \tag{5.3}$$

$$O_3 + h\nu_{<240-310\text{nm}} \rightarrow O_2 + O \tag{5.4}$$

$$O_3 + O \rightarrow 2O_2 \tag{5.5}$$

5.4 Results

In order to test the validity of our implementation and see the effects of non-equilibrium chemistry, a MSG model was run and a comparison between the equilibrium results from GGchem and the non-equilibrium results from the KROME implementation and the Chapman cycle network. The MSG simulation was done with solar elemental abundances, at an effective temperature of 2500 K and a log(g) of 4.5. The modeled planet is at a distance of 1 AU from its host star, represented by a black body of 5700 K, representative of the sun.

We plotted the number densities of the different relevant oxygen species of the Chapman cycle, atomic oxygen, molecular oxygen and ozone in each layer of the atmosphere and compare our KROME implementation against a run without the inclusion of non-equilibrium chemistry 5.1. What can be clearly

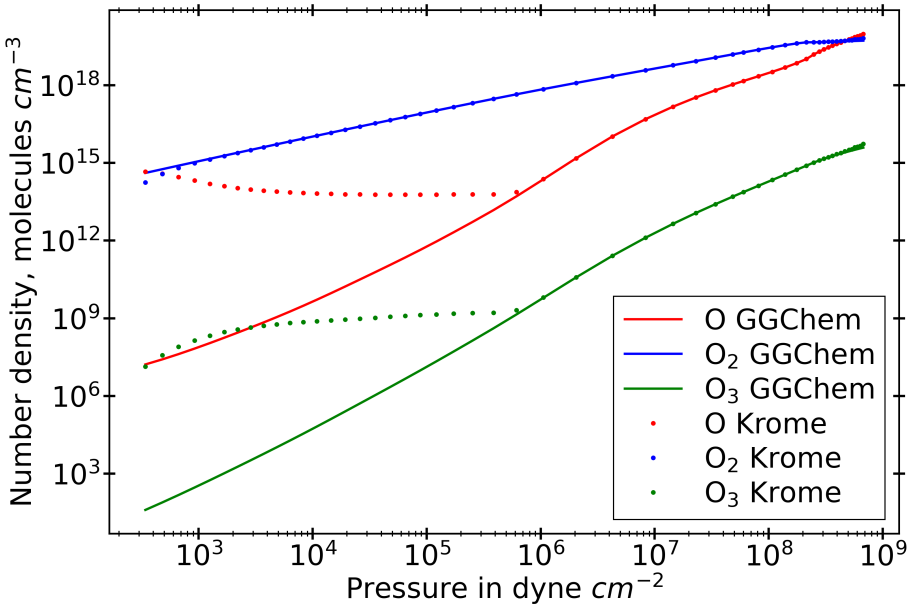

Figure 5.1: Comparison of the number density of the oxygen species that are relevant in the Chapman cycle in the planet that we simulated, between the results one would get with a chemical equilibrium code (solid lines - GGchem) and our implementation of non-equilibrium chemistry (dots - KROME). The x axis shows the pressure [dyne cm^{-2}] levels, representing going deeper into the planets atmosphere

seen in this plot, is that with the KROME implementation, at the higher layers of the atmosphere we create a, by several orders of magnitude, larger amount of atomic oxygen and ozone compared to the equilibrium runs with GGchem. This can be explained by the amount of shielding that the atmosphere provides. Higher up, the planetary atmosphere will not be able to shield against the UV radiation, which results in the first reaction of the Chapman cycle to be able to occur in the first place. The lower we in the atmosphere, the lower the UV radiation and therefore at some point, the whole cycle stops. It is very encouraging to see that ones this point is reached that the KROME results are virtually identical to the GGchem results, because at this point we would expect the investigated species to not be under the influence of any non-equilibrium effects which are part of the chemical network we implemented.

6

Conclusions & Outlook

Conclusion and Outlook of Chapter 2 Six different regions within the disk were identified, which were analyzed with regards of how dust grains charge and if they contribute to the overall charge balance (refer again to Fig.2.6). The upper regions, are photo dominated where dust grains charge positively due to their interaction with the radiation present. The most abundant negative charge carrier are electrons with the most abundant positive charge carriers being the ionized form of the the main electron donators. For the most upper region, region F, the most abundant positive species would therefore be H^+. For the region below F, region E, it would be C^+. For the lowest of the photodominated regions, region D, S^+ is the most abundant positive species. The overall charge balance in these regions is not affected by the dust grains.

The three lower regions that were identified show a more complex behavior. These regions are not photo-dominated, due to the strong shielding from UV and X-ray radiation. Cosmic rays are the only type of radiation that influence the charge balance in these regions. All of these regions are located in the

midplane of the disk.

The most outward (3 to 100 au) of the three midplane regions identified, region C, was coined the metal-poor region. Named metal-poor due to the fact that most species are frozen out into ices, hence not available to the gas phase. The most abundant charged species are electrons and $H_3{}^+$. However it is noteworthy that dust grains are starting to become more and more relevant and have similar concentrations to the electrons on the inner areas of this region.

The next more inwards region ($\approx$ 1 to 3 au), region B, shows a highly complex hydrocarbon chemistry due to the fact that nitrogen and oxygen bearing species being frozen out onto ices whilst carbon bearing species are not frozen out. The most abundant positive charge carrier are $C_3H_3{}^+$ molecules which have the highest proton affinity of all protonated molecules we consider. Dust grains are the most abundant negative charge carries. Electrons are still not negligible compared to the negatively charged dust grains.

The most inward region ($<$ 1 au), region A, is the only region considered dust dominated, since the electron concentration dropping to values as low as 10^{-18}. This is due to the electrons attaching to the dust grains. Together with $NH_4{}^+$ molecules negatively charged dust grains dominate the overall charge balance in this region. Region A or regions with similar shielding and temperatures are the ones mostly likely for lightning to occur in.

A single point of region A was then chosen to investigate the impact different parameters could have on the dust grains charging behavior and the charge balance. These parameters were, the minimum dust grain size, the dust to gas ratio, the cosmic ray ionization rate, the gas density and the dust temperature.

It was found that increasing the minimum dust grain size will result in less charged dust grains, due to the effect that larger grains will have a smaller total surface area, hence being able to hold less charges in total.

Lowering the cosmic ray ionization rate decreases the electron abundances significantly, due to lower cosmic ray ionization rates resulting in less ionization of hydrogen molecules which is the only process that can create free electrons in the areas analyzed.

Increasing the dust to gas ratio decreases the electron concentration. This can be explained by considering that if we increase the dust to gas ratio, we

also increase the amount of potential reaction partners for the electrons, hence more dust grains can take up free electrons and therefore lowering their concentration in the gas. Note here the implications on the magneto rotational instability. Firstly, in the areas we investigate, the electron concentration is already below the critical threshold for MRI to occur, already strengthening the link between dust grain charging and the creation of dead zones. Furthermore, in our studies we increase the dust to gas ratio up to the, for streaming instabilities important point of unity and show that this even further decreases the electron concentration.

An increase in the gas density also results in a decrease of the electron concentration. This can be explained by two factors. Firstly, increasing the gas density also increases the shielding and therefore lowers the cosmic ray ionization rate. Secondly, increasing the gas density also increases the recombination of electrons with molecules in the gas and since, as previously mentioned, the recombination rates scale with the gas number density squared whilst the cosmic ray ionization only scaling with the gas number density linearly.

Changing the temperature has a very complex impact. At very low temperatures ($\leq$ 200 K), one replicates the conditions in region B, resulting in freeze outs of nitrogen and oxygen. Between 300 K and 1300 K only marginal changes are visible in the charge balance. Above 1400 K, Na^+ becomes the dominant positive charge carrier, due to collisional ionization of Na. Therefore, at higher temperatures, the electron concentration increases significantly. Note however another trend when we increase the temperature and that is the decrease in q/a for the dust grains. This can be explained by the limiting factor, for how much the dust grains can charge via electron attachment, being the interaction between the Coulomb barrier and the thermal velocity of the electrons. Since increasing the dust temperature also increases the gas temperature we increase the thermal velocity of the electrons allowing the Coulomb barrier to overcome more easily.

Lastly, it was found that the dust grains charge in a uniform matter. This can be seen by looking at the dust grain charge distribution and normalizing the charge on the dust rains for the respective dust grain size q/a [μm^{-1}]. For all dust bins in the mid plane q/a to be $\approx$ -350. This fact is not too surprising and can be explained in two ways. Firstly the total amount of charge a dust grain can carry q scales with its surface area. Additionally the rates of much a dust

grain charges also scales with its surface area. Hence increasing the dust grains size a should not increase or decrease its overall charge per radius q/a. Another way of explaining this behavior could be to consider that q/a represents the electrostatic potential of the dust grains and that when one looks at the rate coefficients, all of them scale in some form with q/a.

On the outlook of this section one has to mention MRI again. One can see that when we consider dust grain charging, in region A the electron concentration can drop below the usual threshold at which MRI can occur ($\geq 10^{-13}$ (see again Inutsuka and Sano [2005]). It could be interesting to combine the new findings of this work with the parameterized MRI implementation in ProDiMo from Thi et al. [2019]. In this work we tend to find lower electron concentrations then Thi et al. [2019], hence finding a larger dead zone could be the result of a combining the two works.

Conclusion and Outlook of Chapter 3 On top of the results of Chapter 2 a turbulent charge separation model was developed. The aim of this model was to investigate whether the conditions that were found in the mid plane are conducive to the emergence of lightning.

The idea behind this model is that both of the main contributors of the charge balance, $NH_4{}^+$ and negatively charged dust grains, would feel the acceleration of a turbulent eddy in a different way. This is due the frictional forces at hand, that would result in the centrifugal force being applied to the dust grains in quicker manner than for the molecules. As the dust grains feel the change in movement faster when being caught in a turbulent eddy, the $NH_4{}^+$ molecules would be lagging behind until they match the drift velocity of the dust grains. This lag would create a spatial separation that would result in an electric field establishing itself.

In order to see if these electric fields are large enough for lightning to emerge, one has to see if they could overcome the critical electric field. The critical electric field, is the electric field at which the electrons can ionize the medium around them and start an electron avalanche. In this study, the electric fields are several orders of magnitude smaller than the critical electric field, hence an emerge of lightning in this way would be highly unlikely. The same parameters as in the previous chapter were tested to see if they could have an impact on the magnitude of the electric fields, but none of the parameters came remotely

close at having a noticeable impact.

The outlook for this chapter is closely linked to the work described in chapter 4 hence their outlooks will be combined and shown at the end of the conclusion of chapter 4.

Conclusion and Outlook of Chapter 4 The main result of chapter 4 is the preliminary but successful implementation of triboelectric charging into the charge chemistry framework of ProDiMo. This new approach of handling triboelectric rates and rate coefficients has similarities to the larger chemistry framework of ProDiMo by making use of a Newton-Raphson approach to solve the coupled non-linear equations describing the dust grain charging as function of size and charge f(a,q).

The new implementation of triboelectric charging can reveal some interesting changes in the dust grain charge distribution. One finds firstly that one has to consider large enough grains for triboelectric charging to take an effect, as the kinetic energy of the dust grain particles has to be large enough to overcome the Coulomb barrier. In this work we find that the larger collision partner needs to be at least several 10 - 100 μm in size in order for collisions to happen. If triboelectric charging happens, we can see changes in the charge chemistry at the point in the midplane. The previously found paradigm in chapter 2 of a constant q/a is not true anymore an we can see how in the larger dust bins q/a gets less negative whilst for the smaller dust grain bins it increases. This indicates a charge transfer happening from the larger grains to the smaller grains. This charge transfer dominates the overall dust grain charge distribution as it significantly increases the amounts of charge carried by the smallest grains.

Additionally, the way the charge chemistry establishes itself changes slightly compared to the previous findings in chapter 2. Whilst the overall trends are similar, an extra intermediate step has to be considered now, where only the largest grains react with electrons and then carry on these extra negative charges onto the smaller grains.

The outlook of this chapter would be at the same time very enthusiastic, due to the intriguing new results, but also cautious, due to a lot of open questions and still some problems with the implementation itself. Whilst the implementation was overall a success, in the sense that it is capable of producing preliminary

results, it must be noted that it is at this point not fit for a full ProDiMo simulation. This is due to the fact that the boundaries of the dust grain charge distribution still have to be adjusted by hand, for every single point of the simulation and for every dust bin. Additional work is required in understanding the magnitudes of the charge exchanges better, so that the boundaries could be set a priori or automated. This requires better understanding of the mechanism of triboelectric charging. A fundamental issues is that triboelectric charging when it is discussed in the literature, is nearly exclusively discussed between different materials. In the case of different materials one could estimate the charge transfer from a simple comparison of the workfunctions of the materials. In our case we consider dust grains and therefore materials of the same kind. In such a case a workfunction comparison would not work and the amounts of charge transferred would be marginal. But we know from experiments such as Jungmann et al. [2021] that triboelectric charging still occurs between materials of the same kind, and also results in very large amounts of charge transferred. A bridging of the knowledge gap is required.

If the process of setting the boundaries can be automated a full disk simulation should be possible, and would also be needed to test the influence of different parameters on triboelectric charging. In addition full simulations would be needed to potentially find the elusive region X, where the charge balance is completely dominated by dust grains, both positively and negatively charged. In these regions we could then apply the turbulent charge separation model described in chapter 3 and test the electric fields generated again and see if they could be larger in magnitude then the critical electric fields.

Conclusion and Outlook of Chapter 5 The main conclusion from chapter 5 is the successful implementation of KROME into MARCS as part of the MSG project. With this implementation the Chapman cycle was tested and found to be a feasible mechanism for the creation of ozone in the upper layers of the test planet.

With this implementation a lot of different non-equilibrium effects can now be studied. Firstly different photodissociation process can now be implemented and being investigated with the improved MARCS code.

For the MSG project and the work of the group in Copenhagen in particular interesting could be the non-equilibrium effects that potential life has on an

exoplanets atmosphere. This implementation could be used on testing whether certain biosignatures (for example CH_4, CO_2, O_2, N_2O from Earth) are actually biosignatures or could be explained by other effects, such as volcanic outgassing, photochemistry or also lightning.

A

Appendix

This appendix consists of parts of the appendix of my publication Balduin et al. [2023]. It has mostly been added for the sake of completeness and comprehension, as the appendix is referred to several times in said publication. For the sake of transparency it must be mentioned that section A.1 has been written by myself, including the plots.
Section A.2 has been written by my coauthor Peter Woitke.
Section A.3 is a combined effort by myself and my coauthor Peter Woitke.

A.1 On the impact of automatically generated charge exchange and protonation reactions

In this section, we investigate the effect that automatically generated charge exchange, protonation, and endothermic reactions can have on our model. For this, we incorporated three different models (Tab. A.1): one where we do not

Table A.1: The three different models we considered when testing the influence of automatically generated reactions.

Reac. Type	noEX	standard	EX
Charge Exchange	×	✓	✓
Proton Exchange	×	×	✓
Endotherm	×	×	✓

allow exchange, protonation, or endothermic reactions to be generated and only use the network as provided, from now on called "noEX"; one where we allow charge exchange reactions to be generated, which is the case for our standard case discussed before; and one where we allow charge exchange, protonation, and endothermic reactions to be generated, from now on called "EX." We note that for endothermic reactions, we set the barrier of the activation energy for the reactions to be at 5000 Kk_b, which equals to 0.431 eV.

To illustrate the differences between the three models, we wanted to show a list of the different reactions considered for the different setups. However, such a list would consider thousands of reactions since our noEX setup consists of 5530 reactions, the standard setup of 7009, and the EX of 8672, and we would have to show the differences with example reactions, meaning reactions of a specific type not considered by a certain setup. Therefore, we have chosen instead to present a curated list of reactions that show what kind of reactions are additionally considered for the different setups (Tab. A.2).

A.1.1 noEx model

For the noEx model in region A, we found that, firstly, the whole region A starts a bit farther in, due to $C_3H_4^+$ dipping at a later point. Secondly, we found that C_4H^+ is more abundant much farther in. For region B, we again found the trend that the region emerges more inward than in our standard case. Overall, we found the chemistry to be very comparable. We however found that the species H2S+ and H2CS+ are more abundant and overcome our set threshold, while SiOH+ and H3CO+ do not overcome this threshold and are therefore no longer abundant. For region C and outward, we found no notable differences.

Table A.2: Example reactions present in the different models[(1)].

Nr.	Educts	Prod.	noEX	Standard	EX	α	β	γ
1	$N^+ + H$	$N + H^+$	✓	✓	✓	1.00E-12	0.00	0.0000
2	$Ar + H_3^+$	$Ar^+ + H + H_2$	✓	✓	✓	3.65E-10	0.00	0.0000
3	$H + CO_2^+$	$H^+ + CO_2$	×	✓	✓	5.00E-10	0.50	0.0000
4	$H^- + CO_2^+$	$H + CO + O$	×	✓	✓	5.00E-10	0.00	0.0000
5	$C + CH_4^+$	$CH^+ + CH_3$	×	×	✓	1.32E-09	0.00	0.0000
6	$C + C_2H^+$	$CH^+ + C2$	×	×	✓	1.32E-09	0.00	4317.7482

[(1)]Reactions that are only in the noEX model (1 and 2) are from exterior references. Exchange reactions added in our standard model (3 and 4) were added as described in Sect. 2.1.5.
Additional reactions present in the EX model (5 and 6) were added again as explained in Sect. 2.1.5.

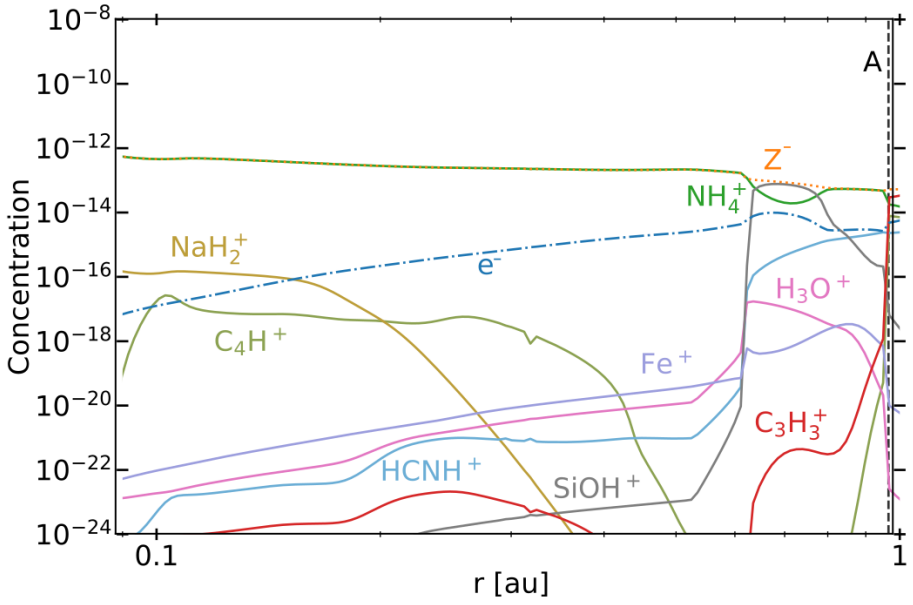

Figure A.1: Results for noEX model in region A. Compare with Fig. 2.7 showing the standard case.

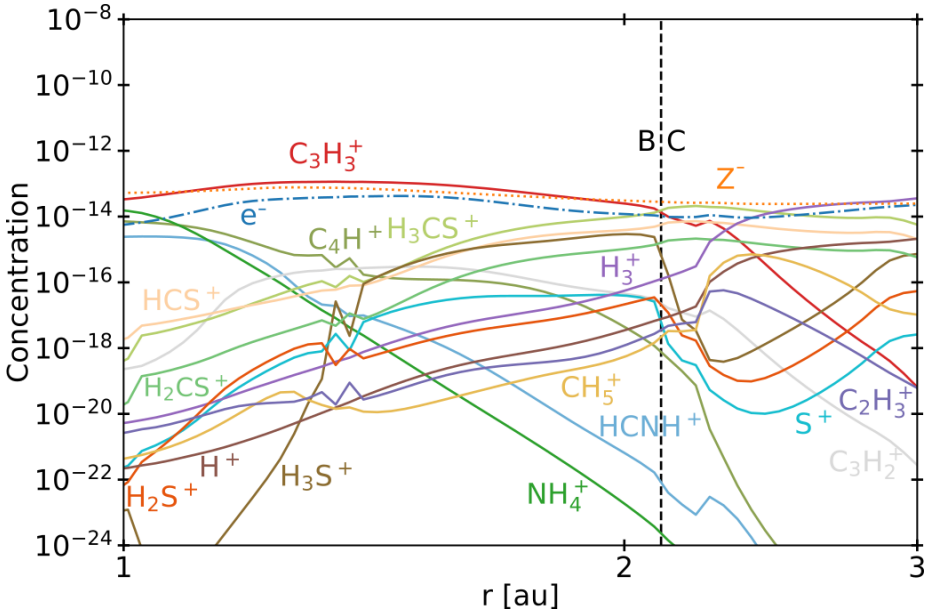

Figure A.2: Results for noEX model in region B. Compare with Fig. 2.9 showing the standard case.

A.1.2 EX model

For region A, we mainly found that compared to our standard model, Na^+ becomes the second most abundant positive charge carrier and replaces $NaH2^+$. In addition, we found that Fe^+ is no longer abundant enough to meet our set threshold. However, we found protonated methanol $CH_3OH_2^+$ to be abundant in the EX model. For region B, we found a much less complex chemistry. In particular, C_4H^+ and $HCNH^+$, which are abundant in our standard model, do not show up anymore. We only found the sulfur bearing species, which are also abundant in the standard model, dominate as the second and third most abundant cations after $C_3H_3^+$. For region C, we again found no significant differences.

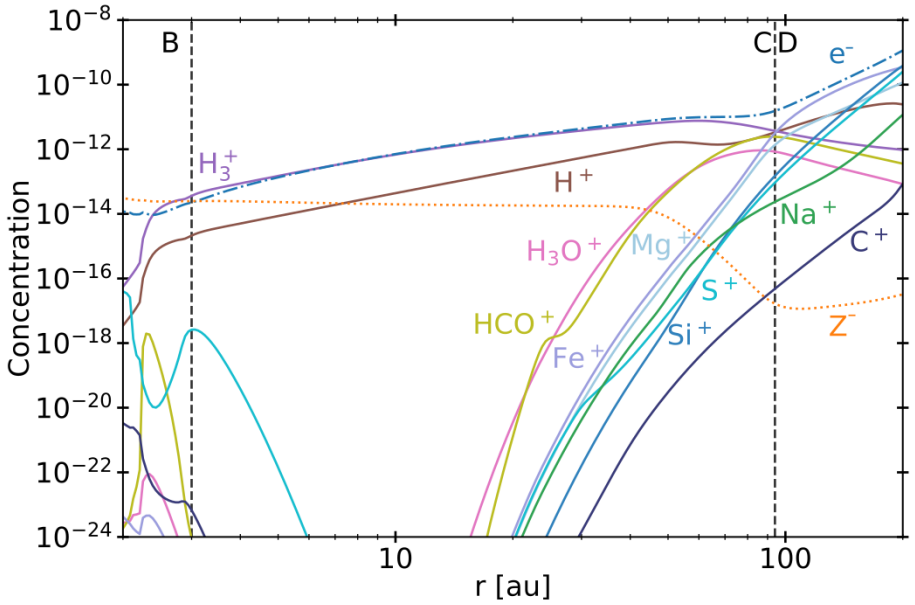

Figure A.3: Results for noEX model in region C. Compare with Fig. 2.9 showing the standard case.

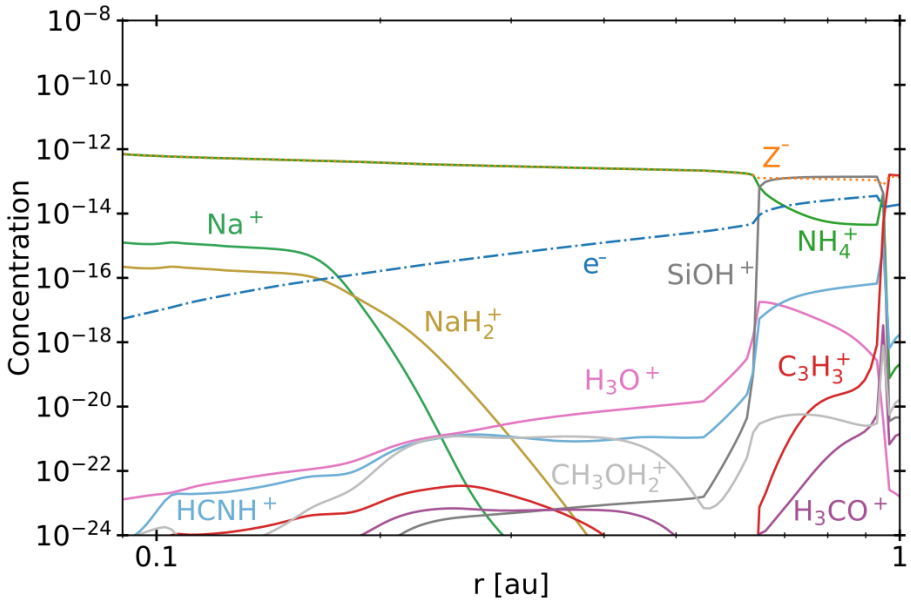

Figure A.4: Results for EX model in region A. Compare with Fig. 2.7 showing the standard case.

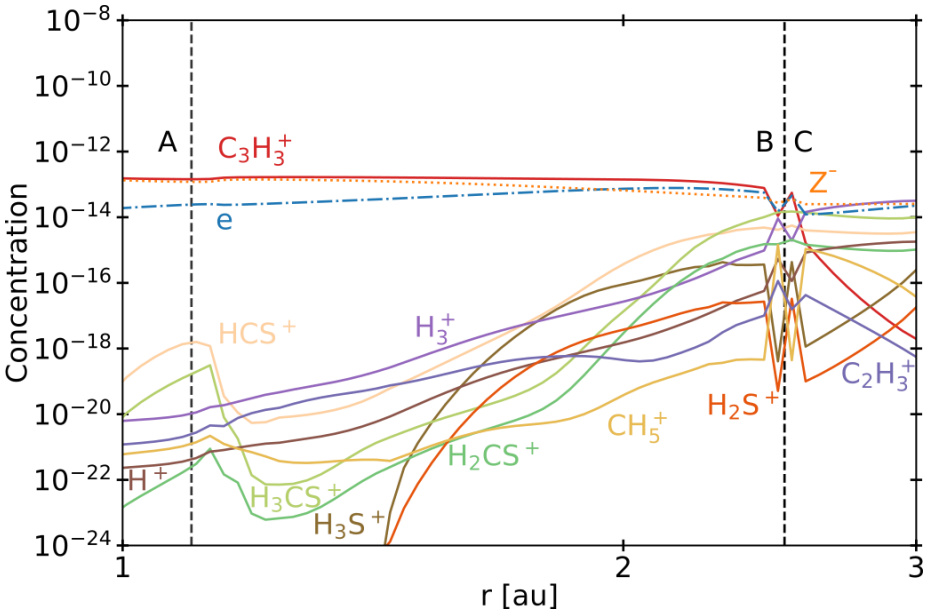

Figure A.5: Results for EX model in region B. Compare with Fig. 2.9 showing the standard case.

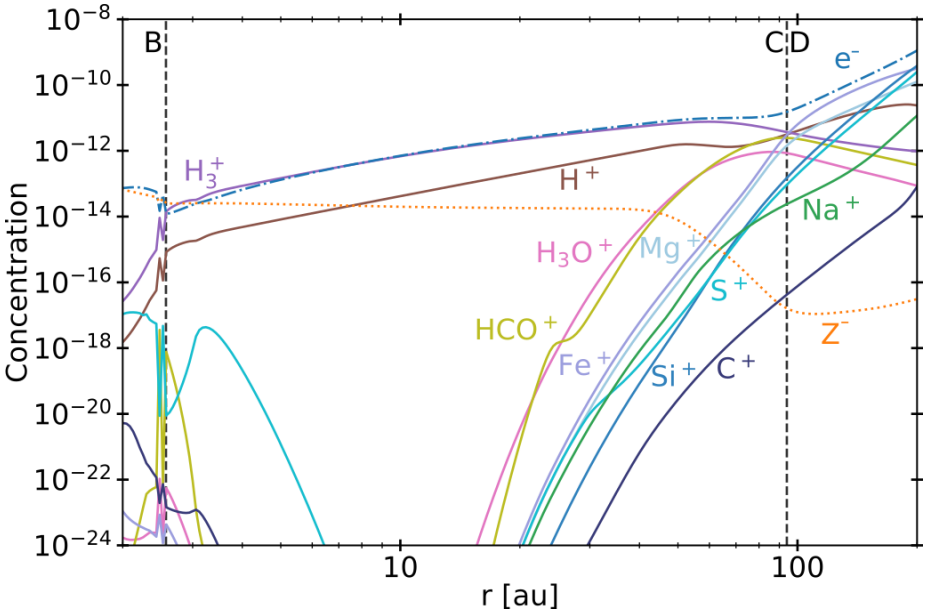

Figure A.6: Results for EX model in region C. Compare with Fig. 2.11 showing the standard case.

A.2 Solving the chemical rate network with dust charge moments

The charge and size distribution of the dust grains are represented in our chemical models by three charge moments, $Z^{+}_{\mathrm{m},j}$, $Z_{\mathrm{m},j}$, and $Z^{-}_{\mathrm{m},j}$, in each dust size bin, using a small number of dust size bins $j \in \{1, \ldots, J\}$. In Sect. 2.1.8, we introduced the effective chemical rates for these moments for photoionization, electron attachment, and charge exchange reactions, which properly describe the overall effect of all grains on the gas and ice chemistry. On one side, the charge distribution function $f_j(q)$ must be known to calculate the effective rate coefficients. However, on the other side, as explained in Sect. 2.1.7, the determination of $f_j(q)$ requires knowing the photon flux and the concentrations of all chemical species, including electrons and molecular anions and cations.

Our formulation with dust charge moments and effective rates still conforms with the basic shape of a coupled system of first-order ODE system,

$$\frac{dn_i}{dt} = P_i - L_i = F_i(\vec{n}) \ , \tag{A.1}$$

which enables us to use numerical ODE solvers to advance the chemistry. The term n_i is the particle density of chemical species i, $\vec{n} = \{n_1, \ldots, n_I\}$ is the solution vector, P_i and L_i are the total production and destruction rates, F_i represents the components of the right-hand side (RHS) vector, and I is the number of chemical species that include $3 \times J$ dust moments. From $\vec{n}$, we could in principle update $f_j(q)$ in each call of the RHS vector, then update the effective rate coefficients, and calculate all F_i. However, this would result in an extremely slow computational method because the calculation of $f_j(q)$ requires the computation of tens of thousands of rates for all individual charging states. In addition, we would need implicit solvers, which require the Jacobian derivative $\partial F_i / \partial n_j$, that is, for each integration step one would need to carry out the determination of $f_j(q)$ a couple of 100 times. Normally in astrochemistry, one can calculate the rate coefficients only once, prior to calling the ODE solver, because the rate coefficients do not depend on the particle densities, and then compute F_i and $\partial F_i / \partial n_j$ from these rate coefficients in very efficient, quick ways. In contrast, according to our formulation of the problem, the rate coefficients here depend on the particle densities in complicated ways.

We figured that there is a much more efficient way to solve our chemical equations by means of an iterative approach. To obtain a time-independent solution of our chemical equations, as used in this paper, we followed the following algorithm:

(1) Provide an initial guess of the particle densities $\vec{n}$ based on the results obtained for the previously solved grid point.

(2) Compute $f_j(q)$ from $\vec{n}$.

(3) Compute all rate coefficients, including the effective rate coefficients, from $f_j(q)$.

(4) Solve $\vec{F}(\vec{n}^{\rm new}) = 0$ for given rate coefficients to obtain the new solution vector $\vec{n}^{new}$.

(5) Compute the relative changes of electron density $n_{\rm e}$ and mean grain charges $\langle q_j \rangle$ in all size bins j between iterations.

(6) If these relative changes are $< 10^{-5}$ and $< 10^{-2}$, respectively, then take $\vec{n}^{new}$ as solution and stop the iteration.

(7) Provide a better guess for $\vec{n}$ and jump back to (2).

For step (7), we applied the following strategy. Each iteration was assigned a quality defined as $Q^{\rm new} = n_{\rm e}^{\rm new} - n_{\rm e}$. At first instance, we took $\vec{n} \leftarrow \vec{n}^{\rm new}$ as the improved guess in step (7), that is, we performed a Λ iteration. In all subsequent calls, we used the previous and current electron densities and Q values to provide a better guess of the solution vector,

$$0 = Q^{\rm new} + X\,(Q - Q^{\rm new}) \tag{A.2}$$

$$\vec{n} \leftarrow \vec{n}^{\rm new} + X\,(\vec{n} - \vec{n}^{\rm new}), \tag{A.3}$$

by determining the value for X that nullifies Q in case Q is a linear function of $n_{\rm e}$, that is, we performed a Newton step. Precisely speaking, we put $0 = Q^{\rm new} + \frac{\partial Q}{\partial n_{\rm e}}(n_{\rm e}^0 - n_{\rm e}^{\rm new})$ where we found $\frac{\partial Q}{\partial n_{\rm e}} = (Q - Q^{\rm new})/(n_{\rm e} - n_{\rm e}^{\rm new})$ from the two previous iterations to determine the next improved guess of the electron density $n_{\rm e}^0$ related to $X = (n_{\rm e}^0 - n_{\rm e}^{\rm new})/(n_{\rm e} - n_{\rm e}^{\rm new})$. If the magnitude of the new quality $Q^{\rm new}$ was much smaller than the magnitude of the old quality Q, X was close to zero, and we essentially performed another Λ iteration. The reader may

verify that the resulting electron density according Eq. (A.3) is indeed n_e^0. This numerical method typically converges within a couple of iterations. In a few cases, however, the method started to oscillate. We therefore monitored the Q values and saved the $\vec{n}$ vectors that were encountered during the iteration. Once we found the negative and positive entries for Q, we bracketed the solution and used the two iterations that produced the smallest positive and largest negative Q values to provide a better next guess for $\vec{n}$ in step (7).

In case we required a time-dependent solution of Eq. (A.1), not performed in this paper, we used a different strategy. The problem in this case is that with constant rate coefficients, the solution may start to alternate between two charging states with every time step taken. For example, highly negatively charged grains do not take any more electrons (i.e., the $k_{\mathrm{m},j,\mathrm{e}}$ become small), which means that during the next time step, the grains charge up less negatively, and so on. Our solution here was to monitor the dependencies of the effective rate coefficients k_r on electron density n_e and use the correction power law

$$k_r = k_r^\mathrm{ref} \left(\frac{n_\mathrm{e}}{n_\mathrm{e}^\mathrm{ref}} \right)^{p_r} \tag{A.4}$$

whenever the ODE solver required the RHS or the Jacobian. The term $n_\mathrm{e}^\mathrm{ref}$ is a reference electron density from which k_r^ref was calculated, and n_e is the actual electron density occurring during the integration. The term p_r is a rate coefficient correction power law index. The initial conditions were $\vec{n} = \vec{n}(t{=}0)$, $n_\mathrm{e}^\mathrm{ref} = n_\mathrm{e}(t{=}0)$, and $p_r = 0$.

The whole time-dependent approach can be summarized in eight steps:

(1) Compute $f_j(q)$ from $\vec{n}$ and rate coefficients k_r^ref from $f_j(q)$.

(2) Advance the chemistry for time step Δt from $\vec{n}$ with rate coefficients according to Eq. (A.4), resulting in $\vec{n}^\mathrm{new}(t + \Delta t)$.

(3) Compute new $f_j(q)$ and new rate coefficients k_r^new from $\vec{n}^\mathrm{new}$.

(4) Update the rate coefficient correction indices as $p_r = (\log k_r^\mathrm{new} - \log k_r)/(\log n_\mathrm{e}^\mathrm{new} - \log n_\mathrm{e})$.

(5) Assess the uncertainty $\Delta\vec{n}$ based on the difference between $\vec{k}$ and $\vec{k}^\mathrm{new}$ and Δt.

(6) Limit the increase of the next time step Δt when large relative uncertainties $\Delta n_i/n_i$ are found.

(7) If $t + \Delta t$ reaches the requested total integration time, take $\vec{n}^{\rm new}$ as the solution and stop the iteration.

(8) Update $t{=}t + \Delta t$, $\vec{n} = \vec{n}^{\rm new}$, $n_{\rm e}^{\rm ref}{=}n_{\rm e}^{\rm new}$, and $k_r^{\rm ref} = k_r^{\rm new}$ and jump back to (2).

This algorithm can slow down the computation of a t-dependent solution when strong oscillations would occur, resulting in large Δn_i where smaller time steps are indeed required. However, the algorithm manages to sufficiently damp these oscillations and quickly re-increases the time step once the conditions have changed and the oscillations disappear.

A.3 Dissociative molecular ion attachment reactions

Consider a reaction between dust grains and $NH_4{}^+$ molecules, in which the $NH_4{}^+$ molecule dissociates,

$$Z^{-q} + NH_4{}^+ \rightarrow Z^{-(q-1)} + NH_3 + H \tag{A.5}$$

where $Z^{-(q-1)}$ is a dust grain that is less negatively charged than Z^{-q} by a factor of one. The reaction enthalpy, which tells us whether a reaction is exothermic or endotherm, is given by

$$\Delta H_r = H_f(Z^{-(q-1)}) + H_f(NH_3) + H_f(H) - H_f(Z^{-q}) - H_f(NH_4{}^+) \ , \tag{A.6}$$

where H_f is the heat of formation of a substance from a chemical standard state, which we set here as purely atomic in the absence of electric fields. For neutral molecules, we used the atomization energies H_f^0 derived from the standard enthalpies at 0K from UMIST Woodall et al. [2007], but for $H_f(NH_4{}^+)$, we needed to take into account the electric potential in the presence of the electric

field of the dust grain at its surface

$$H_f(\mathrm{NH_3}) = H_f^0(\mathrm{NH_3}) \tag{A.7}$$
$$H_f(\mathrm{H}) = H_f^0(\mathrm{H}) \tag{A.8}$$
$$H_f(\mathrm{NH_4^+}) = H_f^0(\mathrm{NH_4^+}) - \frac{qe^2}{a} \ . \tag{A.9}$$

The heat of formation of a negatively charged dust grains is

$$H_f(Z^{-q}) = H_f(\mathrm{atoms} \to Z^0) + \sum_{i=1}^{q} H_f(Z^{-(i-1)} \to Z^{-i}) \ , \tag{A.10}$$

where $H_f(\mathrm{atoms} \to Z^0)$ is the heat of formation of a dust grain from the atoms it is composed of. The term $H_f(Z^{-(i-1)} \to Z^{-i})$ describes the energy liberated when moving a single electron from infinity to the grain's surface (takes energy) and then attaching it to the surface (liberates energy E_0)

$$H_f(Z^{-(i-1)} \to Z^{-i}) = -E_0 + \frac{(i-1)e^2}{a}. \tag{A.11}$$

Using the Gaussian sum formula, the total formation enthalpy of a negatively charged grain is hence

$$H_f(Z^{-q}) = H_f(\mathrm{atoms} \to Z^0) - q\,E_0 + \frac{e^2}{a}\frac{q}{2}(q-1) \ . \tag{A.12}$$

From Eq. (2.12), we could identify the constant $E_0 = W_0 - E_{\mathrm{bg}}$, where W_0 is the work function and E_{bg} the band gap, and we assumed both to be independent of q.

The reaction enthalpy according to Eq. (A.6) is then given by

$$\begin{aligned}\Delta H_r &= E_0 + \frac{e^2}{a} + H_f^0(\mathrm{NH_3}) + H_f^0(\mathrm{H}) - H_f^0(\mathrm{NH_4^+}) \\ &= E_0 + \frac{e^2}{a} + P_A(\mathrm{NH_4^+}) - 13.6\,\mathrm{eV}\end{aligned} \tag{A.13}$$

where the proton affinity is $P_A(\mathrm{NH_4^+}) = H_f^0(\mathrm{NH_3}) + H_f^0(\mathrm{H^+}) - H_f^0(\mathrm{NH_4^+})$, and $H_f^0(\mathrm{H}) - H_f^0(\mathrm{H^+}) = -13.6\,\mathrm{eV}$ is the ionization energy of hydrogen. Since the term e^2/a is negligible even for grains as small as $0.1\,\mu$m, Eq. (A.13) allowed us to state that a dissociative attachment reaction is exothermal when the work function minus the band gap plus the proton affinity of the respective molecule

is smaller than 13.6 eV, independent of q.

There is, however, a small correction term of order e^2/a that complicates things. In our derivation, this term arises from the removal of one electron and one positive molecular ion from the electric field at the grain surface by the reaction, and this term is size dependent. Similar correction terms appear in Eqs. (2.12) and (2.13). In the current code version, we used $E_0 = 5.89\,\mathrm{eV}$, as explained in more detail at the end of Section 2.1.4.

Bibliography

P. Woitke, M. Min, C. Pinte, W. F. Thi, I. Kamp, C. Rab, F. Anthonioz, S. Antonellini, C. Baldovin-Saavedra, A. Carmona, C. Dominik, O. Dionatos, J. Greaves, M. Güdel, J. D. Ilee, A. Liebhart, F. Ménard, L. Rigon, L. B.F.M. Waters, G. Aresu, R. Meijerink, and M. Spaans. Consistent dust and gas models for protoplanetary disks: I. Disk shape, dust settling, opacities, and PAHs. *Astronomy and Astrophysics*, 586, 2016. ISSN 14320746. doi: 10.1051/0004-6361/201526538.

U.G. Jørgensen, F Amadio, B Campos Estrada, K Holten Møller, A Schneider, T Balduin, A D'Alessandro, E Symeonidou, C Helling, Å Nordlund, and P Woitke. A grid of self-consistent msg (marcs-staticweather-ggchem) cool stellar, sub-stellar, and exoplanetary model atmospheres.

A. A. Goodman, P. J. Benson, G. A. Fuller, and P. C. Myers. Dense Cores in Dark Clouds. VIII. Velocity Gradients. ApJ, 406:528, April 1993. doi: 10.1086/172465.

C. J. Lada and B. A. Wilking. The nature of the embedded population in the rho Ophiuchi dark cloud : mid-infrared observations. ApJ, 287:610–621, December 1984. doi: 10.1086/162719.

Karin I. Öberg, Viviana V. Guzmán, Catherine Walsh, Yuri Aikawa, Edwin A. Bergin, Charles J. Law, Ryan A. Loomis, Felipe Alarcón, Sean M. Andrews, Jaehan Bae, Jennifer B. Bergner, Yann Boehler, Alice S. Booth, Arthur D. Bosman, Jenny K. Calahan, Gianni Cataldi, L. Ilsedore Cleeves, Ian Czekala, Kenji Furuya, Jane Huang, John D. Ilee, Nicolas T. Kurtovic, Romane Le Gal, Yao Liu, Feng Long, François Ménard, Hideko Nomura, Laura M. Pérez, Chunhua Qi, Kamber R. Schwarz, Anibal Sierra, Richard Teague, Takashi Tsukagoshi, Yoshihide Yamato, Merel L. R. van't Hoff, Abygail R. Waggoner,

David J. Wilner, and Ke Zhang. Molecules with ALMA at Planet-forming Scales (MAPS). I. Program Overview and Highlights. ApJS, 257(1):1, November 2021. doi: 10.3847/1538-4365/ac1432.

John D. Ilee, Catherine Walsh, Alice S. Booth, Yuri Aikawa, Sean M. Andrews, Jaehan Bae, Edwin A. Bergin, Jennifer B. Bergner, Arthur D. Bosman, Gianni Cataldi, L. Ilsedore Cleeves, Ian Czekala, Viviana V. Guzmán, Jane Huang, Charles J. Law, Romane Le Gal, Ryan A. Loomis, François Ménard, Hideko Nomura, Karin I. Öberg, Chunhua Qi, Kamber R. Schwarz, Richard Teague, Takashi Tsukagoshi, David J. Wilner, Yoshihide Yamato, and Ke Zhang. Molecules with ALMA at Planet-forming Scales (MAPS). IX. Distribution and Properties of the Large Organic Molecules HC_3N, CH_3CN, and c-C_3H_2. ApJS, 257(1):9, November 2021. doi: 10.3847/1538-4365/ac1441.

Joanna Drazkowska, Bertram Bitsch, Michiel Lambrechts, Gijs D. Mulders, Daniel Harsono, Allona Vazan, Beibei Liu, Chris W. Ormel, Katherine Kretke, and Alessandro Morbidelli. Planet Formation Theory in the Era of ALMA and Kepler: from Pebbles to Exoplanets. *arXiv e-prints*, art. arXiv:2203.09759, March 2022.

Arthur Daniel Bosman. *Uncovering the ingredients for planet formation.* PhD thesis, University of Leiden, Netherlands, January 2018.

Joseph C. Weingartner and B. T. Draine. Dust Grain-Size Distributions and Extinction in the Milky Way, Large Magellanic Cloud, and Small Magellanic Cloud. ApJ, 548(1):296–309, February 2001. doi: 10.1086/318651.

B. T. Draine. Interstellar Dust Grains. ARA&A, 41:241–289, January 2003. doi: 10.1146/annurev.astro.41.011802.094840.

M. Min, L. B. F. M. Waters, A. de Koter, J. W. Hovenier, L. P. Keller, and F. Markwick-Kemper. The shape and composition of interstellar silicate grains. *Astronomy and Astrophysics*, 462(2):667–676, November 2006. ISSN 1432-0746. doi: 10.1051/0004-6361:20065436. URL `http://dx.doi.org/10.1051/0004-6361:20065436`.

B. Dubrulle, G. Morfill, and M. Sterzik. The dust subdisk in the protoplanetary nebula. Icarus, 114(2):237–246, April 1995. doi: 10.1006/icar.1995.1058.

C. P. Dullemond and C. Dominik. The effect of dust settling on the appearance of protoplanetary disks. A&A, 421:1075–1086, July 2004. doi: 10.1051/0004-6361:20040284.

A. Riols and G. Lesur. Dust settling and rings in the outer regions of protoplanetary discs subject to ambipolar diffusion. A&A, 617:A117, September 2018. doi: 10.1051/0004-6361/201833212.

T. Birnstiel, M. Fang, and A. Johansen. Dust Evolution and the Formation of Planetesimals. Space Sci. Rev., 205(1-4):41–75, December 2016. doi: 10.1007/s11214-016-0256-1.

Tilman Birnstiel. Dust growth and evolution in protoplanetary disks. *arXiv e-prints*, art. arXiv:2312.13287, December 2023. doi: 10.48550/arXiv.2312.13287.

Andrew N. Youdin and Jeremy Goodman. Streaming Instabilities in Protoplanetary Disks. ApJ, 620(1):459–469, February 2005. doi: 10.1086/426895.

A. Youdin and A. Johansen. Protoplanetary disk turbulence driven by the streaming instability: Linear evolution and numerical methods. *The Astrophysical Journal*, 662(1):613–626, June 2007. ISSN 1538-4357. doi: 10.1086/516729. URL `http://dx.doi.org/10.1086/516729`.

A. Johansen and A. Youdin. Protoplanetary Disk Turbulence Driven by the Streaming Instability: Nonlinear Saturation and Particle Concentration. ApJ, 662(1):627–641, June 2007. doi: 10.1086/516730.

Anders Johansen and Michiel Lambrechts. Forming planets via pebble accretion. *Annual Review of Earth and Planetary Sciences*, 45(1):359–387, August 2017. ISSN 1545-4495. doi: 10.1146/annurev-earth-063016-020226. URL `http://dx.doi.org/10.1146/annurev-earth-063016-020226`.

M. Lambrechts and A. Johansen. Rapid growth of gas-giant cores by pebble accretion. *Astronomy and Astrophysics*, 544:A32, July 2012. ISSN 1432-0746. doi: 10.1051/0004-6361/201219127. URL `http://dx.doi.org/10.1051/0004-6361/201219127`.

Vitaly Akimkin, Alexei V. Ivlev, Paola Caselli, Munan Gong, and Kedron Silsbee. Coagulation–fragmentation equilibrium for charged dust: Abundance of submicron grains increases dramatically in protoplanetary disks. *The Astrophysical Journal*, 953(1):72, August 2023. ISSN 1538-4357. doi: 10.3847/1538-4357/ace2c5. URL `http://dx.doi.org/10.3847/1538-4357/ace2c5`.

Satoshi Okuzumi. Electric Charging of Dust Aggregates and its Effect on Dust Coagulation in Protoplanetary Disks. ApJ, 698(2):1122–1135, June 2009. doi: 10.1088/0004-637X/698/2/1122.

Satoshi Okuzumi, Hidekazu Tanaka, Taku Takeuchi, and Masa-aki Sakagami. Electrostatic Barrier Against Dust Growth in Protoplanetary Disks. I. Classifying the Evolution of Size Distribution. ApJ, 731(2):95, April 2011. doi: 10.1088/0004-637X/731/2/95.

V. V. Akimkin, A. V. Ivlev, and P. Caselli. Inhibited Coagulation of Micron-size Dust Due to the Electrostatic Barrier. ApJ, 889(1):64, January 2020. doi: 10.3847/1538-4357/ab6299.

Richard P. Nelson, Oliver Gressel, and Orkan M. Umurhan. Linear and non-linear evolution of the vertical shear instability in accretion discs. MNRAS, 435(3):2610–2632, November 2013. doi: 10.1093/mnras/stt1475.

Hubert Klahr and Alexander Hubbard. Convective Overstability in Radially Stratified Accretion Disks under Thermal Relaxation. ApJ, 788(1):21, June 2014. doi: 10.1088/0004-637X/788/1/21.

Philip S. Marcus, Suyang Pei, Chung-Hsiang Jiang, and Pedram Hassanzadeh. Three-Dimensional Vortices Generated by Self-Replication in Stably Stratified Rotating Shear Flows. Phys. Rev. Lett., 111(8):084501, August 2013. doi: 10.1103/PhysRevLett.111.084501.

Philip S. Marcus, Suyang Pei, Chung-Hsiang Jiang, Joseph A. Barranco, Pedram Hassanzadeh, and Daniel Lecoanet. Zombie Vortex Instability. I. A Purely Hydrodynamic Instability to Resurrect the Dead Zones of Protoplanetary Disks. ApJ, 808(1):87, July 2015. doi: 10.1088/0004-637X/808/1/87.

Philip S. Marcus, Suyang Pei, Chung-Hsiang Jiang, and Joseph A. Barranco. Zombie Vortex Instability. II. Thresholds to Trigger Instability and the Properties of Zombie Turbulence in the Dead Zones of Protoplanetary Disks. ApJ, 833(2):148, December 2016. doi: 10.3847/1538-4357/833/2/148.

Geoffroy R. J. Lesur and Henrik Latter. On the survival of zombie vortices in protoplanetary discs. MNRAS, 462(4):4549–4554, November 2016. doi: 10.1093/mnras/stw2172.

Raquel Salmeron and Mark Wardle. Magnetorotational instability in protoplanetary discs: the effect of dust grains. MNRAS, 388(3):1223–1238, August 2008. doi: 10.1111/j.1365-2966.2008.13430.x.

Takeru K. Suzuki, Takayuki Muto, and Shu-ichiro Inutsuka. Protoplanetary disk winds via magnetorotational instability: Formation of an inner hole and a crucial assist for planet formation. *The Astrophysical Journal*, 718(2): 1289–1304, July 2010. ISSN 1538-4357. doi: 10.1088/0004-637x/718/2/1289. URL `http://dx.doi.org/10.1088/0004-637X/718/2/1289`.

Daniel Perez-Becker and Eugene Chiang. Surface Layer Accretion in Conventional and Transitional Disks Driven by Far-ultraviolet Ionization. ApJ, 735 (1):8, July 2011. doi: 10.1088/0004-637X/735/1/8.

Xue-Ning Bai. Magnetorotational-instability-driven Accretion in Protoplanetary Disks. ApJ, 739(1):50, September 2011. doi: 10.1088/0004-637X/739/1/50.

W. F. Thi, G. Lesur, P. Woitke, I. Kamp, Ch Rab, and A. Carmona. Radiation thermo-chemical models of protoplanetary disks: Grain and polycyclic aromatic hydrocarbon charging. *Astronomy and Astrophysics*, 632(Jin 1996), 2019. ISSN 14320746. doi: 10.1051/0004-6361/201732187.

C. P. Dullemond and A. B. T. Penzlin. Dust-driven viscous ring-instability in protoplanetary disks. A&A, 609:A50, January 2018. doi: 10.1051/0004-6361/201731878.

Zsolt Regály, Kundan Kadam, and Cornelis P. Dullemond. Self-sustaining vortices in protoplanetary discs: Setting the stage for planetary system formation. MNRAS, 506(2):2685–2694, September 2021. doi: 10.1093/mnras/stab1846.

Zs. Regaly, K. Kadam, and D. Tarczay-Nehez. Planetary nurseries: vortices formed at smooth viscosity transition. *arXiv e-prints*, art. arXiv:2302.03430, February 2023. doi: 10.48550/arXiv.2302.03430.

Shu-ichiro Inutsuka and Takayoshi Sano. Self-sustained ionization and vanishing dead zones in protoplanetary disks. *The Astrophysical Journal*, 628(2):L155, 2005.

Xue-Ning Bai and James M. Stone. Effect of Ambipolar Diffusion on the Nonlinear Evolution of Magnetorotational Instability in Weakly Ionized Disks. ApJ, 736(2):144, August 2011. doi: 10.1088/0004-637X/736/2/144.

A. V. Ivlev, V. V. Akimkin, and P. Caselli. Ionization and Dust Charging in Protoplanetary Disks. ApJ, 833(1):92, December 2016. doi: 10.3847/1538-4357/833/1/92.

Philip J. Armitage and Wilhelm Kley. *From Protoplanetary Disks to Planet Formation: Saas-Fee Advanced Course 45. Swiss Society for Astrophysics and Astronomy.* Springer Berlin Heidelberg, 2019. ISBN 9783662586877. doi: 10.1007/978-3-662-58687-7. URL `http://dx.doi.org/10.1007/978-3-662-58687-7`.

Richard E. Orville. A High-Speed Time-Resolved Spectroscopic Study of the Lightning Return Stroke: Part I. A Qualitative Analysis. *Journal of Atmospheric Sciences*, 25(5):827–838, September 1968a. doi: 10.1175/1520-0469(1968)025\textless{}0827:AHSTRS\textgreater{}2.0.CO;2.

Richard E. Orville. A High-Speed Time-Resolved Spectroscopic Study of the Lightning Return Stroke: Part II. A Quantitative Analysis. *Journal of Atmospheric Sciences*, 25(5):839–851, September 1968b. doi: 10.1175/1520-0469(1968)025\textless{}0839:AHSTRS\textgreater{}2.0.CO;2.

Richard E. Orville. A High-Speed Time-Resolved Spectroscopic Study of the Lightning Return Stroke. Part III. A Time-Dependent Model. *Journal of Atmospheric Sciences*, 25(5):852–856, September 1968c. doi: 10.1175/1520-0469(1968)025\textless{}0852:AHSTRS\textgreater{}2.0.CO;2.

J. F. Noxon. Atmospheric nitrogen fixation by lightning. Geophys. Res. Lett., 3(8):463–465, August 1976. doi: 10.1029/GL003i008p00463.

R. D. Hill, R. G. Rinker, and H. D. Wilson. Atmospheric nitrogen fixation by lightning. *Journal of Atmospheric Sciences*, 37:179–192, January 1980. doi: 10.1175/1520-0469(1980)037\textless{}0179:ANFBL\textgreater{}2.0.CO;2.

Colin Price, Joyce Penner, and Michael Prather. NO_x from lightning: 1. Global distribution based on lightning physics. J. Geophys. Res., 102(D5):5929–5941, March 1997. doi: 10.1029/96JD03504.

Rafael Navarro-González, Christopher P. McKay, and Delphine Nna Mvondo. A possible nitrogen crisis for Archaean life due to reduced nitrogen fixation by lightning. Nature, 412(6842):61–64, July 2001.

O. Wild. Modelling the global tropospheric ozone budget: exploring the variability in current models. *Atmospheric Chemistry & Physics*, 7(10):2643–2660, May 2007. doi: 10.5194/acp-7-2643-2007.

Lee T. Murray, Jennifer A. Logan, and Daniel J. Jacob. Interannual variability in tropical tropospheric ozone and OH: The role of lightning. *Journal of Geophysical Research (Atmospheres)*, 118(19):11,468–11,480, October 2013. doi: 10.1002/jgrd.50857.

S. Chapman. *A Theory of Upper-atmospheric Ozone*. Memoirs of the Royal Meteorological Society. Edward Stanford, 1930. URL `https://books.google.at/books?id=DdOVGwAACAAJ`.

C.T. Russell, R.J. Strangeway, and T.L. Zhang. Lightning detection on the venus express mission. *Planetary and Space Science*, 54(13):1344–1351, 2006. ISSN 0032-0633. doi: https://doi.org/10.1016/j.pss.2006.04.026. URL `https://www.sciencedirect.com/science/article/pii/S0032063306001619`. The Planet Venus and the Venus Express Mission.

C. T. Russell, T. L. Zhang, M. Delva, W. Magnes, R. J. Strangeway, and H. Y. Wei. Lightning on venus inferred from whistler-mode waves in the ionosphere. *Nature*, 450(7170):661–662, November 2007. doi: 10.1038/nature05930. URL `https://doi.org/10.1038/nature05930`.

C. T. Russell, T. L. Zhang, and H. Y. Wei. Whistler mode waves from lightning on venus: Magnetic control of ionospheric access. *Journal of Geophysical Research: Planets*, 113(E5), 2008. doi: https://doi.org/10.1029/2008JE003137. URL `https://agupubs.onlinelibrary.wiley.com/doi/abs/10.1029/2008JE003137`.

Kevin H. Baines, Mona L. Delitsky, Thomas W. Momary, Robert H. Brown, Bonnie J. Buratti, Roger N. Clark, and Philip D. Nicholson. Storm clouds on Saturn: Lightning-induced chemistry and associated materials consistent with Cassini/VIMS spectra. Planet. Space Sci., 57(14-15):1650–1658, December 2009. doi: 10.1016/j.pss.2009.06.025.

U. A. Dyudina, A. P. Ingersoll, S. P. Ewald, C. C. Porco, G. Fischer, W. S. Kurth, and R. A. West. Detection of visible lightning on Saturn. Geophys. Res. Lett., 37(9):L09205, May 2010. doi: 10.1029/2010GL043188.

Marrick Braam, Paul I. Palmer, Leen Decin, Robert J. Ridgway, Maria Zamyatina, Nathan J. Mayne, Denis E. Sergeev, and N. Luke Abraham. Lightning-induced chemistry on tidally-locked Earth-like exoplanets. MNRAS, 517(2): 2383–2402, December 2022. doi: 10.1093/mnras/stac2722.

Marrick Braam, Paul I. Palmer, Leen Decin, Maureen Cohen, and Nathan J. Mayne. Stratospheric dayside-to-nightside circulation drives the 3D ozone distribution on synchronously rotating rocky exoplanets. MNRAS, 526(1): 263–278, November 2023. doi: 10.1093/mnras/stad2704.

Tsutomu Takahashi. Riming Electrification as a Charge Generation Mechanism in Thunderstorms. *Journal of Atmospheric Sciences*, 35(8):1536–1548, August 1978. doi: 10.1175/1520-0469(1978)035\textless{}1536:REAACG\textgreater{}2.0.CO;2.

E. R. Jayaratne, C. P. R. Saunders, and J. Hallett. Laboratory studies of the charging of soft-hail during ice crystal interactions. *Quarterly Journal of the Royal Meteorological Society*, 109(461):609–630, July 1983. doi: 10.1002/qj.49710946111.

C. P. R. Saunders. A Review of Thunderstorm Electrification Processes. *Journal of Applied Meteorology*, 32(4):642–655, April 1993. doi: 10.1175/1520-0450(1993)032\textless{}0642:AROTEP\textgreater{}2.0.CO;2.

C. P. R. Saunders and S. L. Peck. Laboratory studies of the influence of the rime accretion rate on charge transfer during crystal/graupel collisions. J. Geophys. Res., 103(D12):13,949–13,956, June 1998. doi: 10.1029/97JD02644.

Isobel M. P. Houghton, Karen L. Aplin, and Keri A. Nicoll. Triboelectric Charging of Volcanic Ash from the 2011 Grímsvötn Eruption. Phys. Rev. Lett., 111 (11):118501, September 2013. doi: 10.1103/PhysRevLett.111.118501.

B. Baker, M. B. Baker, E. R. Jayaratne, J. Latham, and C. P. R. Saunders. The influence of diffusional growth rates on the charge transfer accompanying rebounding collisions between ice crystals and soft hailstones. *Quarterly Journal of the Royal Meteorological Society*, 113(478):1193–1215, October 1987. doi: 10.1002/qj.49711347807.

J. G. Dash, B. L. Mason, and J. S. Wettlaufer. Theory of charge and mass transfer in ice-ice collisions. J. Geophys. Res., 106(D17):20,395–20,402, January 2001. doi: 10.1029/2001JD900109.

Daniel J. Lacks and Artem Levandovsky. Effect of particle size distribution on the polarity of triboelectric charging in granular insulator systems. *Journal of Electrostatics*, 65(2):107–112, 2007. ISSN 0304-3886. doi: https://doi.org/10.1016/j.elstat.2006.07.010. URL `https://www.sciencedirect.com/science/article/pii/S0304388606000866`.

Keith M. Forward, Daniel J. Lacks, and R. Mohan Sankaran. Charge Segregation Depends on Particle Size in Triboelectrically Charged Granular Materials. Phys. Rev. Lett., 102(2):028001, January 2009. doi: 10.1103/PhysRevLett.102.028001.

Maribeth Stolzenburg, W. David Rust, Bradley F. Smull, and Thomas C. Marshall. Electrical structure in thunderstorm convective regions: 1. Mesoscale convective systems. J. Geophys. Res., 103(D12):14,059–14,078, June 1998. doi: 10.1029/97JD03546.

Eric C. Bruning, W. David Rust, Terry J. Schuur, Donald R. Macgorman, Paul R. Krehbiel, and William Rison. Electrical and Polarimetric Radar Observations of a Multicell Storm in TELEX. *Monthly Weather Review*, 135 (7):2525, January 2007. doi: 10.1175/MWR3421.1.

M. Brook, C. B. Moore, and T. Sigurgeirsson. Lightning in volcanic clouds. J. Geophys. Res., 79(3):472–475, January 1974. doi: 10.1029/JC079i003p00472.

Damien Gaudin, Corrado Cimarelli, Veronica Becker, and Marco Knüver. What controls the occurrence of lightning in volcanic ash plumes? A quantitative lab analysis. In *EGU General Assembly Conference Abstracts*, EGU General Assembly Conference Abstracts, page 12793, April 2018.

Yoav Yair. New results on planetary lightning. *Advances in Space Research*, 50 (3):293–310, August 2012. ISSN 0273-1177. doi: 10.1016/j.asr.2012.04.013. URL `http://dx.doi.org/10.1016/j.asr.2012.04.013`.

John S. Townsend. Lxvi. the conductivity produced in gases by the aid of ultraviolet light. *The London, Edinburgh, and Dublin Philosophical Magazine and*

Journal of Science, 3(18):557–576, 1902. doi: 10.1080/14786440209462804. URL https://doi.org/10.1080/14786440209462804.

S. Matsusaka, H. Maruyama, T. Matsuyama, and M. Ghadiri. Triboelectric charging of powders: A review. *Chemical Engineering Science*, 65(22): 5781–5807, November 2010. ISSN 0009-2509. doi: 10.1016/j.ces.2010.07.005. URL http://dx.doi.org/10.1016/j.ces.2010.07.005.

Daniel J. Lacks and Troy Shinbrot. Long-standing and unresolved issues in triboelectric charging. *Nature Reviews Chemistry*, 3(8):465–476, July 2019. ISSN 2397-3358. doi: 10.1038/s41570-019-0115-1. URL http://dx.doi.org/10.1038/s41570-019-0115-1.

Minsu Seol, Seongsu Kim, Yeonchoo Cho, Kyung-Eun Byun, Haeryong Kim, Jihye Kim, Sung Kyun Kim, Sang-Woo Kim, Hyeon-Jin Shin, and Seongjun Park. Triboelectric series of 2d layered materials. *Advanced Materials*, 30 (39), August 2018. ISSN 1521-4095. doi: 10.1002/adma.201801210. URL http://dx.doi.org/10.1002/adma.201801210.

Haiyang Zou, Litong Guo, Hao Xue, Ying Zhang, Xiaofang Shen, Xiaoting Liu, Peihong Wang, Xu He, Guozhang Dai, Peng Jiang, Haiwu Zheng, Binbin Zhang, Cheng Xu, and Zhong Lin Wang. Quantifying and understanding the triboelectric series of inorganic non-metallic materials. *Nature Communications*, 11(1), April 2020. ISSN 2041-1723. doi: 10.1038/s41467-020-15926-1. URL http://dx.doi.org/10.1038/s41467-020-15926-1.

Felix Jungmann, Hannah van Unen, Jens Teiser, and Gerhard Wurm. Violation of triboelectric charge conservation on colliding particles. Phys. Rev. E, 104 (2):L022601, August 2021. doi: 10.1103/PhysRevE.104.L022601.

Felix Jungmann and Gerhard Wurm. Observation of bottom-up formation for charged grain aggregates related to pre-planetary evolution beyond the bouncing barrier. A&A, 650:A77, June 2021. doi: 10.1051/0004-6361/202039430.

Gerhard Wurm, Felix Jungmann, and Jens Teiser. Ionizing protoplanetary discs in pebble collisions. MNRAS, 517(1):L65–L70, November 2022. doi: 10.1093/mnrasl/slac077.

P. Ábrahám, A. Juhász, C. P. Dullemond, Á. Kóspál, R. van Boekel, J. Bouwman, Th. Henning, A. Moór, L. Mosoni, A. Sicilia-Aguilar, and N. Sipos.

Episodic formation of cometary material in the outburst of a young Sun-like star. Nature, 459(7244):224–226, May 2009. doi: 10.1038/nature08004.

S. J. Desch and J. N. Cuzzi. The Generation of Lightning in the Solar Nebula. Icarus, 143(1):87–105, January 2000. doi: 10.1006/icar.1999.6245.

Takayuki Muranushi. Dust-dust collisional charging and lightning in protoplanetary discs. MNRAS, 401(4):2641–2664, February 2010. doi: 10.1111/j.1365-2966.2009.15848.x.

Satoshi Okuzumi and Shu-ichiro Inutsuka. The Nonlinear Ohm's Law: Plasma Heating by Strong Electric Fields and its Effects on the Ionization Balance in Protoplanetary Disks. ApJ, 800(1):47, February 2015. doi: 10.1088/0004-637X/800/1/47.

Satoshi Okuzumi, Shoji Mori, and Shu-ichiro Inutsuka. The Generalized Nonlinear Ohm's Law: How a Strong Electric Field Influences Nonideal MHD Effects in Dusty Protoplanetary Disks. ApJ, 878(2):133, June 2019. doi: 10.3847/1538-4357/ab2046.

A. Johansen and S. Okuzumi. Harvesting the Decay Energy of 26-Al to Drive Lightning Discharge and Chondrule Formation. In LPI Editorial Board, editor, *Chondrules and the Protoplanetary Disk*, volume 1963 of *LPI Contributions*, page 2012, February 2017.

T. Balduin, P. Woitke, U. G. Jørgensen, W. F. Thi, and Y. Narita. Size-dependent charging of dust particles in protoplanetary disks. Can turbulence cause charge separation and lightning? A&A, 678:A192, October 2023. doi: 10.1051/0004-6361/202346442.

P. Woitke, I. Kamp, and W. -F. Thi. Radiation thermo-chemical models of protoplanetary disks: I. Hydrostatic disk structure and inner rim. *Astronomy and Astrophysics*, 501(1):383–406, 2009. ISSN 00046361. doi: 10.1051/0004-6361/200911821.

I. Kamp, W. F. Thi, P. Woitke, C. Rab, S. Bouma, and F. Ménard. Consistent dust and gas models for protoplanetary disks. II. Chemical networks and rates. A&A, 607:A41, November 2017. doi: 10.1051/0004-6361/201730388.

J. Woodall, M. Agúndez, A. J. Markwick-Kemper, and T. J. Millar. The UMIST database for astrochemistry 2006. A&A, 466(3):1197–1204, May 2007. doi: 10.1051/0004-6361:20064981.

D. McElroy, C. Walsh, A. J. Markwick, M. A. Cordiner, K. Smith, and T. J. Millar. The UMIST database for astrochemistry 2012. A&A, 550:A36, February 2013. doi: 10.1051/0004-6361/201220465.

W. F. Thi, G. Lesur, P. Woitke, I. Kamp, Ch. Rab, and A. Carmona. Radiation thermo-chemical models of protoplanetary disks. Grain and polycyclic aromatic hydrocarbon charging. A&A, 632:A44, December 2019. doi: 10.1051/0004-6361/201732187.

Giambattista Aresu. *High energy irradiated protoplanetary disks : the X-rays and FUV role in thermo-chemical modeling*. PhD thesis, University of Groningen, Netherlands, December 2012.

Joseph C. Weingartner and B. T. Draine. Photoelectric Emission from Interstellar Dust: Grain Charging and Gas Heating. *The Astrophysical Journal Supplement Series*, 134(2):263–281, 2001. ISSN 0067-0049. doi: 10.1086/320852.

Jeffrey N. Cuzzi, Robert C. Hogan, Julie M. Paque, and Anthony R. Dobrovolskis. Size-selective Concentration of Chondrules and Other Small Particles in Protoplanetary Nebula Turbulence. ApJ, 546(1):496–508, January 2001. doi: 10.1086/318233.

B. Feuerbacher and B. Fitton. Experimental Investigation of Photoemission from Satellite Surface Materials. *Journal of Applied Physics*, 43(4):1563–1572, April 1972. doi: 10.1063/1.1661362.

Kin Wong, Sascha Vongehr, and Vitaly V. Kresin. Work functions, ionization potentials, and in between: Scaling relations based on the image-charge model. Phys. Rev. B, 67(3):035406, January 2003. doi: 10.1103/PhysRevB.67.035406.

T. Umebayashi and T. Nakano. Recombination of Ions and Electrons on Grains and the Ionization Degree in Dense Interstellar Clouds. PASJ, 32:405, January 1980.

Ch. Helling, M. Jardine, and F. Mokler. Ionization in Atmospheres of Brown Dwarfs and Extrasolar Planets. II. Dust-induced Collisional Ionization. ApJ, 737(1):38, August 2011. doi: 10.1088/0004-637X/737/1/38.

S. I. Kopnin, I. N. Kosarev, S. I. Popel, and M. Y. Yu. Localized structures of nanosize charged dust grains in Earth's middle atmosphere.

Planet. Space Sci., 52(13):1187–1194, November 2004. doi: 10.1016/j.pss.2004.09.003.

M. Rosenberg. Some physical processes in dusty plasmas. 277(1):125–133, Jun 2001. doi: 10.1023/A:1012240331407. URL `https://doi.org/10.1023/A:1012240331407`.

M. D'Angelo, S. Cazaux, I. Kamp, W. F. Thi, and P. Woitke. Water delivery in the inner solar nebula. Monte Carlo simulations of forsterite hydration. A&A, 622:A208, February 2019. doi: 10.1051/0004-6361/201833715.

W. F. Thi, S. Hocuk, I. Kamp, P. Woitke, Ch. Rab, S. Cazaux, P. Caselli, and M. D'Angelo. Warm dust surface chemistry in protoplanetary disks. Formation of phyllosilicates. A&A, 635:A16, March 2020. doi: 10.1051/0004-6361/201731747.

T. J. Millar, P. R. A. Farquhar, and K. Willacy. The UMIST Database for Astrochemistry 1995. A&AS, 121:139–185, January 1997. doi: 10.1051/aas:1997118.

C. M. Leung, E. Herbst, and W. F. Huebner. Synthesis of complex molecules in dense interstellar clouds via gas-phase chemistry: a pseudo time-dependent calculation. ApJS, 56:231–256, October 1984. doi: 10.1086/190982.

P.J. Linstrom and W.G. Mallard. *NIST Chemistry Webbook: NIST Standard Reference Database Number 69*. NIST, 2022. doi: https://doi.org/10.18434/T4D303. Google-Books-ID: dxM3ngAACAAJ.

C. R. Stark, Ch Helling, and D. A. Diver. Inhomogeneous cloud coverage through the Coulomb explosion of dust in substellar atmospheres. *Astronomy and Astrophysics*, 579:1–13, 2015. ISSN 14320746. doi: 10.1051/0004-6361/201526045.

Ryo Tazaki, Kohei Ichikawa, and Mitsuru Kokubo. Dust Destruction by Charging: A Possible Origin of Gray Extinction Curves of Active Galactic Nuclei. *The Astrophysical Journal*, 892(2):84, 2020. ISSN 1538-4357. doi: 10.3847/1538-4357/ab7822.

M. Padovani, D. Galli, and A. E. Glassgold. Cosmic-ray ionization of molecular clouds. A&A, 501(2):619–631, July 2009. doi: 10.1051/0004-6361/200911794.

Ch. Rab, M. Güdel, M. Padovani, I. Kamp, W. F. Thi, P. Woitke, and G. Aresu. Stellar energetic particle ionization in protoplanetary disks around T Tauri stars. A&A, 603:A96, July 2017. doi: 10.1051/0004-6361/201630241.

Ch. Rab, M. Güdel, P. Woitke, I. Kamp, W. F. Thi, M. Min, G. Aresu, and R. Meijerink. X-ray radiative transfer in protoplanetary disks. The role of dust and X-ray background fields. A&A, 609:A91, January 2018. doi: 10.1051/0004-6361/201731443.

L. Ilsedore Cleeves, Fred C. Adams, and Edwin A. Bergin. Exclusion of Cosmic Rays in Protoplanetary Disks: Stellar and Magnetic Effects. ApJ, 772(1):5, July 2013. doi: 10.1088/0004-637X/772/1/5.

Lewis F. Richardson. Atmospheric Diffusion Shown on a Distance-Neighbour Graph. *Proceedings of the Royal Society of London Series A*, 110(756):709–737, April 1926. doi: 10.1098/rspa.1926.0043.

A. Kolmogorov. The Local Structure of Turbulence in Incompressible Viscous Fluid for Very Large Reynolds' Numbers. *Akademiia Nauk SSSR Doklady*, 30:301–305, January 1941.

P. Woitke and Ch. Helling. Dust in brown dwarfs. II. The coupled problem of dust formation and sedimentation. A&A, 399:297–313, February 2003. doi: 10.1051/0004-6361:20021734.

Azra Abedi, Laleh Sattar, Mahtab Gharibi, and Larry A. Viehland. Investigation of temperature, electric field and drift-gas composition effects on the mobility of NH4+ ions in He, Ar, N2, and CO2. *International Journal of Mass Spectrometry*, 370:101–106, September 2014. doi: 10.1016/j.ijms.2014.06.014.

H. Ryzko. Drift velocity of electrons and ions in dry and humid air and in water vapour. *Proceedings of the Physical Society*, 85(6):1283–1295, June 1965. doi: 10.1088/0370-1328/85/6/327.

C. W. Ormel and J. N. Cuzzi. Closed-form expressions for particle relative velocities induced by turbulence. A&A, 466(2):413–420, May 2007. doi: 10.1051/0004-6361:20066899.

C. W. Ormel, M. Spaans, and A. G. G. M. Tielens. Dust coagulation in protoplanetary disks: porosity matters. A&A, 461(1):215–232, January 2007. doi: 10.1051/0004-6361:20065949.

T. Muranushi and T. Tomiyasu. Proto-planetary Nebulae Struck by Lightning? A Charge Separation Study of Ice Dust Grains And its Effect on Dust Growth. In Tomonori Usuda, Motohide Tamura, and Miki Ishii, editors, *Exoplanets and Disks: Their Formation and Diversity*, volume 1158 of *American Institute of Physics Conference Series*, pages 145–146, August 2009. doi: 10.1063/1.3215824.

Leonard B. Loeb. The Mobility of NA^+ Ions in N_2 and H_2 as a Function of Time. *Physical Review*, 38(3):549–571, August 1931. doi: 10.1103/PhysRev.38.549.

Nanna Bach-Møller, Christiane Helling, Uffe G. Jørgensen, and Martin B. Enghoff. Aggregation and Charging of Mineral Cloud Particles under High-energy Irradiation. ApJ, 962(1):87, February 2024. doi: 10.3847/1538-4357/ad13ef.

B. Gustafsson, R. A. Bell, K. Eriksson, and A. Nordlund. A grid of model atmospheres for metal-deficient giant stars. I. A&A, 42:407–432, September 1975.

B. Gustafsson, B. Edvardsson, K. Eriksson, U. G. Jørgensen, Å. Nordlund, and B. Plez. A grid of MARCS model atmospheres for late-type stars. I. Methods and general properties. A&A, 486(3):951–970, August 2008. doi: 10.1051/0004-6361:200809724.

Ch. Helling and P. Woitke. Dust in brown dwarfs. V. Growth and evaporation of dirty dust grains. A&A, 455(1):325–338, August 2006. doi: 10.1051/0004-6361:20054598.

P. Woitke, Ch. Helling, G. H. Hunter, J. D. Millard, G. E. Turner, M. Worters, J. Blecic, and J. W. Stock. Equilibrium chemistry down to 100 K. Impact of silicates and phyllosilicates on the carbon to oxygen ratio. A&A, 614:A1, June 2018. doi: 10.1051/0004-6361/201732193.

T. Grassi, S. Bovino, D. R. G. Schleicher, J. Prieto, D. Seifried, E. Simoncini, and F. A. Gianturco. KROME - a package to embed chemistry in astrophysical simulations. MNRAS, 439(3):2386–2419, April 2014. doi: 10.1093/mnras/stu114.

List of Figures

List of Tables